DISSERTATION

DEVELOPMENT OF A HIGH POWER HIGH ENERGY ULTRAFAST LASER

Submitted by

Han Chi

Department of Electrical and Computer Engineering

In partial fulfillment of the requirements

For the Degree of Doctor of Philosophy

Colorado State University

Fort Collins, Colorado

Fall 2021

Doctoral Committee:

Advisor: Jorge Rocca

Carmen Menoni
Mario Marconi
Siu Au Lee

ABSTRACT

DEVELOPMENT OF A HIGH POWER HIGH ENERGY ULTRAFAST LASER

This dissertation describes the development of high energy, high repetition rate laser technology based on cryogenically cooled diode-pumped Yb:YAG laser amplifiers. The key challenges of thermal management, the generation of high energy green pulses at high repetition rate, and the design of an ultrafast laser amplifier that uses the green pulses as pump are discussed in this dissertation.

To aid the development of thermal management solutions, an accurate, in situ, noninvasive optical technique to generate three-dimensional (3-D) temperature maps of cryogenic amplifiers during operation at high average power was demonstrated. The temperature is determined by analyzing the fluorescence spectra of the laser material (Yb:YAG) with a neural network algorithm. The accuracy of the technique relies on a calibration that does not depend on simulations. Results are presented for a cryogenic Yb:YAG active mirror laser amplifier operating at different pump conditions, which include kW pump power level operation. Based on this temperature measurement technique, an analysis of the thermal behavior of a high-energy kilowatt-average-power diode-pumped cryogenically cooled Yb:YAG active mirror laser amplifier is presented. Maps of the temperature distribution in the laser amplifier crystal at pump powers up to 1 kW were obtained for the first time by spectrally resolving the fluorescence induced by a scanning probe beam. The cryo-temperature measurement technique is applicable to other solid-state lasers materials. The wavefront distortions resulting from the front surface deformation and the overall deformation of the gain medium assembly were measured using a Mach–Zehnder interferometer. The measured deformations agree well with the results of finite element thermomechanical modeling simulations, and with the results of focal length shift measurements. The relative contributions to the optical path difference (OPD) of the mechanical deformations, refractive index changes, and electronic

contribution are discussed. The pump-induced mechanical deformations of the assembly dominate the OPD changes in the kilowatt-average-pump-power cryogenically cooled Yb:YAG active mirror laser investigated.

The generation of green (λ = 515 nm) Joule-level pulses at 1 kHz repetition rate was demonstrated. This was achieved by frequency doubling 1.2 J, 2 ns temporally shaped square pulses from a cryogenically cooled Yb:YAG laser in an LBO crystal. The generation of 0.94 J second-harmonic pulses at 1 kHz was demonstrated with 78% conversion efficiency. The unconverted light was sent through a second LBO crystal to generate an additional >100 mJ second-harmonic pulses to reach a total green average power of 1.04 kW. A higher conversion efficiency of 89% was also achieved for 0.58 J green pulses at 1 kHz. An application of this green laser is the pumping of high average power ultrafast laser amplifiers. The design of a two-stage water-cooled Ti:Sapphire amplifier system to generate 300 mJ pulses pre-compression using this green laser as pump is discussed. The simulation of the gain and thermal distribution of the 1st and 2nd stage amplifier are presented. The first experimental results of the operation of the first amplification stage of this laser system are discussed.

ACKNOWLEDGEMENTS

To begin, I would like to thank my advisor, Prof. Jorge Rocca, for his mentorship through the Ph.D. program. He has been a role model for me with his diligence in work. As a researcher, he also taught me to view things from different perspectives and to develop a broader vision of the work.

I would like to express my thanks to my committee members, Prof. Carmen Menoni, Prof. Siu Au Lee and Prof. Mario Marconi, for their insightful feedback and help in different ways.

Special thanks to Yong Wang, who played an important role not only in the research but also off the work during the last six years. It would not have been possible for me to finish the dissertation without his help.

I would like to appreciate all my colleagues working or having worked on this work, Vladimir Chvykov, Brendan Reagan, Cory Baumgarten, Hanchen Wang, Herman Bravo, Kristian Dehne, Gabe Murray, Alexander Meadows, and Aaron Davenport. The work is based on the efforts and contributions from all related people.

I would like to thank everyone who helped me in the past six years, including but not limited to: Ela Jankowska, Liang Yin, Shoujun Wang, Huanyu Song, Reed Hollinger, Alex Rockwood, Adam Higginson, Sergio Oloriz, Byron Fritch, Jethro Leroux, Sean Jonex, and others.

Most importantly, I would like to thank the support from all my family, espacially my wife, Dr. Le Yang. The support from her is my momentum to pursue the degree and to conquer barriers. The discussions with her initiate numerous creative ideas for the achievements in my work. I appreciate the life with you since we met in the summer of 2010.

DEDICATION

I would like to dedicate this thesis to my grandmother, Chen, Liqiao.

TABLE OF CONTENTS

Chapter 1

Introduction

1.1 A Brief History of Laser Development

Since the first laser by Theodore Maiman crossed the threshold for laser oscillation in 1960 [1], the development of lasers has revolutionized research and numerous applications in various fields. In the over 60-year evolution of the laser, the chase for better performance to meet the requirements for different applications has driven the development of gain medium materials, pump technologies, and optical designs. From the initial use of a ruby rod as the gain medium in the first demonstrated laser, different gain medium laser materials have enabled lasers with different characteristics and enhanced the laser performance, such as for high power operation, high pulse energy, and different pulse duration operation.

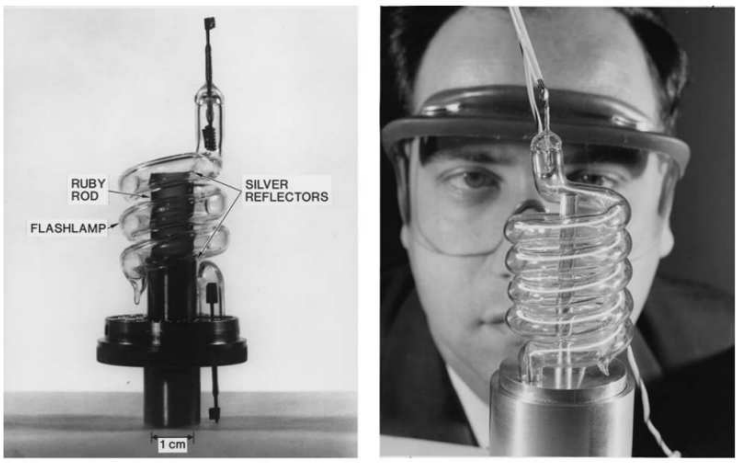

Figure 1.1: (a)Theodore Maiman's first laser, removed from aluminum cylinder used during operation, and (b) photo of Maiman behind a larger ruby laser, handed out at the Hughes press conference announcing the laser. The photographer insisted on posing Maiman with the larger laser, and initially many thought this was the first laser [2].

In the first decade after Maiman's demonstration, all types of matter: solids, gases and plasmas, and liquids (dye lasers) have been used as gain material for laser demonstration. The first gas laser, the helium-neon (He-Ne) laser, was invented by Ali Javan and William R. Bennett, Jr. in 1960 based on a selectively excited transition in the Ne atom [3]. The first semiconductor diode laser was demonstrated by Robert Hall in 1962 using GaAs [4]. The first ion laser was demonstrated by Earl Bell in 1963 in mercury vapor [5]. The CO_2 molecular laser was invented in 1964 and reached 200 W continuous wave (CW) in 1965 when nitrogen was added to provide efficient resonance excitation of the laser upper levels [6], and the first dye laser was realized in 1966 by Peter Sorokin [7]. After 60 years of laser development, new types of laser with increased power, various wavelengths, and pulse characteristics, are still being developed for various applications and purposes. Among all, solid-state lasers are the most widely used type for achieving high average power, high pulse energy, and high peak power.

1.2 Ultrafast Laser Development

The ultrafast laser, one of the most important branches of the laser family, is typically defined as a laser that generates laser pulses with less than picosecond (1 ps = 10^{-12} s) level pulse duration. The nature of ultrafast laser offers a powerful tool for different applications in various area involving fast processes and/or high peak power. However, it took several years after the birth of the laser to generate the laser pulses at the ultrafast level. At the beginning of the laser development, almost all lasers were operating in continuous wave (CW) or long pulse (microsecond-level duration) mode. In the first significant step, the Q-switching technique, in which the cavity losses are increased to avoid lasing during pumping to accumulate a large population inversion many times the threshold inversion and are subsequently rapidly lowered to produce a gigantic laser pulse, was demonstrated for high intensity nanosecond (1 ns = 1×10^{-9} s) pulse laser generation. After a few years of development, the shortest laser pulse generated by Q-switching was still limited at the level of nanoseconds. Scientists started to seek other methods to achieve laser pulses with a shorter duration. In 1972, with the new technique of mode-locking [8] in an oscillator based on a

broad emission bandwidth dye material (Rhodamine 6G), the pulse duration was suddenly pushed to the level of picoseconds. The big step on the ultrafast pulse generation makes the mode-locking technique, in which the phase of the laser cavity longitudinal modes is locked, one of the key technologies in the development of ultrafast lasers. With the development of new laser materials with broader emission bandwidth, femtoseconds or even few-cycle ultrafast pulses were achieved by using the mode-locking technique.

In parallel with chasing shorter pulse duration, scientists also searched for methods to increase the pulse energy and average power of ultrafast pulses. In general, the maximum energy of laser pulses from the oscillator is limited by the beam size inside the laser cavity. Therefore, the concept of laser oscillator-amplifier sequence in which the beam exiting the oscillator is expanded to reduce the fluence was used to boost pulse energy. However, high energy pulses with a beam intensity exceeding the level of GW/cm^2 (1 GW = 10^9 W) lead to nonlinear effects that distort the beam and cause severe damages to the laser components. This limited the increase of laser peak power for nearly 20 years. In the mid-1980s, a technique called Chirped Pulse Amplification (CPA), in which pulses are stretched, amplified, and finally re-compressed, was presented by Donna Strickland and Gérard Mourou [9]. The implementation of CPA suddenly broke through the limitation of the peak power in ultrafast laser amplifiers. Since then, the peak power of ultrafast lasers rapidly increased and reached the level of petawatt (1 PW = 10^{15} W) peak power and 10^{22} W/cm^2 focused intensity in recent years [10]. The innovation of CPA technique was recognized by the Royal Swedish Academy of Sciences that awarded Donna Strickland and Gérard Mourou the 2018 Nobel Prize in Physics.

Following the fast development of the ultrafast lasers enabled by the demonstration of mode-locking and CPA techniques discussed in more detail below, the resulted high peak power and extreme brevity of high energy ultrafast laser pulses also provide the potentialities on a vast area of fundamental research and industrial applications, which stem from direct laser beam interactions with matters, or from interactions with matters of the secondary particle and high photon energy sources they drive. By focusing the high peak power laser pulses into a small area, electrons and

ions are accelerated into different physical regimes that exhibit different nonlinear behaviors in molecular (10^6-10^{12} W/cm^2), bound atomic electron (10^{12}-10^{18} W/cm^2), relativistic plasma (10^{18}-10^{24} W/cm^2), ultra-relativistic and even vacuum (>10^{24} W/cm^2) regions. These enabled the study of high harmonic generation (HHG), THz radiation generation, X-ray and Gamma-ray generation, electron and ion acceleration, neutron generation, attosecond (10^{-18} s) pulses, and filamentations [11]. There are also a variety of applications that depend on these secondary sources generated by the high-energy ultrafast laser, such as medical purposes, triggering and/or guiding of energy or electromagnetic waves, and supercontinuum generation [11].

Below I will discuss in more detail the two key technologies in the development of ultrafast lasers, which are the mode-locking technique and CPA technique.

Mode-Locking Technique

As mentioned above, the mode-locking technique is one of the key methods employed to generate ultrafast pulses. The principle of mode-locking technique can be described as follows. In a simple laser oscillator, each longitudinal mode within the lasing bandwidth oscillates independently building up from the spontaneous emission, and consequently the phase relationship between different longitudinal modes is random. CW or Q-switching pulsed operation can be achieved under this random phase condition. However, the shortest pulse duration will be limited at the level of nanoseconds. The mode-locking technique locks the longitudinal modes with a fixed phase. In this way, the longitudinal modes of the laser will periodically all constructively interfere with one another, producing a short intense pulse of light, as shown in Figure 1.2.

The longitudinal mode distance Δv is defined by the cavity geometry according to:

$$\Delta v = c/2nL \tag{1.1}$$

where L is the cavity length, c/n is the speed of light in the medium with refractive index n. For a given Δv, the more the number of longitudinal modes, the shorter the final output pulse. In another words, if there are N modes locked in a laser with a mode separation Δv, the overall mode-locked

bandwidth is $N\Delta v$. The relationship between this bandwidth $N\Delta v$ and the theoretical transform-limited pulse duration Δt is given by:

$$\Delta t = \frac{k}{N\Delta v} \tag{1.2}$$

where the constant k is the time-bandwidth product. As shown in Eq.(1.2), the larger this bandwidth value $N\Delta v$ is, the shorter the pulse duration from the laser could be potentially obtained. The time-bandwidth product is determined by the temporal shape of the pulse, for example, 0.441 for a Gaussian shape pulse, and 0.315 for a hyperbolic-secant-squared (sech^2) shape pulse that is often used to fit ultrafast laser pulses.

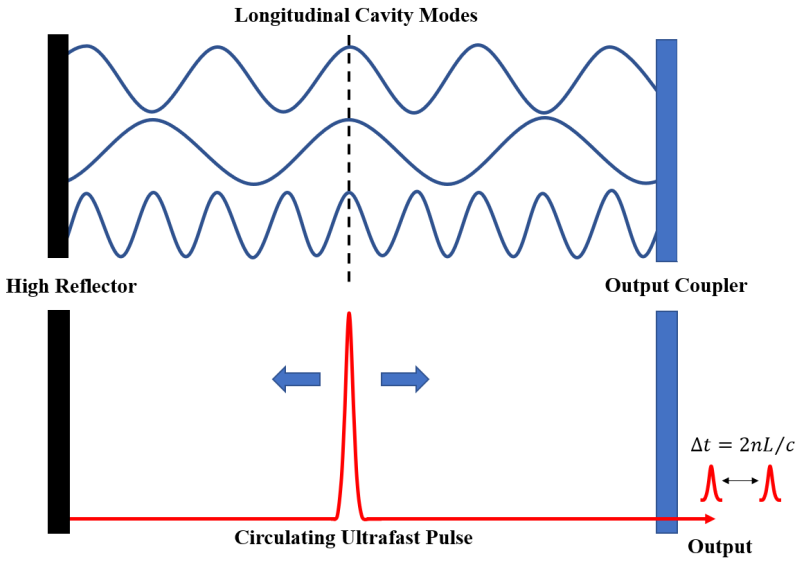

Figure 1.2: Illustration of mode-locking theory. Δt is the time between two consecutive pulses, $2nL$ is total traveled length in the oscillator, c is speed of light.

In general, to realize the mode-locking mechanism in a laser oscillator, either an active element (an optical modulator) or a passive element (a saturable absorber) needs to be used in the formation of ultrafast pulses. Based on the type of element used in the mode-locking technique, it can be described as active or passive mode-locking. In the active mode-locking, the periodic modulation of the losses or the phase changes is achieved with an acousto-optic or electro-optic modulator. With the synchronization between the modulation and oscillating round trips, the ultrafast pulse

width can be achieved, typically in picoseconds level. However, the active mode-locking is unable to support shorter pulses due to the slow active modulation speed of the modulation device. On the contrary, the passive mode-locking allows the generation of much shorter (femtosecond) pulses, as the modulation speed of the saturable absorber is much faster than the speed of active modulation units. There are different types of saturable absorbers for passive mode locking, including semiconductor saturable absorber mirror (SESAM), quantum dots, and artificial saturable absorbers based on nonlinear effects (e.g., Kerr lens mode locking). For most ultrafast oscillators based on solid-state material, the Kerr lens mode locking technique is the most widely adopted method since the stable mode-locking operation is achievable without the requirement of a visible saturable absorber device.

Kerr Lens Mode-Locking

The Kerr lens mode-locking technique takes advantage of the Kerr lensing effect in the gain material to lock the phase of longitudinal modes. When a short laser pulse propagates through a nonlinear medium, the Kerr effect leads to a phase delay that is the largest on the beam axis, where the intensity is the highest, and smaller off-axis. The phase delay is related to the change of refractive index according to:

$$n(I) = n + \Delta n = n + n_2 I \tag{1.3}$$

where n is the low intensity zero order refractive index of the material, and Δn is the modified refractive index. In this expression, n_2 is the nonlinear index, and I is the optical intensity. As a result, due to the uneven intensity distribution across the beam, the Kerr effect is similar to the behavior of a lens whose focal length is intensity dependent, as shown in Figure 1.3. There are two different mechanisms of achieving mode locking with the Kerr lensing effect, one is hard aperture Kerr lens mode-locking where an iris is applied into the oscillator cavity as the hard aperture, and the other is soft aperture Kerr lens mode locking where the pumped area in the gain material is acting as the soft aperture. As the beam passes through the aperture, the high-intensity portion of the pulse will maintain enough gain on each pass through the gain media, but the low-intensity

portion (CW or long pulse) will suffer high losses and finally decay. After the round-trip oscillation inside the laser cavity, the phases of different longitudinal modes are locked, a stable mode-locked short laser pulse is produced.

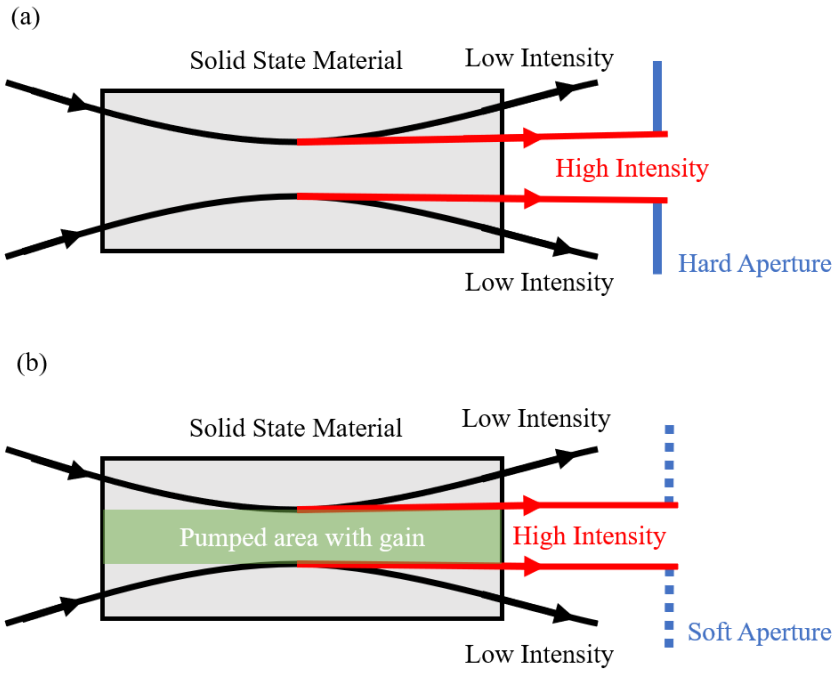

Figure 1.3: Illustration of (a) equivalent hard aperture and (b) equivalent soft aperture in Kerr lens mode locking. Black ray represents low intensity portion associated with larger losses; red ray represents high intensity portion associated with fewer losses.

By using the Kerr lens mode-locking technique with a broad emission bandwidth laser material such as Ti:Sapphire, the laser oscillator can easily generate sub-100 fs pulses. Compared with the previous generation mode-locking dye laser, the Ti:Sapphire Kerr lens mode-locking laser can generate a shorter pulse duration with less complexity for the mode-locking operation. As a result, the dye laser was quickly replaced by Ti:Sapphire laser, which became the laser of choice for generating femtosecond pulses until today. In 1995, by using chirped dielectric mirrors, an 8 fs Ti:Sapphire oscillator was demonstrated [12]. A while later, 5 fs pulses were directly generated with a spectrum wavelength from 600-1200 nm, which set the record for the broadest bandwidth and shortest pulses directly from a laser oscillator [13].

CPA Technique

In addition to the mode-locking technique, the technique of chirped pulse amplification (CPA) plays a critical role in the development of ultrafast lasers. For ultrafast laser amplifiers, as the pulse energy gets boosted to a higher level, the high peak power can become a problem. The exceeding GW/cm^2 level beam intensity will cause severe damage to the optical components through nonlinear processes such as self-focusing, which is quantitatively defined in term of a B-integral:

$$B = \frac{2\pi}{\lambda} \int n_2 I(z)\, dz \tag{1.4}$$

where n_2 is the nonlinear index, *I(z)* is the optical intensity along the beam axis, z is the position in beam direction. As n_2*I(z)* is the nonlinear change in the refractive index, one can easily recognize the B-integral to be the total on-axis nonlinear phase shift accumulated in a passage through the amplifier. If the B-integral becomes larger than 1, for example at the level of 3-5, self-focusing will occur due to the modified refractive index distribution in the beam wavefront plane. In this case, the higher optical intensities on the beam axis, as compared with the wings of the spatial intensity distribution, cause an effectively increased refractive index for the inner part of the beam. Then, due to the Fermat's principle, the beam itself acts like a focusing lens. As a result, the beam diameter of the high B-integral beam is decreased compared with that of a low B-integral beam. The threshold of self-focusing in terms of the B-integral depends on conditions such as the wavelength of the beam and the n_2 of the materials. In some high peak power cases, the beam will even self-focus as it propagates through air, not only damaging the subsequent optical surfaces but also forming a plasma or filament propagation, which will degrade the beam qualities and make it impossible to get the beam amplified in the following amplifier stage(s), or to focus it into a diffraction-limited spot. For a long period, the ultrafast laser's pulse energy and peak power were limited at such relatively low level.

To amplify ultrafast laser pulses to high energy, one of the methods to avoid the damage is to enlarge the beam size to maintain the beam intensity at a safe level. However, in the case of

ultrashort pulses, the beam size can rapidly scale to impractical sizes which cannot be achieved because of the cost of the system and availability of large-aperture optics.

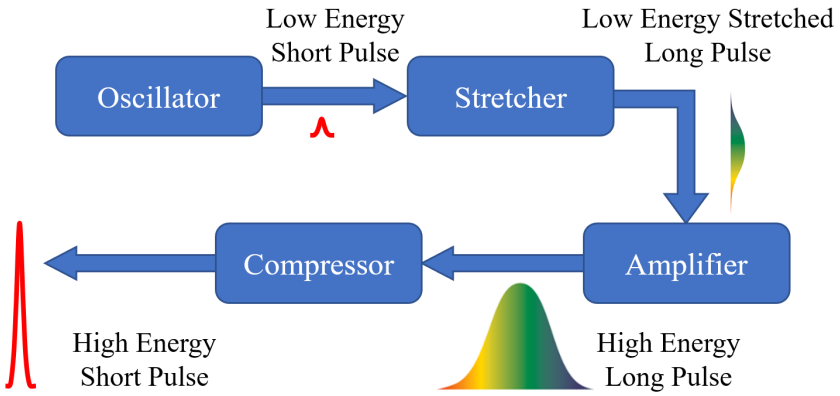

Figure 1.4: Illustration of the CPA theory.

In the mid-1980s, a technique called Chirped Pulse Amplification (CPA) was presented by Donna Strickland and Gérard Mourou [9], which overcame the limitation to the maximum peak power that could be achieved in laser amplifiers. Instead of only enlarging the beam size of the high-energy ultrafast pulse to keep the beam intensity in the safe range, the CPA technique is a strategy that manipulates the temporal profile of the pulse before and after the amplification process. As shown in Figure 1.4, a low energy zero-chirp short pulse from an oscillator can be first stretched out in time by chirping the pulse via a stretcher before being introduced into the amplifier(s). After going through the stretcher, the laser pulse can have a pulse duration that is a factor of 1000 to 100000 larger than the original pulse. As a result, the amplified beam can reach higher energy with a high extraction efficiency while maintaining a safe intensity level on all optical components in the system. The obtained high energy long pulse can be compressed after amplification by applying the opposite dispersion to that imposed by the stretcher, which results in high energy short pulse with high peak power.

Compared with the traditional master-oscillator power-amplifier (MOPA) configuration, the key to the CPA technique is the use of dispersive elements as stretcher and compressor, such as

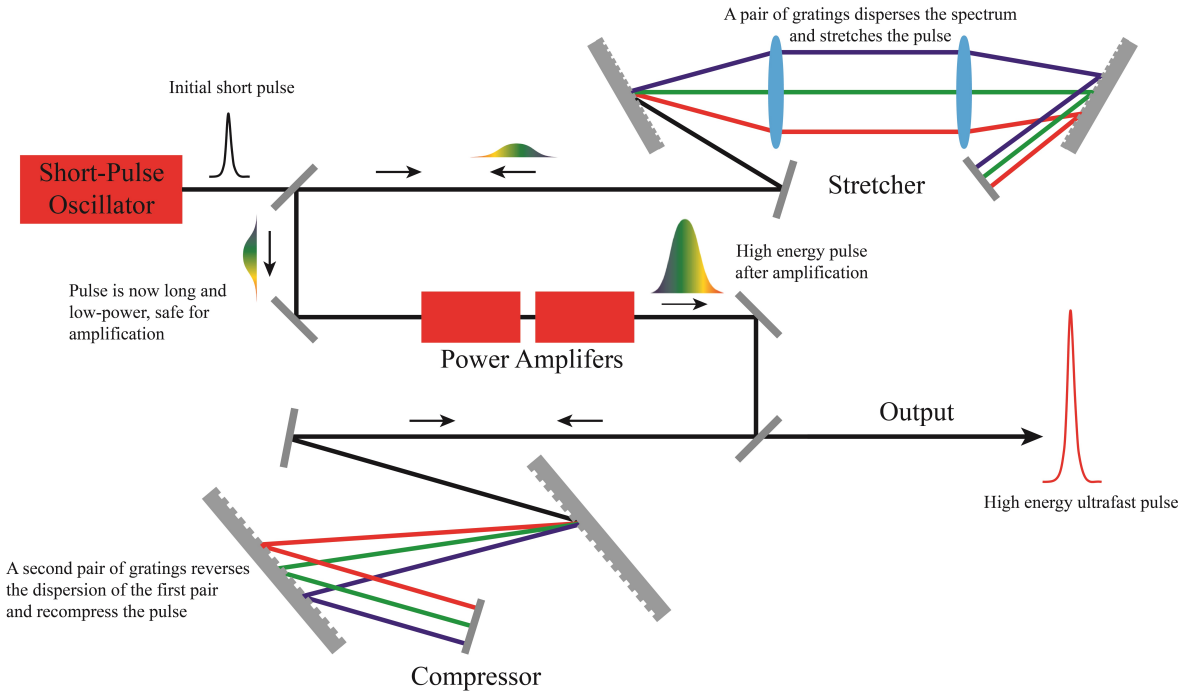

Figure 1.5: Illustration of the CPA technique in the laser system.

a pair of diffraction gratings, a pair of prisms, optical fibers, and dispersive multi-layer coatings (chirped mirrors). In a typical CPA system, shown in Figure 1.5, a broadband short pulse from a mode-locked oscillator normally has zero spectral chirp, which means the high-frequency and the low-frequency components of the laser pulse travel simultaneously in time. By applying normal dispersion in the stretcher, the low-frequency component of the zero-chirp pulse travels a shorter path than the high-frequency component. Therefore, the laser pulse becomes positively chirped, which means that the high-frequency component lags behind the low-frequency component, resulting in a long duration pulse (typically hundreds of picoseconds to a few nanoseconds in high intensity lasers). The higher the amount of applied dispersion, the longer the pulse duration can be achieved. In the amplification process, since the pre-applied dispersion is much higher than the dispersion in the normal materials, the change of pulse duration is small as the pulse energy increases. Finally, in the compressor, the same amount of negative dispersion is applied to the beam. The low-frequency component on the leading edge travels a longer path than the high-frequency component. As a result, the low-frequency component and high-frequency component travel si-

multaneously in time again. The short zero-chirp pulse is obtained again but with higher peak power and with higher pulse energy.

The basic principle of stretching or compressing the pulse duration is to manipulate the optical path difference between the longer wavelength component and the shorter wavelength component in a laser pulse using dispersive elements such as prisms or diffraction gratings. In the case of the grating pair, the diffractive angle is a function of the wavelength such that a delay can be generated between different wavelength components. The relationship between the grating spacing and the angles of the incident and diffracted beams is known as the grating equation. If the incident angle of a plane wave is at any arbitrary angle θ_i, the grating equation can be presented as:

$$\sin\theta_i - \sin\theta_m = \frac{m\lambda}{d} \tag{1.5}$$

where the integer *m* is the propagation-order of interest, λ is the wavelength of the incident light, *d* is the grating spacing, and θ_m is the diffracted angle of the light at diffraction order *m*. Simply rewrite the Eq.(1.5), the diffracted angle θ_m can be expressed as:

$$\theta_m = \arcsin(\sin\theta_i - \frac{m\lambda}{d}) \tag{1.6}$$

For the zero diffraction order, where *m=0*, the diffracted angle θ_m is equal to the incident angle θ_i. However, for the non-zero diffraction order, for example, *m=1*, the diffracted angle θ_m is related to the wavelength of the beam and the grating spacing for a certain incident angle. Considering the light with multi-wavelength components with an incident angle of θ_i, the short wavelength component could have a larger diffracted angle θ_m at the surface of grating, and vice versa. As a result, this difference in diffracted angle between the longer wavelength component and shorter wavelength component can be used to generate optical path difference (OPD). By using another grating with the same groove spacing to combine different wavelength components back to the same output angle, a positively or negatively chirped laser pulse could be achieved with a beam quality close to that of the original beam. By using the grating pair in an opposite way,

the positively or negatively chirped laser pulse could be compressed back into a zero-chirp short pulse. The longer the distance between the two gratings, the larger the optical path difference generated between the different wavelengths, which means the grating pair provide a larger group delay dispersion (GDD), defined as:

$$GDD = GVD \times length \tag{1.7}$$

where the GVD is the group velocity dispersion, which is defined as the derivative of the inverse group velocity with respect to frequency:

$$GVD = \frac{\partial}{\partial \omega}(\frac{1}{v_g}) = \frac{\partial^2 k}{\partial \omega^2} \tag{1.8}$$

where ω are angular frequency, *k* is the wave number:

$$k = \frac{2\pi}{\lambda} \tag{1.9}$$

As can be seen from Eq. (1.7), with a certain GVD dispersive material, the distance that the pulse passing through will determine the amount of GDD applied to the stretching or compressing process. As for other dispersive elements, for example an optical fiber, the GVD is determined by the properties of the fiber material. If GVD>0, the fiber is called normal dispersion fiber, and in contrast when GVD<0, the fiber is called anomalous dispersion fiber. As a result, as a zero-chirp pulse passing through a normal dispersion fiber, normal dispersion will be accumulated in the pulse, which means the shorter wavelength components will suffer a larger optical path and the longer wavelength components will experience a shorter optical path. Therefore, a separation between the longer and shorter wavelength components can be achieved, and results in a stretched pulse. The length of the fiber determines the amount of GDD applied to the pulse, which can result in different pulse duration with the management of dispersion.

In the first demonstration of the CPA system in 1985, a 1.4-km optical fiber was used to provide the positive dispersion to stretch the about 60 nJ, 1 μm pulses generated by a mode-locked Nd:YAG oscillator [9]. Subsequently, the stretched 300 ps pulse was safely amplified in a regenerative amplifier to a pulse energy of 2 mJ. After amplification, a grating pair with negative dispersion which was first presented by E. B. Treacy in 1969 [14], was used to compress the high energy pulse [9]. As a result, a near zero-dispersion pulse was obtained with a pulse duration of 2 ps and an energy of 1 mJ. A further upgrade to the CPA technique was achieved by using a stretcher also based on a pair of gratings that can better compensate for the dispersion of the compressor. This was achieved by introducing a pair of lenses between the gratings, as was first demonstrated by O. E. Martinez [15]. With the capability of providing variable positive dispersion with a very compact design, this stretcher geometry quickly became a standard choice for the stretcher in CPA systems, as shown in Figure 1.5. The Martinez stretcher configuration offers a convenient way that the stretched ultrafast pulses can be precisely compensated by the grating compressor, which has largely benefited the CPA ultrafast laser system for the past decades. Looking back at the development of ultrafast lasers, the birth of the CPA technique revolutionizes the entire field of ultrafast lasers and many extraordinary discoveries have become possible since then, justifying the 2018 Nobel prize in Physics to Strickland and Mourou [16].

1.3 Current Status of High Energy Ultrafast Laser

The competition to achieve higher pulse energy and higher average power started several decades ago. However, the repetition rates of the high energy, high peak power, ultrafast laser facilities are still relatively low, typically only generating one pulse every second, minute, or even longer. The worldwide status of high power ultrafast lasers is summarized in Figure 1.6. In general, we can notice two type of lasers: those operating with highest peak power (i.e. PW-class) but low average power and repetition rate of less than 10 Hz, and those operating at high average power (i.e. up to kW) and kHz repetition rate but much lower peak power. The first class is dominated by Ti:Sapphire lasers, and the second by Yb-doped lasers. The highest repetition rate PW lasers

in the world currently operate at 3.3 Hz, be 0.85 PW laser at Colorado State University (CSU) [17] and the HALPS laser installed at the Extreme Light Infrastructure (ELI) in Europe, that has been operated at 0.5 PW and is planned for operation at 1 PW peak power at 10 Hz repetition rate [18]. Even though these low repetition rate high peak power ultrafast lasers allow for pioneering proof of principle experiments. There are many applications such as high average power high energy photon and particle sources that require operation at a high repetition rate.

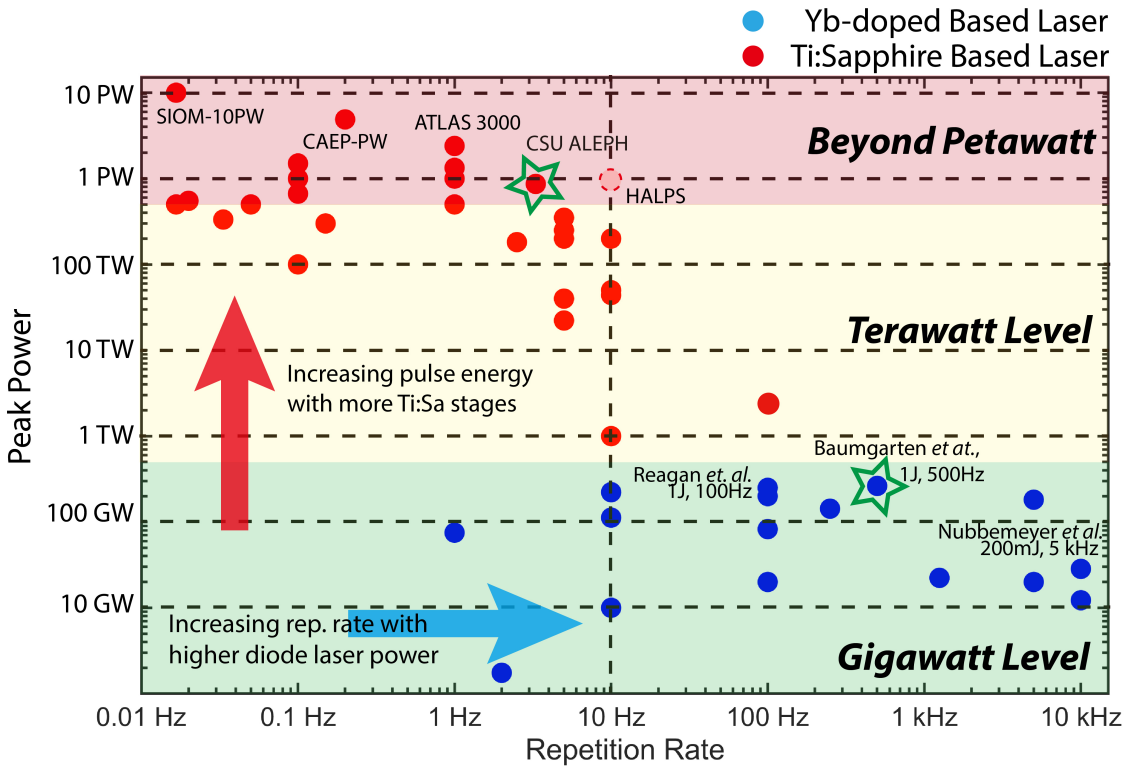

Figure 1.6: The summary of worldwide high peak power ultrafast lasers. The lasers in the green stars are from CSU. Data from Ref.[10] and Ref.[82].

The pulse energy of ultrafast lasers is presently limited to tens of millijoules for operating at 1 kHz repetition rate, or to a few hundred millijoules for 100 Hz repetition rate. Table 1.1 shows a summary of the currently reported laser systems with energy >10 mJ and repetition rate >100 Hz and femtoseconds pulse duration (<300 fs). As indicated in Table 1.1, until now, the average power of high repetition rate (>100 Hz) high energy (>10 mJ) ultrafast lasers is still limited under tens of Watts. The highest pulse energy, which is 220 mJ, was achieved by R. Clady et al. from

Aix-Marseille University in 2018 [19]. This 100 Hz repetition rate, 9.5 TW peak power result was reached with four multi-pass Ti:Sapphire amplifier stages, and the last cryogenically cooled amplifier required ten individual 100 mJ pulse energy 100 Hz repetition rate frequency-doubled (λ=532 nm) Nd:YAG lasers as the pump source. In another result listed in Table 1.1, a 1 kHz repetition rate Optical Parametric Chirped Pulse Amplification (OPCPA) laser system achieving compressed sub-9 fs pulses of 53 mJ energy was reported by R. Budriūnas et al. in 2017 [20]. The seed laser was amplified by four consecutive OPCPA stages with total green pump energy of 336 mJ at 1 kHz, which was frequency-doubled from the output of a system with ten Nd:YAG amplifiers. The same group reported 34 mJ pulses with a shorter pulse duration in 2019 [21]. Significant efforts to develop even higher energy and higher average power ultrafast lasers are underway worldwide. One aspect of the effort is the development of the final amplifier stage and gain materials. The other is the implementation of pump sources with sufficient energy at a high repetition rate.

Table 1.1: Summary of the high repetition rate (>100 Hz) high energy (>10 mJ) ultrafast lasers [19–25].

	Y. Nabekawa, et al. [19]	**R. Clady, et al. [20]**	**A. Golinelli, et al. [21]**	**R. Budriūnas, et al. [22]**	**T. Stanislauskas, et al. [23]**	**Tiago de Faria Pinto, et al. [24]**	**R. Antipenkov, et al. [25]**
Year	2010	2018	2019	2017	2019	2019	2019
Compressed Pulse Energy	40 mJ	220 mJ	16 mJ	53 mJ	34 mJ	10.5 mJ	Achieved > 20 mJ Designed > 100 mJ
Repetition Rate	100 Hz	100 Hz	1 kHz	1 kHz	1 kHz	100 Hz	1 kHz
Average Power	4 W	22 W	16 W	53 W	34 W	1 W	Achieved > 20 W Designed > 100 W
Compressed Pulse Duration	12 fs	23 fs	17.8 fs	sub-9 fs	6.3 fs	220 fs	Designed < 20 fs
Peak Power	3.3 TW	9.5 TW	0.9 TW	5.5 TW	5.4 TW	0.05 TW	
Final Stage Technique	Multi-Pass Ti:Sa	Multi-Pass Ti:Sa	Multi-Pass Ti:Sa	OPCPA	OPCPA	OPCPA	OPCPA

1.3.1 The Generation of High Power High Energy Ultrafast Pulses

In general, there are two types of final amplifier stage(s) generating high energy (>10 mJ) high repetition rate (>100 Hz) ultrashort pulse duration (<300 fs). The first one is to implement the broadband gain media in multi-pass amplifiers in the CPA system, such as Ti:Sapphire, where the seed pulses extract the stored energy on the upper laser level via passing through the gain media. The second way is to use the OPCPA system, where the energy of the pump gets converted to the seed pulse through the nonlinear effect within nonlinear materials.

CPA System with Broadband Gain Materials

The first method has been widely used because of the natural advantages of Ti:Sapphire material. Ti:Sapphire is one of the most important laser materials in modern ultrafast laser. It consists of Ti^{3+} ion dopant in a sapphire host [26]. Both the properties of Ti^{3+} ion and the sapphire host offer great advantages for high power ultrafast lasers. The Ti^{3+} ion has a very broad emission bandwidth, ranging from 660 to 1180 nm, as shown in Figure 1.7, which could support laser pulses to achieve the duration of a few femtoseconds. Ti^{3+} ion's absorption band is also wide, ranging from 450 to 550 nm, which would bring flexibility to the pump source selection. Additionally, the excellent thermal and mechanical properties of the sapphire host are another reason for Ti:Sapphire's success. The thermal conductivity of sapphire is around 40 W/(m·K) at room temperature, which is higher than most of the laser material hosts. Besides, its thermal conductivity dramatically increases as the temperature decreases and reaches about 1000 W/(m·K) at 77 K [27]. The trend is not affected much by the doping concentration of Ti^{3+} ions. The high thermal conductivity of the sapphire host provides the necessary advantage that a high-power laser requires, and it has been proven to widely benefit the development of power scaling of the ultrafast laser.

Ti:Sapphire has some disadvantages as ultrafast laser gain material. One of the drawbacks is the short upper laser level lifetime, about 3.2 µs. The upper laser level lifetime and peak power of the pump source determine the maximum stored energy that could be extracted by seed pulses. As a result, high-energy short-pulse-width pump sources are required in generating high-energy pulses from Ti:Sapphire-based laser. Another drawback is its high quantum defect, which leads to a high

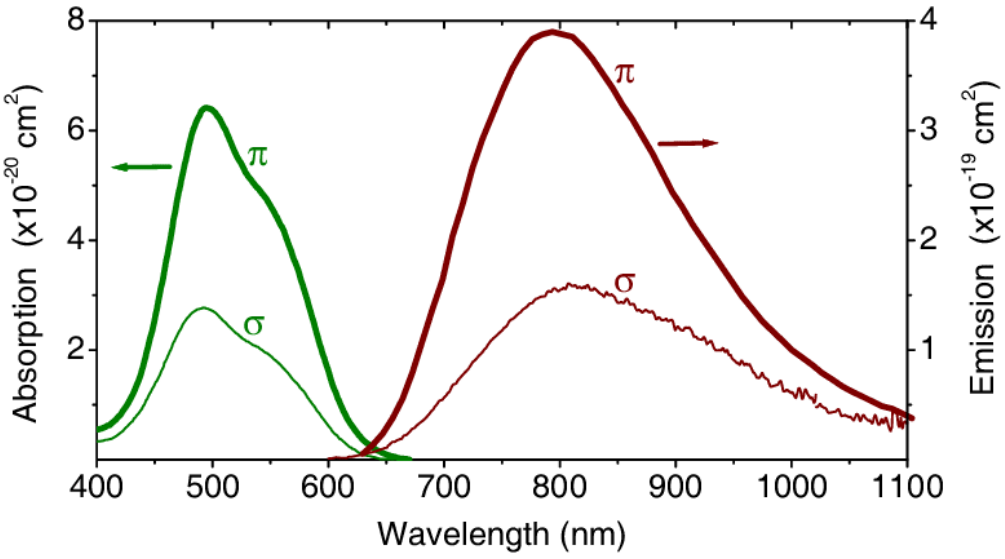

Figure 1.7: Absorption and emission cross-sections of Ti:Sapphire [28].

amount of thermal power during the lasing process. This would result in serious thermal effects at high average power operations. However, benefiting from sapphire's high thermal conductivity, the thermal power could be extracted through the effective heat dissipation design to mitigate the thermal effects.

The typical design of Ti:Sapphire CPA amplifier system uses a Ti:Sapphire front-end laser with broad-spectrum bandwidth to provide enough seeding energy before the amplifier stage(s). Then the Ti:Sapphire multi-pass amplifier(s) is applied to boost the energy to the desired level. The advantages of the Ti:Sapphire multi-pass amplifier(s) are the high optical-to-optical efficiency and the freedom of time synchronization between the pump and seed beam. The disadvantages, however, are the gain narrowing effect and high quantum defect that lead to the relatively long pulse duration (on the level of 25 fs) and the unavoidable thermal effects in the amplifier, respectively.

Alternatively, some Yb-doped materials with broad emission bandwidth could also be considered for the broadband gain media in a multi-pass amplifier, such as Yb:CaF_2, Yb:CALGO, and Yb:KYW/Yb:KGW. Even though the broadband Yb-doped materials such as Yb:CALGO and Yb:CaF_2 have shown the ability to generate sub-100 fs pulse [29, 30], the highest reported energy results of Yb-doped femtosecond lasers are still limited to a few millijoules with kHz level repetition rates [31]. As for other mature Yb-doped materials such as Yb:KYW and Yb:KGW,

the emission bandwidth is not as broad as Yb:CALGO. The shortest pulse duration reported with millijoule-level pulse at kHz repetition rates is on the level of 300 fs [32]. If further amplifying the pulse energy with Yb:KYW or Yb:KGW, the supported shortest pulse duration would be increased to the 500-fs level due to the gain narrowing effect [33, 34], which requires much higher energy to reach the same peak power than with pulses with tens of femtoseconds duration. Furthermore, the low gain factor and thermal conductivities will suppress the power scaling with broadband Yb-doped materials. To reach a shorter pulse duration, a nonlinear-effect-based spectrum broadening process is needed to broaden the spectrum of pulse after the final amplification. However, this process loses a substantial portion of energy in the beam coupling and brings problems such as system complexity, repeatability, and cost. In summary, the main reason for not widely applying the Yb-doped material as the last amplifier stage for ultrafast lasers is because of the restriction on pulse duration, along with the disadvantage of low thermal conductivities of gain materials and the system complexity in the spectrum broadening process.

OPCPA System with Nonlinear Materials

For the second method, the OPCPA amplifier system is combined with CPA technology and the nonlinear process to convert the pump energy into the seed (Optical Parametric Amplification, OPA) rather than the classical stimulated emission amplifier. In the OPA process, the signal pulse propagates through the nonlinear crystal together with the pump pulse in shorter wavelengths. Under the phase matching conditions, the energy of the pump is converted into the signal pulse and a so-called idler pulse as the pulses propagate through the nonlinear crystal simultaneously. This nonlinear-effect-based amplification offers a wide selection of seed wavelengths. Therefore, the gain narrowing effect during amplification is negligible. As a result, compared with the typical pulse duration (25 fs) from Ti:Sapphire amplifier system, the OPCPA system could reach less than 10 fs, which helps to increase the peak power with the limited pulse energy [10]. Apart from the advantage in spectrum bandwidth, the thermal effect in OPCPA system is much weaker than Ti:Sapphire amplifier since only a small amount of heat is generated due to weak parasitic absorption. Even with these advantages, the challenge of the OPCPA system is still complicated.

Because of the nature of the phase-matching process, the energy conversion only happens during the time of the pump. The requirement on pulse duration of the seed and pump is therefore rigid, as well as on their temporal synchronization. As a result, the high energy pump pulse with a short duration is also a restrictive requirement for high energy ultrafast pulse generation with OPCPA system. Besides, the requirement on the beam quality of pump beam profile is high for the nonlinear process compared with traditional amplifiers. Other than the above-mentioned challenges, the phase-matching issues in each case also need to be considered.

In summary, these two methods have distinct advantages and disadvantages as the final amplifier stage of high energy high average power ultrafast laser, and both have been demonstrated in high peak power ultrafast laser generation. The critical limitation for scaling up average power and pulse energy of the ultrafast laser is not the amplification methods. As indicated by previous work, the availability of high repetition rate high energy pump sources poses a critical limit to all kinds of high peak power ultrafast lasers to reach a higher repetition rate and to benefit more applications. In the next section, the limitation of the traditional ultrafast laser on increasing the repetition rate will be discussed, and the potential solution for a high repetition rate high energy ultrafast laser will be proposed.

1.4 Limitations of the High Energy Ultrafast Laser on Increasing Repetition Rates and Potential Solutions

The leading approach to generate high-energy green pulses to pump Ti:Sapphire and OPCPA ultrashort pulse lasers is by frequency doubling the $\lambda = 1\,\mu m$ wavelength solid-state lasers in a nonlinear optical crystal. As the most widely used high energy $\lambda = 1\,\mu m$ laser, the flashlamp-pumped Nd:glass and Nd:YAG laser have been the first choice because of their high pulse energy and their mature geometry. However, the high repetition rate is a challenge for the high-energy operation of flashlamp-pumped Nd-doped lasers. The first reason is that the electrical charging time of the capacitors that drive the flashlamps is inversely proportional to the charging supply power. The second is the mismatch between the flashlamp (typically Xe) spectrum and the absorption of Nd

ions in the gain medium. In addition, in the case of glass, the poor thermal conductivity leads to a high thermal gradient that degrades the beam quality that ultimately can cause failure.

The development of high-power diode lasers has made it possible to solve the spectrum mismatch problem, contributing to greatly decrease the heating problem. Selecting diode lasers emitting at a wavelength that matches one of the laser material's absorption bands can largely increase the optical-to-optical efficiency compared to the flashlamp-pumping. Another advantage of diode lasers is their compact size. After assembling several diode bars into a stack, as shown in Figure 1.8, extremely high average powers can be achieved. With a stack of diode laser bars and a well-designed beam-shaping system, the peak power delivered onto the solid-state laser gain material can reach several kilowatts or higher [35].

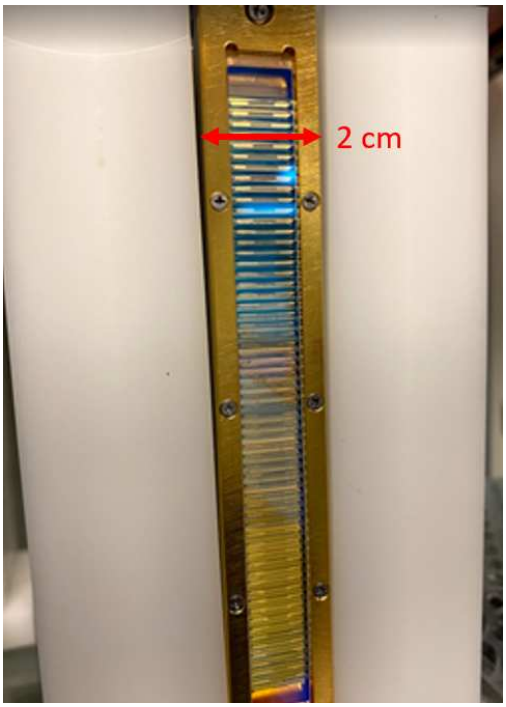

Figure 1.8: A 60-bar diode laser assembly that can generate 6 kW peak power.

With the development of high-power diode lasers, high gain Nd-doped materials logically became the choice for the first generation of diode-pump solid-state laser (DPSSL). However, laser sources providing Joule-level pulse energies at kilohertz repetition rate were still not available.

This is mainly because of the short upper laser level lifetime of the Nd-dope material (e.g., about 230 µs for Nd:YAG [36]). For example, storing 1 J energy on the upper laser level with a lifetime of 200 µs requires at least a peak power of 5 kW pump laser, without considering any loss. The currently available 100 Hz level Nd-doped lasers can provide 250 mJ level output energy [37, 38]. However, it has not been possible to increase their repetition rate to the next level while maintaining the pulse energy, which is normally limited at the level of 100 mJ at a repetition rate of 1 kHz [39]. Furthermore, the above specifications only consider the pulse energy generated at λ = 1 µm whereas another 20-40% loss in energy would be introduced by the subsequent second harmonic generation (SHG) process for green pulse generation.

Regarding the possibility of directly pumping high energy ultrafast laser systems using the green diode lasers, the peak power of the currently available diode laser is still several orders of magnitude away from those required. As discussed above, all the currently available pump sources are unable to provide sufficient pump energy for the high energy (i.e., >250 mJ) ultrafast laser working at 1 kHz repetition rate. In the next section, we will present a promising scalable solution to this problem.

1.4.1 Yb:YAG Lasers

An efficient, scalable solution for the generation of high-energy green pulses at high repetition rates is the frequency-doubling of λ = 1 µm lasers based on Yb-doped materials. Several of these gain materials have good optical, thermal, and mechanical properties. The advantages of Yb-doped materials are indicated in Figure 1.9, where the energy level diagrams of Nd^{3+} and Yb^{3+} ion are compared. In both materials, lasing occurs at wavelengths around 1 µm, in transitions between the $^4F_{5/2}$ and $^4I_{11/2}$ manifolds in Nd^{3+}, and between the $^2F_{5/2}$ and $^2F_{7/2}$ manifolds in Yb^{3+}. The main difference is that the Yb-doped materials have a lower quantum defect, resulting in less heating power under the same amount of absorbed pump power [40]. For example, the Yb-doped YAG material (Yb:YAG) absorbs at wavelengths around 940 nm and 970 nm and lases at 1030 nm. Therefore, the quantum defect of Yb:YAG is only 8.7% for 940 nm and 6% for 970 nm,

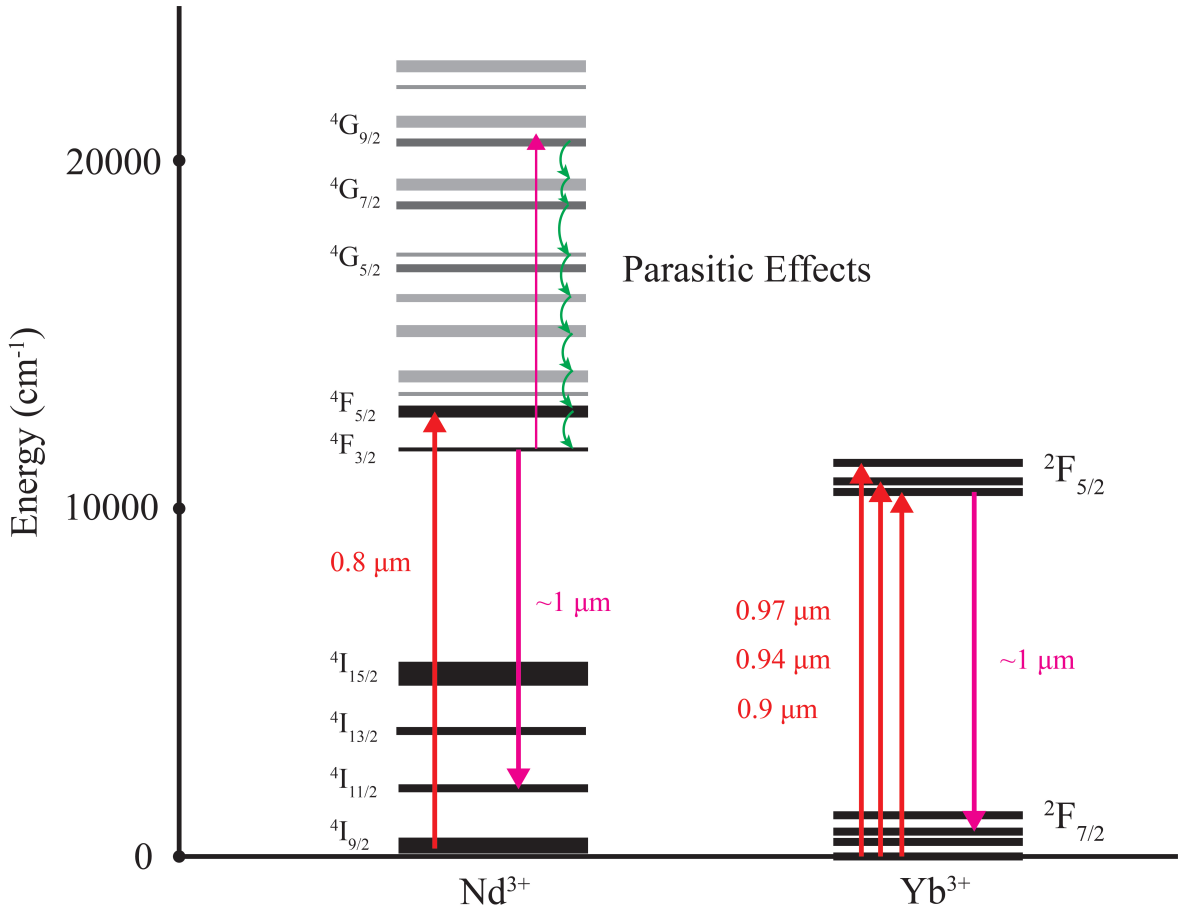

Figure 1.9: The relevant energy levels of Nd^{3+} and Yb^{3+} gain media with typical pump and lasing transitions, as well as parasitic effects [40].

much lower than the 24% quantum defect of Nd:YAG. With the same amount of pump energy absorbed, the Yb-doped lasers have about three times lower heating power compared to Nd-doped lasers, which can be used to dramatically increase the laser average power. In addition, as shown in Figure 1.9, the simplified energy level in Yb^{3+} benefits the Yb-doped laser to avoid parasitic effects such as up-conversion, excited-state absorption, and cross-relaxation, which occur in Nd-doped media because of the existence of higher energy levels [40]. The main de-excitation paths from the high levels in Nd^{3+} are predominately non-radiative and contribute to thermal loading. These parasitic effects also contribute to depopulate the laser upper level, reducing the population inversion and gain. With an upper laser level lifetime of about 1 ms, Yb-doped materials can be efficiently pumped with commercially available high-power diode lasers. Compared to the about 230 µs upper-level lifetime in Nd:YAG, the peak power required from the diode laser to produce a certain population inversion is five times lower.

As for the host material, there are numerous selections for Yb^{3+} ion other than YAG, such as KYW, KGW, YLF and CaF_2, which provides various choices for different laser output parameters, and that have pump requirements [33, 40–44]. Table 1.2 is a summary of the main properties of several selected Yb-doped gain materials. Among all these, Yb:YAG stands out for high power laser generation, not only because of Yb:YAG's overall good optical properties but also YAG's good mechanical and thermo-optical properties, especially at cryogenic temperature.

Although the thermo-optical and mechanical properties of YAG are good compared with other host materials at room temperature, these properties are further improved at cryogenic temperature (at 77 K, the boiling temperature of liquid nitrogen (LN2) at 1 atm) [41, 45–47]. As listed in Table 1.3, the thermal conductivity of Yb:YAG at room temperature is 8.6 W/(m·K). As the temperature decreases, the thermal conductivity increases dramatically to around 60 W/(m·K) at cryogenic temperature, which leads to a better heat dissipation under high-power operation. This improvement is reduced as the Yb-doping concentration increases, but the increase in thermal conductivity is still significant at the concentrations typically used (i.e., 1-10%). The thermo-optic coefficient and expansion coefficient also become more favorable as the temperature decreases to

Table 1.2: Spectroscopic of various Yb-doped materials at room temperature [33, 40–44]. λ_e for emission center wavelength; λ_{abs} for absorption center wavelength; $\Delta\lambda_e$ for emission FWHM bandwidth; σ_e for emission cross-section coefficient; τ_e for upper laser level lifetime; κ for thermal conductivity.

Yb-doped Materials	λ_e (nm)	λ_{abs} (nm)	$\Delta\lambda_e$ (nm)	σ_e (10^{-20} cm^2)	τ_e (ms)	κ (W/m·K) (undoped)
Yb:YAG	1030	941	11	2.1	0.95	8.6
Yb:KYW	1025	981	16	3	0.6	3.3
Yb:KGW	1023	981	20	2.8	0.6	3.3
Yb:YLF	1017	959	>30	0.75	2.08	5.2
Yb:CaF_2	1049	980	70	0.17	2.4	9.7

77 K. The thermo-optic coefficient decreases by about eight times at 77 K, which mitigates the thermal effects as well. The gain-related properties also get improved at cryogenic temperature. The energy level diagram of Yb:YAG changes from the quasi-three-level system to a four-level system. In the case of the quasi-three-level system, because the lower laser level is very close to the ground state, the population inversion can only happen as more than half of the ions are pumped into the upper laser level, which results in a smaller emission cross-section coefficient. On the contrary, for cryogenic temperature Yb:YAG, the lower laser level of the four-level system is well above the ground state and is quickly depopulated, which leads to an increase in emission cross-section compared to that at room temperature. As a result, the saturation fluence drops by more than five times at 77 K, from 9.2 J/cm^2 to 1.7 J/cm^2. This decrease in saturation fluence allows for efficient energy extraction without optical damage to the coatings and bulk materials. The associated increase in gain also allows for efficient energy extraction in a small number of passes through the gain media, which helps to avoid high nonlinear phase accumulation and thermal effects. Besides, the bandwidth narrowing effect at 77 K benefits the reduction of reabsorption at 1030 nm.

Nevertheless, while cooling to 77 K significantly improves most properties of Yb:YAG, there are also some disadvantages. The most apparent drawback is bandwidth narrowing. The full width

Table 1.3: Optical and mechanical properties of Yb:YAG at room temperature and at liquid nitrogen temperature. The column on the right quantifies the change. Values according to Refs [41, 45–47].

Yb:YAG properties at room and cryogenic temperature	At 300 K	At 77 K	Factor
Thermal Conductivity (W/m·K)	8.6	60	$\times 7$
Thermal-optic coefficient (10^{-6}/K)	7.8	0.9	$\times 1/8$
Expansion coefficient (10^{-6}/K)	6.14	1.95	$\times 1/3$
Saturation fluence (J/cm^2)	9.2	1.7	$\times 1/5$

half maximum (FWHM) emission bandwidth of Yb:YAG at room temperature is about 5 nm at the center of the 1030 nm line [40], which can support several hundred femtoseconds pulse duration. At 77 K, the FWHM emission bandwidth is narrower than 1 nm, which in practice only supports pulses of a few picoseconds in duration. However, this is not a problem when the laser is used as the pump source of ultrafast lasers.

1.4.2 Status of Yb:YAG High Average Power Lasers

The current state-of-the-art diode-pumped Yb-doped lasers at λ = 1.03 µm with >10 mJ pulse energy and repetition rate >10 Hz are summarized in Figure 1.10 [34, 48–70]. In this figure, the horizontal axis represents the repetition rate from 10 Hz to 10 kHz, and the vertical axis indicates the pulse energy. As the product of pulse energy and repetition rate, the diagonal lines indicate increased average power from 1 W to over 10 kW. Different gain medium geometries have been used to manage the thermal load under the high average power pumping, including slabs, thin disks, and thick disks operating at cryogenic temperatures. Most of the kilowatt level average power Yb:YAG lasers operate at a high repetition rate with relatively low pulse energy. These include the thin disk laser operating at 300 kHz repetition rate with an energy of 4.7 mJ [71], the InnoSlab laser generating 54 mJ pulse energy at 10 kHz repetition rate [63], and a 5 kHz repetition rate thin-disk laser demonstrated to generate picosecond pulses with 200 mJ energy [60]. In 2016,

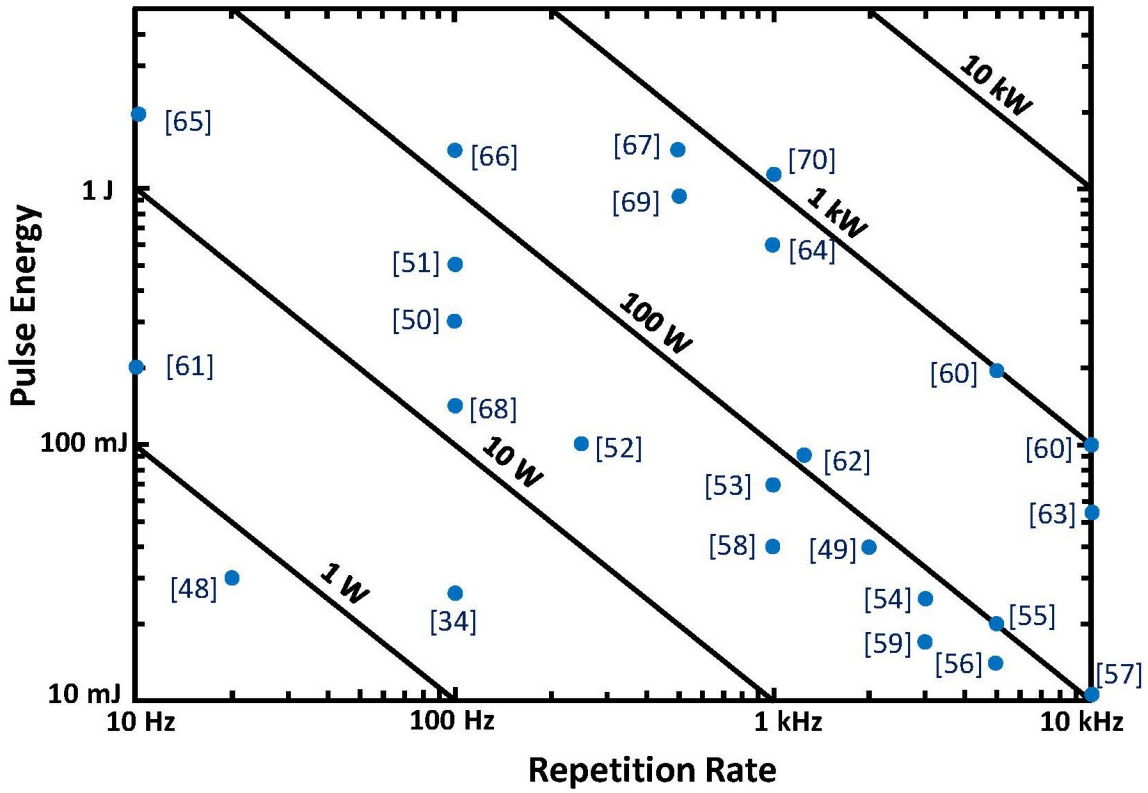

Figure 1.10: Summary of the state-of-the-art diode-pumped Yb-doped lasers at $\lambda = 1\,\mu m$ with high pulse energy (>10 mJ) and repetition rate (>10 Hz). Each performance point is related to the corresponding number in the reference list [34, 48–70].

our group has previously demonstrated a cryogenically cooled Yb:YAG active mirror laser that produced 1 J pulses at 500 Hz, an average power of 500 W [67]. More recently, L.E.Zapata et al. reported a cryogenically cooled Yb:YAG amplifier that can generate 1 J pulses of 20 ns duration at 500 Hz repetition in 2019 [69]. A Yb:YAG laser system based on thin disks was reported to deliver pulses with 720 mJ energy at 1 kHz repetition rate by C. Herkommer et al. in 2020 [64]. At higher energy but lower repetition rate, an Yb:YAG laser has been demonstrated to generate 10 ns pulses of up to 100 J at 10 Hz repetition rate by the group in the Central Laser Facility (CLF) in 2018 [72].

1.4.3 Pump Laser of High Power High Energy Ultrafast Lasers

Second harmonic generation (SHG) based on the λ = 1 μm Yb-doped laser also provides a path for the development of high energy, high repetition rate pulse lasers that are critical for developing ultrafast lasers. The generation of high-energy green pulses with high average power by frequency-doubled λ = 1 μm lasers has been successfully demonstrated in recent years. The general selection of nonlinear optical material for the SHG process of λ = 1 μm pulses is mostly limited to LiB_3O_5 (LBO), β-BaB_2O_4 (BBO), yttrium calcium oxyborate (YCOB), and KH_2PO_4(KDP). Among all, LBO has proven to yield the highest optical conversion efficiency into the second harmonic for high energy λ = 1 μm lasers [73–77]. However, most of the reported progress achieved in the development of high average power green lasers based on Yb-doped material has been limited to the level of μJ to mJ pulses at repetition rates ranging from hundreds of kHz to megahertz (MHz), as shown in Table 1.4. For example, 370 W average power at λ = 515 nm was achieved by generating 7 μJ pulses at 50 MHz repetition rate [75]. An average power of 1.4 kW was achieved at the same wavelength with 4.8 mJ pulses at 300 kHz repetition rate [76]. In comparison, the repetition rate and average power of lasers generating joule-level green pulses have remained considerably low. SHG in the cryogenically cooled Yb:YAG laser has produced 5.6 J pulses at 10 Hz repetition rate, with an average power of 56 W [77]. Recently, the same group demonstrated an upgraded version of their system to reach a λ = 515 nm pulse energy of 59.7 J at 10 Hz repetition rate [78]. However, there are still no reports of joule-level green pulse laser operation at kHz repetition rates. Future

progress in the development of high pulse energy, high repetition rate green lasers will make it possible to construct a kHz level ultrafast laser system with hundreds of millijoule pulse energy using either multi-pass Ti:Sapphire amplifier or OPCPA system pumped at kHz level repetition rate.

Table 1.4: Summary of the state-of-the-art high power green laser based on based on Yb-doped λ = 1 µm lasers [71, 75–82].

Wavelength	Energy	Rep. Rate	Average Power	Pulse Duration	NLO material	References
515 nm	2.7 mJ	300 kHz	820 W	8 ps	LBO	*Jan-Philipp Negel, 2015 [71]*
515 nm	4.7 mJ	300 kHz	1.4 kW	6.8 ps	LBO	*Christoph Rocker, 2020 [76]*
520 nm	60 µJ	10 MHz	600 W	285 ps	LBO	*Koji Tsubakimoto, 2017 [79]*
520 nm	26.4 µJ	5 MHz	135 W	406 fs	LBO	*Jan Rothhardt, 2010 [80]*
515 nm	22 µJ	20 MHz	445 W	733 fs	LBO	*Bastian Gronloh, 2014 [75]*
523 nm	31.7 J	10 Hz	317 W	15 ns	YCOB	*MERCURY, 2008 [81]*
515 nm	5.6 J	10 Hz	56 W	10 ns	LBO	*DiPOLE100, 2016 [77]*
515 nm	59.7	10 Hz	597 W	10 ns	LBO	*DiPOLE100, 2020 [78]*

1.5 Main Content of the Dissertation

The work in this dissertation is motivated by the goal of developing a high repetition rate (500 Hz - 1 kHz level) ultrafast Ti:Sapphire laser with the pulse energy of a few hundred millijoules. The proposed laser scheme, diagrammatically illustrated in Figure 1.11, is based on a 1 kHz repetition rate cryogenically cooled diode-pumped Yb:YAG laser as the primary pump source to pump a sequence of two Ti:Sapphire amplifiers. The 1030 nm output beam from this laser can be frequency-doubled to 515 nm to pump the Ti:Sapphire amplifiers.

The work in this thesis consisted of developing key components for this laser system. Several key challenges were addressed towards achieving the goal. The first consisted in the upgrade of a 500 Hz joule-level Yb:YAG system previously developed at CSU [67] to 1 kHz repetition rate operation. Secondly, the output of this λ = 1030 nm laser had to be efficiently frequency doubled

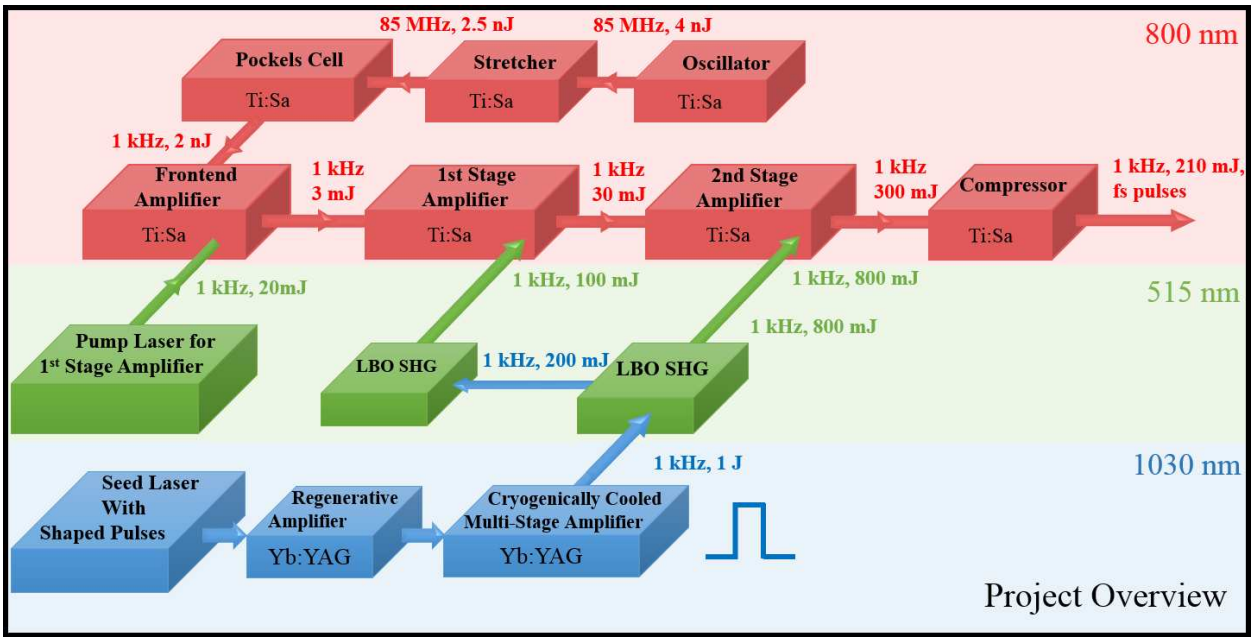

Figure 1.11: Schematic diagram of high repletion rate ultrafast Ti:Sapphire laser pumped by frequency doubled cryogenically cooled Yb:YAG amplifiers.

to kilowatt average power in green that is needed to pump the Ti:Sapphire amplifier stages. Lastly, the Ti:Sapphire amplifiers need to be designed to manage the thermal load. To separately address these key problems, the structure of this dissertation is divided into three main parts that will address the problem key, the corresponding methods, and results obtained.

In Chapter 2 and Chapter 3, a real-time three-dimensional (3-D) temperature mapping technique for cryogenically cooled Yb:YAG is introduced and applied to the previously developed 500 Hz joule-level Yb:YAG laser system. As mentioned above, thermal management in high-power laser systems is the fundamental solution to mitigate the thermal effects. Chapter 2 introduces the basic concept and the demonstration of this real-time three-dimensional (3-D) temperature measurement technique, which is based on fluorescence analysis by a neural network algorithm. In Chapter 3, the results of applying this technique to the final amplification stage of the kilowatt average power cryogenically cooled Yb:YAG amplifier will be discussed along with deformation simulations and measurements. By scanning the probe area of the entire laser material, the temperature distributions under different pump powers up to kilowatts were measured. In addition, interferometry measurement was conducted to measure the mechanical deformation of

the gain medium under different pump conditions. These investigations aided the scaling of the existing 500 Hz, >1 J amplifier [67] to 1 kHz repetition rate.

In Chapter 4, the 1 kHz operation of the Joule-level Yb:YAG system is described along with the generation of the kW level average power λ = 515 nm green pulses at 1 kHz repetition rate. In the first part, the modifications applied to the cryogenically cooled Yb:YAG laser system to achieve 1 kHz repetition rate operation are described, including the modifications in the regenerative amplifier, the pre-amplifier, and the main amplifier. In the second part of this chapter, the frequency-doubled generation of Joule-level 515 nm wavelength laser pulses at 1 kHz repetition rate is presented. The generation of temporal rectangular shape nanoseconds pulses with an arbitrary pulse shape seed laser, and the uses of two LBO crystals in sequence to maximize SHG is described, resulting in the generation of 1.04 kW average power λ = 515 nm beam at 1 kHz repetition rate.

Chapter 5 focuses on the design of room-temperature kHz-repetition-rate Ti:Sapphire amplifier system and the first results achieved with this design. The Ti:Sapphire CPA system was designed with a home-built front end laser and two subsequent multi-pass amplifiers pumped by the green laser demonstrated in Chapter 4 to produce more than 300 mJ at 1 kHz repetition rate before pulse compression. A new Ti:Sapphire crystal geometry named cross-thin slab (XTS) geometry was proposed to achieve good heat dissipation for high energy high repetition rates operation. This XTS geometry provides the large cooling area while maintaining energy extraction efficiency. The water cooled crystal mounts for each multi-pass amplifier were designed to achieve the efficient heat dissipation. The gain calculation and thermal distribution simulation results show that the 300 mJ pulse duration at 1 kHz repetition rate is feasible with this design. A pair of gold gratings was used for compressing the pulses from the front end laser passing through the entire system, which shows that less than 55 fs pulses can be achieved with the current design. Shorter than 30 fs pulses could be achieved with additional spectrum compensation device added to the system, which will result in 10 TW level peak power pulses.

Chapter 6 presents a summary of the dissertation, with a short discussion of the future plan.

References

[1] TH Maiman. Optical and microwave-optical experiments in ruby. *Physical Review Letters*, 4(11):564, 1960.

[2] Jeff Hecht. A short history of laser development. *Applied Optics*, 49(25):F99–F122, 2010.

[3] Ali Javan. Possibility of production of negative temperature in gas discharges. *Physical Review Letters*, 3(2):87, 1959.

[4] Robert N Hall, Gunther E Fenner, JD Kingsley, TJ Soltys, and RO Carlson. Coherent light emission from gaas junctions. *Physical Review Letters*, 9(9):366, 1962.

[5] Joan Lisa Bromberg. *The laser in America, 1950-1970*. MIT Press, 1991.

[6] CKN Patel, PK Tien, and JH McFee. CW high power CO2–N2–He laser. *Applied Physics Letters*, 7(11):290–292, 1965.

[7] Peter P Sorokin and JR Lankard. Stimulated emission observed from an organic dye, chloro-aluminum phthalocyanine. *IBM Journal of Research and Development*, 10(2):162–163, 1966.

[8] E. P. Ippen, C. V. Shank, and A Dienes. Passive mode locking of the CW dye laser. *Applied Physics Letters*, 21(8):348–350, 1972.

[9] Donna Strickland and Gerard Mourou. Compression of amplified chirped optical pulses. *Optics Communications*, 55(6):447–449, 1985.

[10] Colin N Danson, Constantin Haefner, Jake Bromage, Thomas Butcher, Jean-Christophe F Chanteloup, Enam A Chowdhury, Almantas Galvanauskas, Leonida A Gizzi, Joachim Hein, David I Hillier, et al. Petawatt and exawatt class lasers worldwide. *High Power Laser Science and Engineering*, 7, 2019.

[11] Engineering National Academies of Sciences, Medicine, et al. *Opportunities in Intense Ultrafast Lasers: Reaching for the Brightest Light*. National Academies Press, 2018.

[12] A Stingl, M Lenzner, Ch Spielmann, F Krausz, and R Szipöcs. Sub-10-fs mirror-dispersion-controlled Ti:sapphire laser. *Optics Letters*, 20(6):602–604, 1995.

[13] Richard Ell, Uwe Morgner, Franz X Kärtner, James G Fujimoto, Erich P Ippen, V Scheuer, Gregor Angelow, Theo Tschudi, Max J Lederer, Alex Boiko, et al. Generation of 5-fs pulses and octave-spanning spectra directly from a Ti:sapphire laser. *Optics Letters*, 26(6):373–375, 2001.

[14] Edmond Treacy. Optical pulse compression with diffraction gratings. *IEEE Journal of Quantum Electronics*, 5(9):454–458, 1969.

[15] O Martinez. 3000 times grating compressor with positive group velocity dispersion: Application to fiber compensation in 1.3-1.6 μm region. *IEEE Journal of Quantum Electronics*, 23(1):59–64, 1987.

[16] G Ravindra Kumar. The 2018 nobel prize in physics: a gripping and extremely exciting tale of light. *Current Science*, 115(10):1844–1848, 2018.

[17] Yong Wang, Shoujun Wang, Alex Rockwood, Bradley M Luther, Reed Hollinger, Alden Curtis, Chase Calvi, Carmen S Menoni, and Jorge J Rocca. 0.85 pw laser operation at 3.3 hz and high-contrast ultrahigh-intensity λ= 400 nm second-harmonic beamline. *Optics letters*, 42(19):3828–3831, 2017.

[18] ELI Beamlines. https://www.eli-beams.eu/facility/lasers/laser-3-hapls-1-pw-30-j-10-hz/.

[19] R Clady, Y Azamoum, L Charmasson, A Ferré, O Utéza, and M Sentis. 22 W average power multi-terawatt femtosecond laser chain enabling 10^{19} W/cm^2 at 100 Hz. *Applied Physics B*, 124(5):1–9, 2018.

[20] Rimantas Budriūnas, Tomas Stanislauskas, Jonas Adamonis, Aidas Aleknavičius, Gediminas Veitas, Darius Gadonas, Stanislovas Balickas, Andrejus Michailovas, and Arūnas Varanavičius. 53 W average power CEP-stabilized OPCPA system delivering 5.5 TW few cycle pulses at 1 kHz repetition rate. *Optics Express*, 25(5):5797–5806, 2017.

[21] Tomas Stanislauskas, Ignas Balčiūnas, Rimantas Budriūnas, Gediminas Veitas, Darius Gadonas, Jonas Adamonis, Andrejus Michailovas, Ádám Börzsönyi, Szabolcs Tóth, Janos Csontos, et al. Chirped pulse parametric amplifier producing 5-TW, 2.1-cycle, CEP-stable pulses at 1 kHz repetition rate. In *2019 Conference on Lasers and Electro-Optics Europe & European Quantum Electronics Conference (CLEO/Europe-EQEC)*, pages 1–1. IEEE, 2019.

[22] Y Nabekawa, A Amani Eilanlou, Y Furukawa, KL Ishikawa, H Takahashi, and K Midorikawa. Multi-terawatt laser system generating 12-fs pulses at 100 Hz repetition rate. *Applied Physics B*, 101(3):523–534, 2010.

[23] A Golinelli, X Chen, B Bussière, E Gontier, P-M Paul, O Tcherbakoff, P D'oliveira, and J-F Hergott. CEP-stabilized, sub-18 fs, 10 kHz and TW-class 1 kHz dual output Ti:Sa laser with wavelength tunability option. *Optics Express*, 27(10):13624–13636, 2019.

[24] Tiago de Faria Pinto, Jan Mathijssen, Kjeld SE Eikema, and Stefan Witte. Optical parametric chirped pulse amplifier producing ultrashort 10.5 mj pulses at 1.55 μm. *Optics Express*, 27(21):29829–29837, 2019.

[25] Roman Antipenkov, František Batysta, Robert Boge, Emily Erdman, Michael Greco, Jonathan T Green, Bedřich Himmel, Martin Horáček, Zbyněk Hubka, Lukáš Indra, et al. The construction of Allegra kilohertz femtosecond laser system at ELI-Beamlines. In *Short-pulse High-energy Lasers and Ultrafast Optical Technologies*, volume 11034, page 110340M. International Society for Optics and Photonics, 2019.

[26] Peter F Moulton. Spectroscopic and laser characteristics of Ti:Al_2O_3. *JOSA B*, 3(1):125–133, 1986.

[27] MG Holland. Thermal conductivity of several optical maser materials. *Journal of Applied Physics*, 33(9):2910–2911, 1962.

[28] Evgeni Sorokin. Solid-state materials for few-cycle pulse generation and amplification. *Few-cycle laser pulse generation and its applications*, pages 3–73, 2004.

[29] Sujith Manjooran and Arkady Major. Diode-pumped 45 fs Yb:CALGO laser oscillator with 1.7 MW of peak power. *Optics Letters*, 43(10):2324–2327, 2018.

[30] Yiran Wang, Xiancui Su, Yiyan Xie, Feilong Gao, Santosh Kumar, Qinglin Wang, Cailong Liu, Bingyuan Zhang, Baitao Zhang, and Jingliang He. 17.8 fs broadband Kerr-lens mode-locked Yb:CALGO oscillator. *Optics Letters*, 46(8):1892–1895, 2021.

[31] Anne-Laure Calendron. Dual-crystal Yb:CALGO high power laser and regenerative amplifier. *Optics Express*, 21(22):26174–26181, 2013.

[32] Huijun He, Jun Yu, Wentao Zhu, Xiaoyang Guo, Cangtao Zhou, and Shuangchen Ruan. A Yb:KGW dual-crystal regenerative amplifier. *High Power Laser Science and Engineering*, 8, 2020.

[33] Anne-Laure Calendron, Hüseyin Çankaya, and Franz X Kärtner. High-energy kHz Yb:KYW dual-crystal regenerative amplifier. *Optics Express*, 22(20):24752–24762, 2014.

[34] Dimitrios N Papadopoulos, Alain Pellegrina, Lourdes Patricia Ramirez, Patrick Georges, and Frédéric Druon. Broadband high-energy diode-pumped Yb:KYW multipass amplifier. *Optics Letters*, 36(19):3816–3818, 2011.

[35] Joerg Neukum. Overview on new diode lasers for defense applications. In *High-Power Lasers 2012: Technology and Systems*, volume 8547, page 85470X. International Society for Optics and Photonics, 2012.

[36] Kireet Semwal and SC Bhatt. Study of Nd^{3+} ion as a dopant in yag and glass laser. *International Journal of Physics*, 1(1):15–21, 2013.

[37] InnoLas Laser. https://www.innolas-laser.com.

[38] Northrop Grumman. http://catalog.cuttingedgeoptronics.com/.

[39] Photonics Industries. https://www.photonix.com/.

[40] Sébastien Chénais, Frédéric Druon, Sébastien Forget, François Balembois, and Patrick Georges. On thermal effects in solid-state lasers: The case of ytterbium-doped materials. *Progress in Quantum Electronics*, 30(4):89–153, 2006.

[41] RL Aggarwal, DJ Ripin, JR Ochoa, and TY Fan. Measurement of thermo-optic properties of $Y_3Al_5O_{12}$, $Lu_3Al_5O_{12}$, $YAlO_3$, $LiYF_4$, $LiLuF_4$, BaY_2F_8, $KGd(WO_4)_2$, and $KY(WO_4)_2$ laser crystals in the 80–300 K temperature range. *Journal of Applied Physics*, 98(10):103514, 2005.

[42] M. Siebold, S. Bock, U. Schramm, B. Xu, Jean-Louis Doualan, Patrice Camy, and Richard Moncorgé. Yb:CaF_2—a new old laser crystal. *Applied Physics B*, 97(2):327–338, 2009.

[43] N.V. Kuleshov, A.A. Lagatsky, A.V. Podlipensky, V.P. Mikhailov, and G. Huber. Pulsed laser operation of Yb-doped $KY(WO_4)_2$ and $KGd(WO_4)_2$. *Optics Letters*, 22(17):1317–1319, 1997.

[44] Walter Koechner and Michael Bass. *Solid-state lasers: a graduate text*. Springer Science & Business Media, 2006.

[45] Rosalind Wynne, John L Daneu, and Tso Yee Fan. Thermal coefficients of the expansion and refractive index in YAG. *Applied Optics*, 38(15):3282–3284, 1999.

[46] Jun Dong, Michael Bass, Yanli Mao, Peizhen Deng, and Fuxi Gan. Dependence of the Yb^{3+} emission cross section and lifetime on temperature and concentration in yttrium aluminum garnet. *JOSA B*, 20(9):1975–1979, 2003.

[47] Glen A Slack and DW Oliver. Thermal conductivity of garnets and phonon scattering by rare-earth ions. *Physical Review B*, 4(2):592, 1971.

[48] Junji Kawanaka, Koichi Yamakawa, Hajime Nishioka, and Ken-ichi Ueda. 30-mj, diode-pumped, chirped-pulse Yb:YLF regenerative amplifier. *Optics Letters*, 28(21):2121–2123, 2003.

[49] Kyung-Han Hong, Juliet T Gopinath, Darren Rand, Aleem M Siddiqui, Shu-Wei Huang, Enbang Li, Benjamin J Eggleton, John D Hybl, Tso Yee Fan, and Franz X Kärtner. High-

energy, kHz-repetition-rate, ps cryogenic Yb:YAG chirped-pulse amplifier. *Optics Letters*, 35(11):1752–1754, 2010.

[50] J Tümmler, R Jung, H Stiel, PV Nickles, and W Sandner. High-repetition-rate chirped-pulse-amplification thin-disk laser system with joule-level pulse energy. *Optics Letters*, 34(9):1378–1380, 2009.

[51] Robert Jung, Johannes Tümmler, Thomas Nubbemeyer, and Ingo Will. Thin-disk ring amplifier for high pulse energy. *Optics express*, 24(5):4375–4381, 2016.

[52] Luis E Zapata, Hua Lin, Anne-Laure Calendron, Huseyin Cankaya, Michael Hemmer, Fabian Reichert, W Ronny Huang, Eduardo Granados, Kyung-Han Hong, and Franz X Kärtner. Cryogenic Yb:YAG composite-thin-disk for high energy and average power amplifiers. *Optics Letters*, 40(11):2610–2613, 2015.

[53] Chun-Lin Chang, Peter Krogen, Kyung-Han Hong, Luis E Zapata, Jeffrey Moses, Anne-Laure Calendron, Houkun Liang, Chien-Jen Lai, Gregory J Stein, Phillip D Keathley, et al. High-energy, kHz, picosecond hybrid Yb-doped chirped-pulse amplifier. *Optics Express*, 23(8):10132–10144, 2015.

[54] Thomas Metzger, Alexander Schwarz, Catherine Yuriko Teisset, Dirk Sutter, Alexander Killi, Reinhard Kienberger, and Ferenc Krausz. High-repetition-rate picosecond pump laser based on a Yb:YAG disk amplifier for optical parametric amplification. *Optics Letters*, 34(14):2123–2125, 2009.

[55] Hanieh Fattahi, Ayman Alismail, Haochuan Wang, Jonathan Brons, Oleg Pronin, Theresa Buberl, Lénárd Vámos, Gunnar Arisholm, Abdallah M Azzeer, and Ferenc Krausz. High-power, 1-ps, all-Yb:YAG thin-disk regenerative amplifier. *Optics Letters*, 41(6):1126–1129, 2016.

[56] Darren A Rand, Scot EJ Shaw, Juan R Ochoa, Daniel J Ripin, Andrew Taylor, Tso Yee Fan, Hector Martin, Scott Hawes, Jim Zhang, Samvel Sarkisyan, et al. Picosecond pulses from

a cryogenically cooled, composite amplifier using Yb:YAG and Yb:GSAG. *Optics Letters*, 36(3):340–342, 2011.

[57] Daniel E Miller, Luis E Zapata, Daniel J Ripin, and Tso Yee Fan. Sub-picosecond pulses at 100 W average power from a Yb:YLF chirped-pulse amplification system. *Optics Letters*, 37(13):2700–2702, 2012.

[58] Jakub Novák, Jonathan T Green, Thomas Metzger, Tomáš Mazanec, Bedřich Himmel, Martin Horáček, Zbyněk Hubka, Robert Boge, Roman Antipenkov, František Batysta, et al. Thin disk amplifier-based 40 mj, 1 kHz, picosecond laser at 515 nm. *Optics Express*, 24(6):5728–5733, 2016.

[59] Jonathan Fischer, Alexander-Cornelius Heinrich, Simon Maier, Julian Jungwirth, Daniele Brida, and Alfred Leitenstorfer. 615 fs pulses with 17 mJ energy generated by an Yb: thin-disk amplifier at 3 kHz repetition rate. *Optics Letters*, 41(2):246–249, 2016.

[60] Thomas Nubbemeyer, Martin Kaumanns, Moritz Ueffing, Martin Gorjan, Ayman Alismail, Hanieh Fattahi, Jonathan Brons, Oleg Pronin, Helena G Barros, Zsuzsanna Major, et al. 1 kW, 200 mJ picosecond thin-disk laser system. *Optics Letters*, 42(7):1381–1384, 2017.

[61] Sandro Klingebiel, Christoph Wandt, Christoph Skrobol, Izhar Ahmad, Sergei A Trushin, Zsuzsanna Major, Ferenc Krausz, and Stefan Karsch. High energy picosecond Yb:YAG CPA system at 10 Hz repetition rate for pumping optical parametric amplifiers. *Optics Express*, 19(6):5357–5363, 2011.

[62] FX Morrissey, TY Fan, DE Miller, and D Rand. Picosecond kilohertz-class cryogenically cooled multistage Yb-doped chirped pulse amplifier. *Optics Letters*, 42(4):707–710, 2017.

[63] Bruno E Schmidt, Arvid Hage, Torsten Mans, François Légaré, and Hans Jakob Wörner. Highly stable, 54 mJ Yb-InnoSlab laser platform at 0.5 kW average power. *Optics Express*, 25(15):17549–17555, 2017.

[64] Clemens Herkommer, Peter Krötz, Robert Jung, Sandro Klingebiel, Christoph Wandt, Robert Bessing, Pierre Walch, Thomas Produit, Knut Michel, Dominik Bauer, et al. Ultrafast thin-disk multipass amplifier with 720 mJ operating at kilohertz repetition rate for applications in atmospheric research. *Optics Express*, 28(20):30164–30173, 2020.

[65] Federico J Furch, Brendan A Reagan, Bradley M Luther, Alden H Curtis, Shaun P Meehan, and Jorge J Rocca. Demonstration of an all-diode-pumped soft x-ray laser. *Optics letters*, 34(21):3352–3354, 2009.

[66] Brendan A Reagan, Cory Bamgarten, Keith Wernsing, Herman Bravo, Mark Woolston, Alden Curtis, Federico J Furch, Bradley M Luther, Dinesh Patel, Carmen S Menoni, et al. 1 Joule, 100 Hz repetition rate, picosecond CPA laser for driving high average power soft X-ray lasers. In *CLEO: Science and Innovations*, pages SM1F–4. Optical Society of America, 2014.

[67] Cory Baumgarten, Michael Pedicone, Herman Bravo, Hanchen Wang, Liang Yin, Carmen S Menoni, Jorge J Rocca, and Brendan A Reagan. 1 J, 0.5 kHz repetition rate picosecond laser. *Optics Letters*, 41(14):3339–3342, 2016.

[68] AH Curtis, BA Reagan, KA Wernsing, FJ Furch, BM Luther, and JJ Rocca. Demonstration of a compact 100 Hz, 0.1 J, diode-pumped picosecond laser. *Optics Letters*, 36(11):2164–2166, 2011.

[69] Luis E Zapata, Simon Schweisthal, Jelto Thesinga, Collette Zapata, Matthias Schust, Liu Yizhou, Mikhail Pergament, and Franz X Kaertner. Joule-class 500 Hz cryogenic Yb:YAG chirped pulse amplifier. In *CLEO: Science and Innovations*, pages SM4E–1. Optical Society of America, 2019.

[70] Yong Wang, Han Chi, Cory Baumgarten, Kristian Dehne, Alexander R Meadows, Aaron Davenport, Gabe Murray, Brendan A Reagan, Carmen S Menoni, and Jorge J Rocca. 1.1 J Yb:YAG picosecond laser at 1 kHz repetition rate. *Optics Letters*, 45(24):6615–6618, 2020.

[71] Jan-Philipp Negel, André Loescher, Andreas Voss, Dominik Bauer, Dirk Sutter, Alexander Killi, Marwan Abdou Ahmed, and Thomas Graf. Ultrafast thin-disk multipass laser amplifier delivering 1.4 kW (4.7 mJ, 1030 nm) average power converted to 820 W at 515 nm and 234 W at 343 nm. *Optics Express*, 23(16):21064–21077, 2015.

[72] Paul Mason, Saumyabrata Banerjee, Jodie Smith, Thomas Butcher, Jonathan Phillips, Hauke Höppner, Dominik Möller, Klaus Ertel, Mariastefania De Vido, Ian Hollingham, et al. Development of a 100 J, 10 Hz laser for compression experiments at the High Energy Density instrument at the European XFEL. *High Power Laser Science and Engineering*, 6, 2018.

[73] Chuangtian Chen, Yicheng Wu, Aidong Jiang, Bochang Wu, Guiming You, Rukang Li, and Shujie Lin. New nonlinear-optical crystal: LiB_3O_5. *JOSA B*, 6(4):616–621, 1989.

[74] T Ukachi, RJ Lane, WR Bosenberg, and CL Tang. Measurements of noncritically phase-matched second-harmonic generation in a LiB_3O_5 crystal. *Applied Physics Letters*, 57(10):980–982, 1990.

[75] Bastian Gronloh, Peter Russbueldt, Waldemar Schneider, Bernd Jungbluth, and Hans-Dieter Hoffmann. High average power sub-picosecond pulse generation at 515 nm by extracavity frequency doubling of a mode-locked Innoslab MOPA. In *Solid State Lasers Xxi: Technology and Devices*, volume 8235, page 82351C. International Society for Optics and Photonics, 2012.

[76] Christoph Röcker, André Loescher, Florian Bienert, Philippe Villeval, Dominique Lupinski, Dominik Bauer, Alexander Killi, Thomas Graf, and Marwan Abdou Ahmed. Ultrafast green thin-disk laser exceeding 1.4 kW of average power. *Optics Letters*, 45(19):5522–5525, 2020.

[77] Jonathan P Phillips, Saumyabrata Banerjee, Jodie Smith, Mike Fitton, Tristan Davenne, Klaus Ertel, Paul Mason, Thomas Butcher, Mariastefania De Vido, Justin Greenhalgh, et al. High energy, high repetition rate, second harmonic generation in large aperture DKDP, YCOB, and LBO crystals. *Optics Express*, 24(17):19682–19694, 2016.

[78] Jonathan P Phillips, Saumyabrata Banerjee, Paul Mason, Jodie Smith, Jacob Spear, Mariastefania De Vido, Klaus Ertel, Thomas Butcher, Gary Quinn, Danielle Clarke, et al. Second and third harmonic conversion of a kilowatt average power, 100-J-level diode pumped Yb:YAG laser in large aperture LBO. *Optics Letters*, 46(8):1808–1811, 2021.

[79] Koji Tsubakimoto, Hidetsugu Yoshida, and Noriaki Miyanaga. 600 W green and 300 W UV light generated from an eight-beam, sub-nanosecond fiber laser system. *Optics Letters*, 42(17):3255–3258, 2017.

[80] Jan Rothhardt, Tino Eidam, Steffen Hädrich, Florian Jansen, Fabian Stutzki, Thomas Gottschall, Thomas V Andersen, Jens Limpert, and Andreas Tünnermann. 135 W average-power femtosecond pulses at 520 nm from a frequency-doubled fiber laser system. *Optics Letters*, 36(3):316–318, 2011.

[81] A Bayramian. HEC DPSSL Development for LIFE Lifetest Facility. In *5th High Energy Class Diode Pumped Solid State Laser (HEC-DPSSL) Workshop*, June 10–12, 2009.

[82] François Légaré. *Emerging Laser Technologies for High-Power and Ultrafast Science*. 2053-2563. IOP Publishing, 2021.

Chapter 2

In situ 3-D Temperature Mapping of High Energy, High Average Power Cryogenic Amplifiers

Progress in a variety of important laser applications including compact particle accelerators [1], coherent and incoherent sources of ultra-short wavelength radiation [2–5], laser processing of materials [6], extreme ultraviolet lithography [7], and the future prospect of practical inertial confinement fusion power generation [8], generates a demand for lasers with simultaneously high pulse energy and high average power. Despite significant progress in high average power pulsed solid-state laser technology [9–14], the development of high energy, multi-kW average power lasers has been elusive. Recently, the first demonstrations of lasers producing >1 Joule pulses with kilowatt-level average power have been realized by taking advantage of the improved thermal parameters [15, 16] and the gain characteristics [17–19] of diode-pumped Yb:YAG at cryogenic temperature. These include the recent demonstration of a chirped pulse amplification (CPA) laser based on cryogenic Yb:YAG active mirror amplifiers that produced 1.5 J stretched pulses at 0.5 kHz repetition rate (0.75 kW average power) which were subsequently compressed to about 5 ps duration [20], and the generation of 100 J pulses at 10 Hz repetition rate with nanosecond pulse duration using cryogenic gas-cooled Yb:YAG amplifiers [21].

As discussed in Chapter 1, one of the key challenges in the development of higher average power laser amplifiers is the thermal management of the gain medium. A solution is to use cryogenic cooling. As a result, developing a temperature technique that can noninvasively measure the temperature of the laser material in real time during full power operation is important. However, current temperature measurement tools such as the thermal camera cannot be used at cryogenic temperature. A new technique capable of mapping the Yb-doped material at cryogenic temperature needs to be developed.

This chapter presents the demonstration of a three-dimensional (3-D) temperature measurement technique for Yb:YAG laser system at the cryogenic temperature. The method can provide a 3-D map of the temperature of the laser amplifier gain medium as it is operating at full power (kilowatt-level average power) in real-time and noninvasively. The temperature is determined by analyzing the amplifier's fluorescence spectra with a neural network algorithm. The accuracy of the technique relies on a calibration that does not depend on simulations. Results are presented for a cryogenic Yb:YAG active mirror laser amplifier operating at different pump conditions. The technique is also applicable to other solid-state laser materials.

2.1 Introduction

Heat generation in solid-state laser amplifiers is a key obstacle to scaling high-energy solid-state lasers to higher average power. Thermal gradients within the amplifier active material lead to the power-limiting effects of thermal lensing, depolarization, and, ultimately, catastrophic stress fracture of the material. The ability to make spatially resolved measurements of the temperature within the cryogenically cooled gain material is very useful for understanding heat generation and distribution processes, and benchmarking simulations of heat flow to aid in the design of optimized geometries and superior cooling techniques. To our knowledge, no two-dimensional (2-D) or 3-D technique has been developed to measure the temperature of laser materials at cryogenic temperature during operation. A few methods for determining the temperature of solid-state laser materials have been previously demonstrated. Wavefront and depolarization measurements have been made to determine thermal effects present in solid-state lasers [22, 23]. However, these methods do not directly measure the temperature and require assumptions to be made about the thermo-optic coefficient and expansion coefficient of the material, as well as being sensitive to a number of parameters. More direct methods to determine the operating temperature of laser gain media have been demonstrated for lasers operating near room temperature, including using the luminescence (fluorescence) of the dopant ion [24–26] and the use of infrared thermal camera to acquire thermal maps [27]. However, thermal cameras cannot be used at cryogenic temperature or

through most window materials. The luminescence of transition metals and rare earth elements, including Yb^{3+} [28], has been extensively studied for the development of temperature sensors for a broad range of applications, as discussed in several review papers [29–31]. Most of these studies focused on temperatures near or above room temperature, but some include work on thermographic phosphors in a cryogenic environment. The latter include the use of the luminescence from Mg_4FGeO_6:Mn, a laser-induce fluorescence phosphor, for 2-D temperature measurements in the 110-300 K range [32].

A technique to determine the temperature of a cryogenic Yb:YAG laser was reported that uses the intensity ratio of two points in the Yb:YAG fluorescence spectrum [33]. This method was demonstrated in a continuous wave (CW) diode-pumped laser. However, as discussed below, we have observed that this intensity ratio is insufficient to accurately determine the temperature of a pulsed Yb:YAG cryo-cooled amplifier with strong gain where stimulated emission significantly alters the fluorescence spectrum. In this Chapter, we present a technique that overcomes the limitations of this optical technique using the entire information in a selected range of the fluorescence spectrum to accurately measure the temperature of Yb-doped gain media operating at cryogenic temperature. We also show that this technique can be employed to generate 2-D and 3-D maps of the temperature distribution in cryo-cooled laser amplifiers based on spatially resolved measurements of the emission fluorescence. This technique can be implemented in situ, under high power laser operating conditions. We demonstrate the utility of this new technique by recording thermal maps of a cryo-cooled Yb:YAG active mirror amplifier under different pumping intensities and heat removal conditions. While an active mirror Yb:YAG amplifier was used for the measurements presented here, the technique is general and can be used on other cryogenic Yb:YAG oscillator or amplifier geometries and is expected to be useful on other solid-state laser materials as well.

2.2 Laser Amplifier Thermal Measurements at Cryogenic Temperatures

The fluorescence spectrum emitted by Yb:YAG is dependent on temperature. Figure 2.1 shows emission spectra from a 2 mm thick 3-at.% Yb:YAG crystal at different temperatures between 40 K and 280 K. The temperature was varied with the aid of a closed-cycle He cryorefrigerator. The temperature was determined with a silicon diode attached to the heat spreading plate to which the crystal is soldered. To ensure that this temperature is the same as that of the crystal, individual pump pulses were used to obtain the spectra, eliminating any local heating that could create a temperature difference with respect to the heat sink where the temperature sensor is located. As can be seen from these spectra for the 1015 nm-1029 nm wavelength region, as the temperature of the crystal is increased, the peaks at 1022 nm and 1025 nm decrease in amplitude, broaden, and shift to longer wavelength. In Ref. [33], the ratio of the fluorescence intensities at 1022 nm and 1027 nm was used to estimate the local temperature of the active region. However, as can be seen from the normalized spectra in Figure 2.1(b) and Figure 2.1(c), in this high gain medium the spectra are also dependent on the pump power. This indicates that it is affected by stimulated emission. The effect is more clearly demonstrated in the plot of Figure 2.1(d), which shows this intensity ratio as a function of the crystal temperature for pump pulses of three different energies. These measurements show that the intensity ratio method is influenced by gain effects, leading to discrepancies between the inferred temperature and the measured temperature by as large as 20 K in the temperature range from 60 K to 140 K. Therefore, the method previously reported cannot be used to accurately measure temperature profiles in high gain cryogenically cooled amplifiers.

In the following sections, we describe a variation of the fluorescence measurement approach that allows for accurate measurements in the range of temperatures of interest for high power cryo-cooled amplifiers with a resolution of less than 1 K. Instead of using the ratio of the fluorescence intensity at two wavelengths, we make use of the entire fluorescence spectrum in a selected wavelength region as input for a neural network based fitting function [34–36].

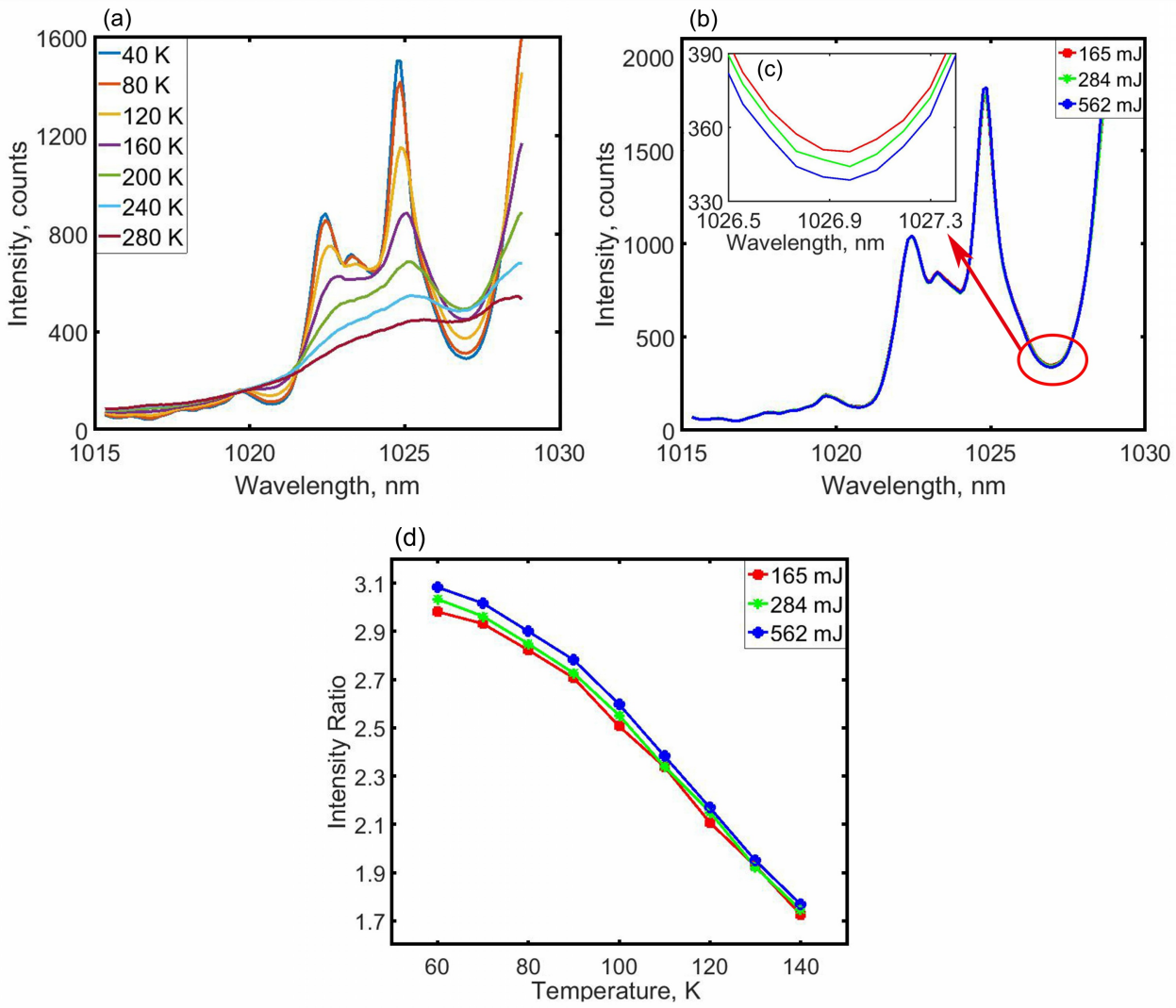

Figure 2.1: (a) Measured Yb:YAG fluorescence spectra from 1015 nm to 1029 nm at different temperatures. (b) Fluorescence spectra at 60 K excited with different pump energies (single shot), normalized at 1022 nm. (c) The enlarged fluorescence spectra near 1027.0 nm. (d) The fitted temperature results only using 1022 nm/ 1027 nm intensity ratio from 60 K to 140 K at different pump energies.

2.3 Temperature Mapping Technique

The experimental setups used to measure the 2-D and 3-D temperature distribution in a cryogenically cooled Yb:YAG active mirror amplifier are shown in Figure 2.2(a) and Figure 2.3, respectively. The active mirror was soldered to a copper heat sink that operates in vacuum cooled by a closed-cycle He cryo-refrigerator. The temperature of the heat sink was monitored by a calibrated Si diode detector. A heater was used to tune the temperature of the gain material for calibration.

2-D Temperature Mapping Technique

Figure 2.2(a) shows the experimental setup for 2-D temperature mapping. To determine the temperature in the active area (gain region), it is sufficient to collect the fluorescence generated by the 940 nm pump laser. However, since it is also of interest to determine the temperature in the region surrounding the active area where there is no fluorescence, a λ = 940 nm fiber coupled laser diode module is used to produce a small diameter "localized probe pulse" that can be displaced to excite the fluorescence at any crystal location of interest. A localized probe pulse duration of 1.5 ms was used to generate fluorescence at a very low repetition rate (single shot) to avoid influencing the thermal profile. These localized probe pulses are delivered through a 600 µm core diameter probe fiber which is imaged onto the laser crystal using a single achromatic lens. The magnification of this image system is 5×. The probe fiber is mounted in close proximity to a second fiber that collects the fluorescence signal. This 50 µm core diameter, NA = 0.22 signal fiber delivers the fluorescence to a 0.66 m focal length Czerny-Turner spectrometer. The end face of the signal fiber is placed at the crystal's image plane. The tips of both fibers are mounted on an XYZ stage. The depth-of-field of the image system is about 6 mm and the transverse resolution was measured to be better than 0.5 mm. 2-D maps of the temperature in the active mirror Yb:YAG amplifier were obtained by raster scanning the tip of the probe and signal fibers through the plane of the fluorescence. A cooled scientific CMOS camera mounted on the spectrometer imaged the fluorescence spectra. The spectral window used for these measurements was 1015 nm-1029 nm with a resolution of about 0.03 nm. Note that this spectral region does not include the dominant emission

peak of Yb:YAG at $\lambda = 1030$ nm, but includes the bright emission occurring between 1020 nm and 1029 nm. The exposure time of the camera was selected to be 1 ms, and the acquisition time window was triggered at the beginning of the localized probe pulse. As shown below, this technique allows measurements of the transverse profile of the axial-averaged temperature distribution.

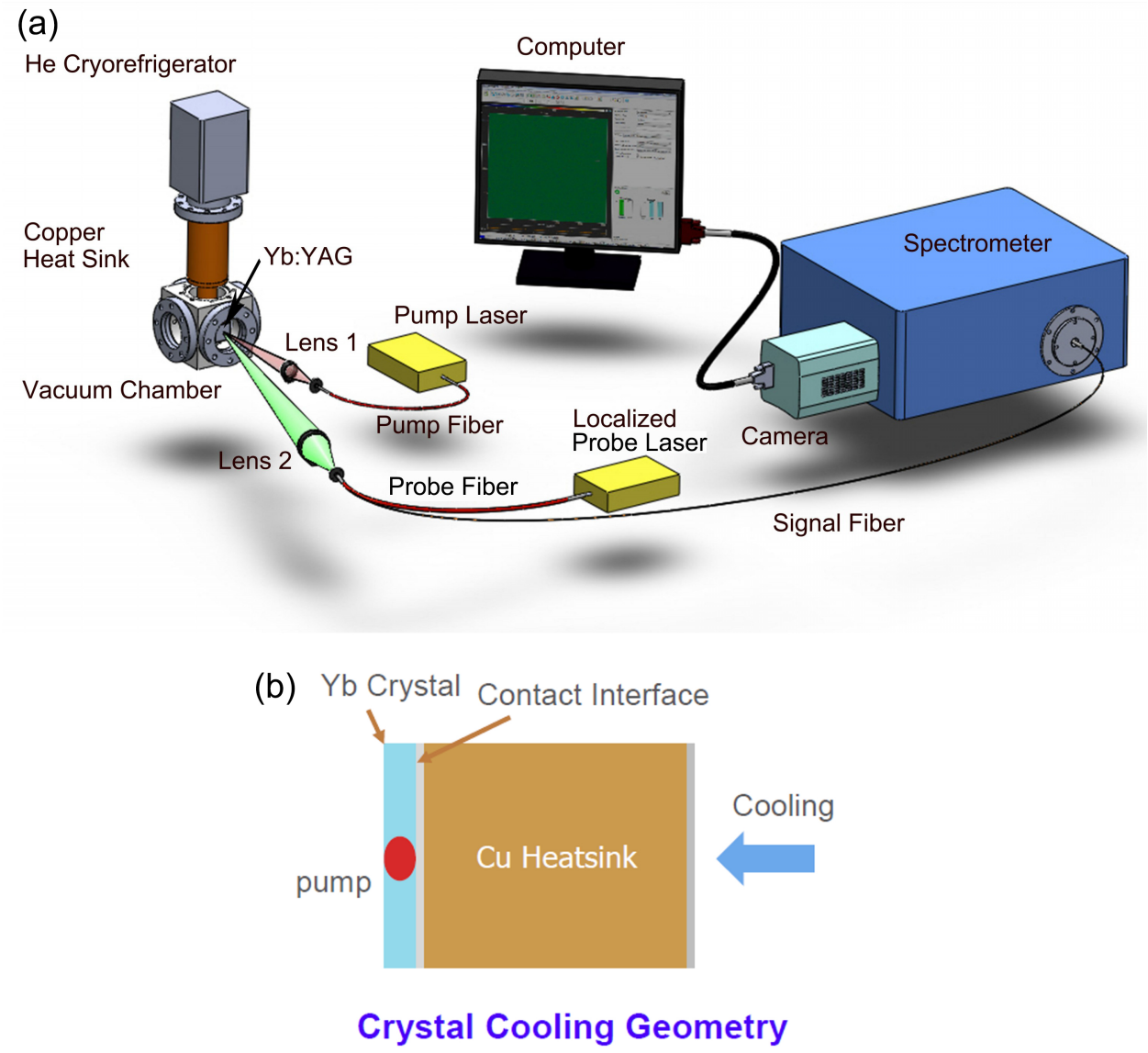

Figure 2.2: a) Conceptual diagram of the experimental setup for 2-D temperature mapping in solid-state laser amplifiers operating at cryogenic temperatures. b) Crystal cryo-cooling configuration.

For many cases, this 2-D temperature distribution is sufficient to understand thermal problems and is helpful to design efficient cooling techniques and monitor their performance. To obtain full, 3-D temperature distributions we constructed an alternative system based on the widely used confocal laser scanning microscopy (CLSM) technique [37], described below.

3-D Temperature Mapping Technique

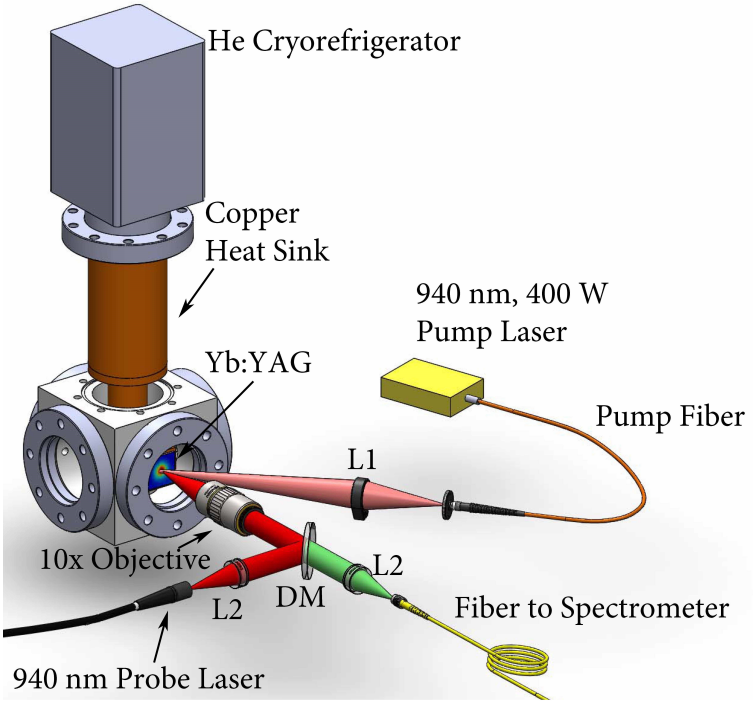

Figure 2.3: Conceptual diagram of the experimental setup for 3-D temperature mapping in solid-state laser amplifiers operating at cryogenic temperatures. L1 is an f = 25 mm achromatic lens, L2 is an f = 30 mm achromatic lens. DM is dichroic mirror.

To obtain full, 3-D temperature maps with depth resolution, we constructed the confocal microscope setup shown in Figure 2.3. In this setup, Lens 2, the pump fiber and the signal fiber in Figure 2.2(a) are replaced by the confocal setup, which consists of two f = 30 mm lenses (L2), a 1000 nm cut-off wavelength long-pass filter, and a long working distance 10× microscope objective. A single mode fiber and a single emitter laser used as the localized probe laser perform a similar function to the pinhole used in most CLSM. The localized probe laser is a 50 mW single

emitter 940 nm single mode laser diode that is collimated by lens L2. The collimated laser beam is reflected by the dichroic mirror and focused by the 10× objective into the crystal to trigger the fluorescence. The triggered fluorescence is collected by the 10× objective, passes thought the dichroic mirror and finally is focused by the second lens L2 into a 6 µm core diameter single mode fiber, which delivers it into the spectrometer. The confocal microscope achieves a depth resolution of about 100 µm defined by the distance over which the intensity of the fluorescence changes from 10% to 90% when the translation stage is scanned through the front surface of the crystal. The transverse resolution was measured to be better than 0.2 mm. An XYZ stage was employed to move the entire confocal setup to achieve the 3-D temperature measurements. The spectrometer signal was collected by the cooled scientific camera mounted in the image plane of the spectrometer, selecting an exposure time of 0.1 s. In the pumping area, the fluorescence resulting from the pump laser is subtracted so that only the fluorescence from the confocal setup is used in the analysis.

Neural Network Based Fitting Function

To achieve accurate local temperature measurements with high resolution over a broad range of pump powers and temperatures, the entire fluorescence spectrum from 1015 nm to 1029 nm was used as the input to a neural-network-based fitting function [34–36]. The neural network is a concept widely used in machine learning, which involves computers learning from provided data so that the computer can carry out certain tasks, for example, objects recognition, data mining, and outcomes prediction [38, 39]. The key ability of machine learning is to perform accurately on new, unseen data, examples, or tasks after having experienced a learning data set [40]. The training examples come from some generally unknown probability distributions (considered representative of the space of occurrences), and the learner (e.g., a computer/program) has to build a specific model (e.g., a neural network algorithm) about this space that enables it to produce sufficiently accurate predictions in new cases [41]. For the spectroscopy analysis at different temperatures, the variation in the spectra intensity at different wavelengths and the temperature value is linked through an unknown and complex relationship. If the computer/program was trained by a sufficient number of

spectra data at known temperatures, an algorithm would be generated to produce the accurate prediction of temperature with any unknown spectra data. The algorithm normally used for machine learning is the neural network fitting function, which is based on a collection of connected units or nodes called artificial neurons that loosely model the neurons in a biological brain [35, 36], as shown in Figure 2.4.

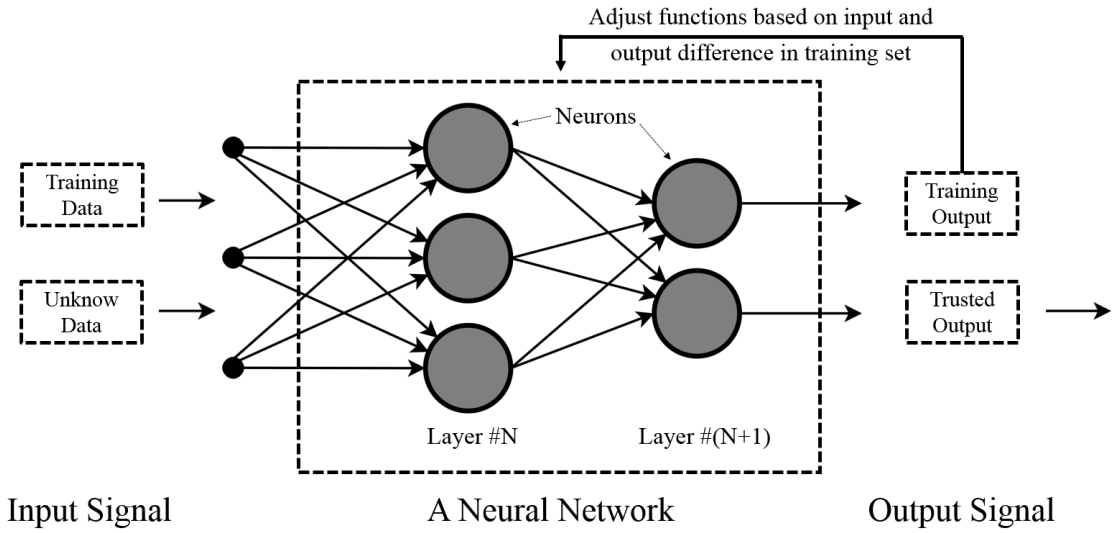

Figure 2.4: The concept of a neural network algorithm.

Each connection, or artificial neuron, can process the input signal and then transmit the signal to other neurons connected to it. The signal at each connection/neuron is a real number that is derived from the original data, and the output of each neuron is computed by a certain nonlinear function of the sum of its inputs. Typically, neurons are aggregated into layers. Each layer can generate different outputs based on their nonlinear functions, which are adjusted as learning proceeds. All these neurons, layers, and nonlinear functions combine as a neural network. For a general learning process from the initial neural network with a certain defined structure to an established neural network, the output of the neural network will be firstly compared with the original input training data. If the difference between the output and input is larger than a certain error range, an adjustment in the neural network will be initiated under a certain method toward the reduction of this difference. Then, the training data will be sent to the new neural network again to check

whether the new input-output difference is within the desired criterion. After a number of iterations of this process, the neural network will find out the best algorithm that fits the training data with the smallest error. In addition, depending on different design rules, some of the data will be used as the testing set and validation set which are not used in the training process to test the algorithm as the blind test sets. Once a certain neural network algorithm passes the desired criterion in the blind test, this neural network can be used to predict the output as the trusted result with a certain error range from the unknown data set as the input. This method has been widely used in variety of areas including spectroscopy analysis [42–44].

The neural network used here is based on the MATLAB Neural Network Toolbox [34]. The fitting function is a two-layer feed-forward neural network with sigmoid hidden neurons and linear output neurons. The network can fit arbitrary, multi-dimensional mapping problems well, given consistent data and enough neurons in its hidden layer [34]. To build the fitting algorithm, we recorded fluorescence spectra at known temperatures ranging from 50 K to 140 K with an interval of 5 K. At each temperature, spectra were recorded for 24 different localized probe pulse energies. In both the 2-D and 3-D measurements, the localized probe pulse is limited to very low energy and low average power which do not contribute to any significant heating of the material. The characteristics of the local pump pulses were kept the same during both the training of the neural network and the measurements presented below. These spectra recorded at known temperatures were used to train a 10-hidden-neuron fitting function [44]. For this purpose, the Yb:YAG crystal was mounted on the cold finger of closed-cycle He cryo-refrigerator using the geometry illustrated in Figure 2.2(b). The Levenberg-Marquardt back-propagation algorithm [44] was selected to train the network. 70% of the data was chosen randomly to train the network, 15% of the data was used as the validation sample, and the rest of the data was used for testing the performance of the network [34]. The acquisition and fitting of all the calibration spectra can be done in less than one hour. The temperature predicted by the fitting function closely matches the temperature measured by the sensor in the heat spreading plate when negligible power impinged on the crystal. Using a

test input of spectra recorded, but not used in the fitting algorithm, we obtained an RMS deviation of 0.24 K from the temperature measured by the temperature sensor.

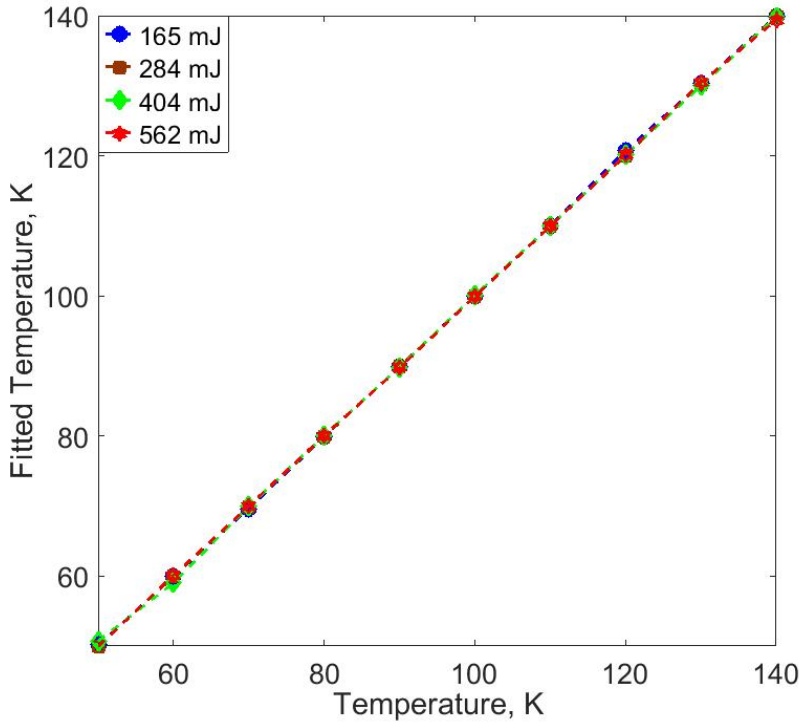

Figure 2.5: Results of the calibration of the fitting function with different pump energies resulting in temperature between 50 K and 140 K. The horizontal axis is the temperature measured by the semiconductor sensor in the heat sink and the vertical axis shows the temperature deduced by fitting the measured spectra. The overall RMS error is 0.24 K.

Figure 2.5 shows the results of this fitting function including all the training data, testing data and validation data. These measurements, obtained using a broad spread of pump energies and gain profiles, demonstrate the accuracy of this method for measuring the temperature of the Yb-doped laser media at cryogenic temperatures under varied pumping and energy extraction conditions.

2.4 Results and Discussion

Below we discuss the 2-D and 3-D temperature distributions obtained using this technique for different pumping intensities and heat removal conditions. The measurements presented here were

made on a cryogenic Yb:YAG active mirror multi-pass amplifier capable of producing 100 mJ-level pulses at 100 Hz repetition rate that is similar to that presented in Ref. [45]. The laser amplifier consists of a 2 mm thick, 3-at.% Yb:YAG active mirror pumped with up to 400 W peak power, 1.5 ms duration pump pulses in a 4 mm spot produced by a fiber-coupled laser diode module. Heat removal is accomplished using a closed-cycle He cryo-refrigerator.

2-D Temperature Maps

Figure 2.6 shows two different measured temperature maps corresponding to two different pump powers. These temperature maps were acquired by raster scanning the probe and the signal fibers over an area of 12 mm$\times$15 mm on the plane of the Yb:YAG active mirror with a step size 0.5 mm at a rate of about 1 pixel per second. The pulse from the localized probe laser was delayed with respect to the main pump pulse by 2 ms to avoid a temporal overlap of the fluorescence signals. The peak temperatures measured for the 113 W and 141 W pump power cases are 113 K and 138 K, respectively. The minimum-recorded temperatures outside the pump region are 95 K and 116 K, respectively. It should be noticed that as the fluorescence is collected from the entire thickness of the active mirror, the temperatures correspond to average values along the locally irradiated volume. These values, averaged along the crystal length, are useful for estimating thermal focusing and can be directly compared with simulations. As can be seen from these maps, the temperature profiles are convex and symmetric, as expected for the cooling geometry used in this experiment.

Figure 2.7 shows one-dimensional cuts of the temperature profiles corresponding to different average pump powers. The pump pulse energy and duration are kept constant, while the repetition rate was adjusted from 100 Hz to 250 Hz. It can be seen that, as the pump power is increased, the temperature difference between the axial and periphery of the pump spot increases due to a larger radial-cooling component. The increase in the "base" temperature apparent in these plots is mostly due to the increase of the heat sink temperature as the thermal load is increased. While the local heat generation due to the thermal defect of Yb:YAG within the active region is limited to about 15 W, the stored energy is not extracted by a laser seed and results in a large amount of the spontaneous emission that is absorbed by the heat sink and contributes to the total thermal load.

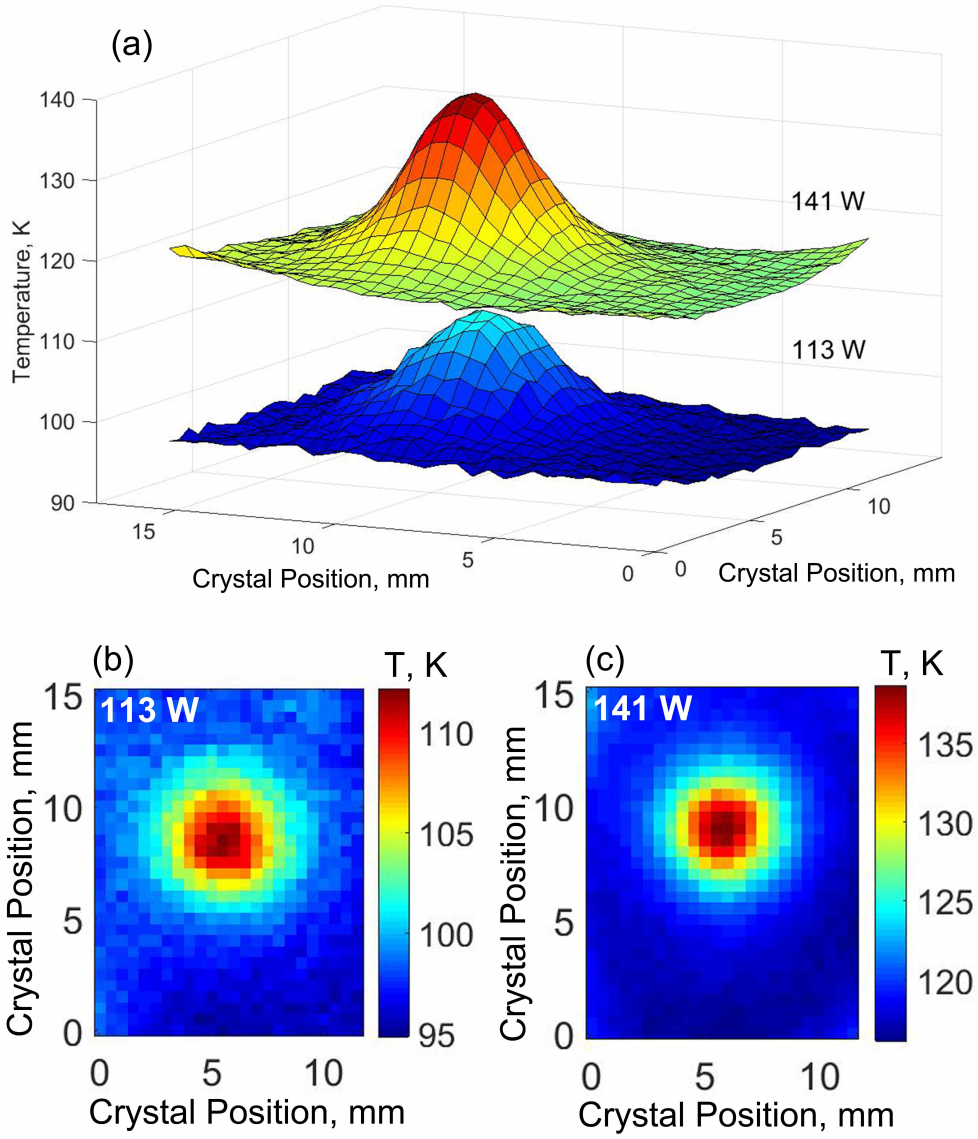

Figure 2.6: 2-D Temperature maps measured for different average pump powers. (a) Temperature maps for 113 W and 141 W average pump powers plotted using the same temperature scale; (b) 2-D temperature map for the 113 W pump power case. The temperature color scale ranges from 95 K to 113 K; (c) 2-D temperature map for the 141 W pump power case. The temperature color scale ranges from 116 K to 138 K.

The temperature is also strongly influenced by the quality of the thermal contact between the Yb:YAG active mirror and the heat sink. Figure 2.8 shows the results for the same (56 W) pump power for two different solder interface conditions. Figure 2.8(b) shows the temperature profile obtained with a poor thermal interface. Figure 2.8(c) shows that obtained with a significantly better thermal interface. The difference is striking, and emphasizes the well-known importance of

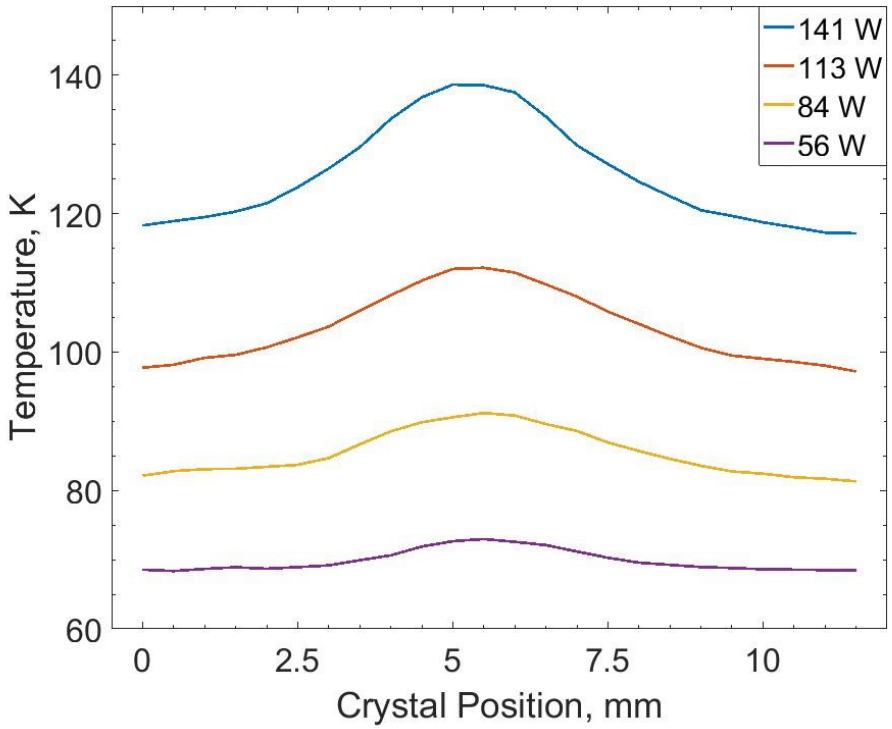

Figure 2.7: One-dimensional cuts of the 2-D temperature maps obtained for average pump powers ranging from 56 W to 141 W.

a good thermal interface in active mirror lasers. These results illustrate the utility of this technique for evaluating the thermal performance of high power cryogenic Yb-doped lasers. For situations where the temperature distribution over the entire amplifier medium volume is required, we have developed the high resolution confocal setup shown in Figure 2.3.

3-D Temperature Mapping

Full 3-D temperature maps were acquired using the confocal microscope setup shown in Figure 2.3. The 3-D temperature maps were obtained by scanning the entire confocal setup over the desired volume with a step size corresponding to 0.36 mm in depth and 0.64 mm transversely. The axial position Z = 2.0 mm is defined to coincide with the front surface of the crystal. A volume of 6.4 mm $\times$ 3.2 mm $\times$ 1.8 mm was scanned. With motorized stages such measurement can be acquired in less than 10 minutes. Figure 2.9 shows the measured 3-D temperature distribution for two different pump powers. Figure 2.9(a) and Figure 2.9(b) show the measured temperature

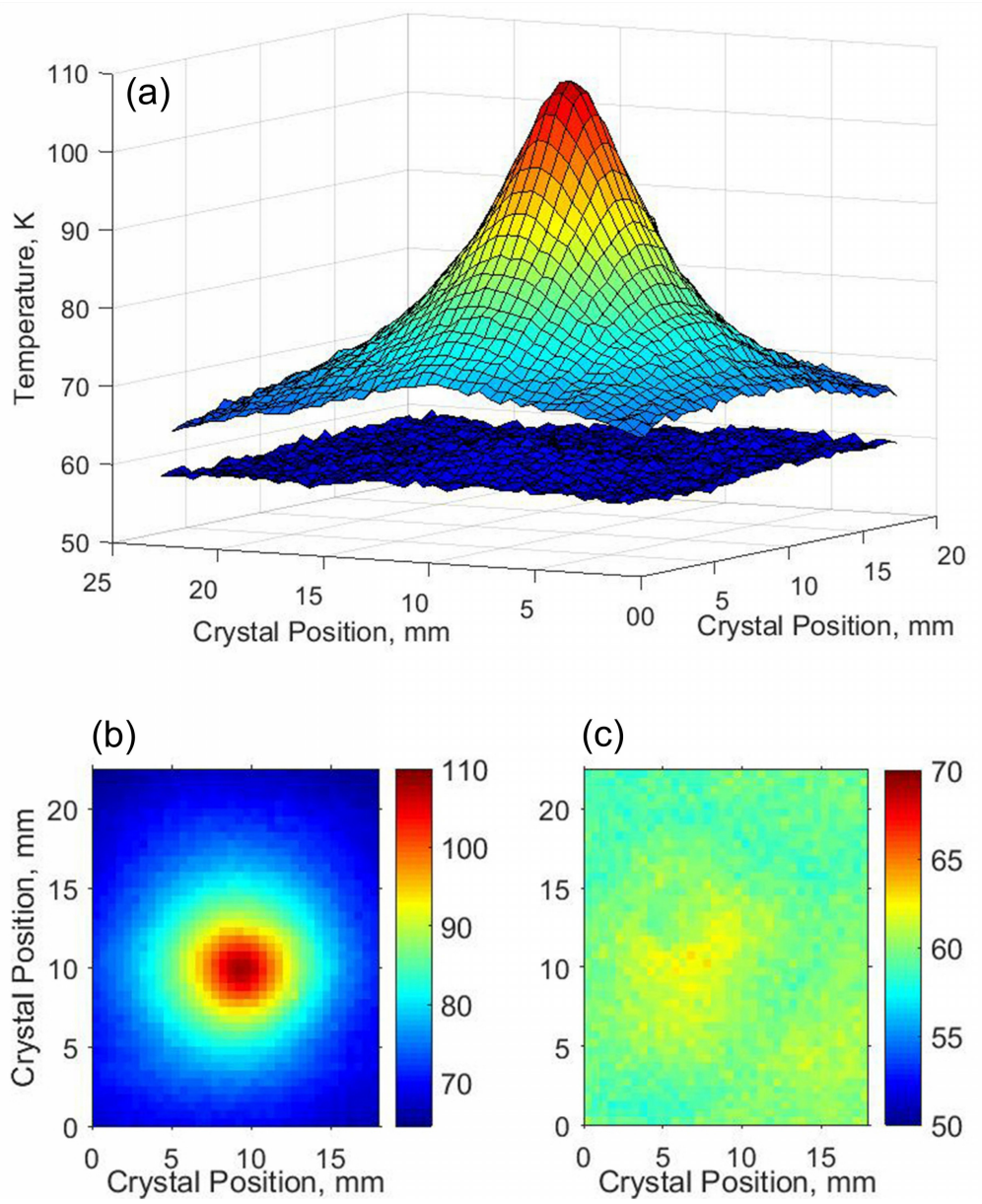

Figure 2.8: 2-D temperature mapping comparison of the different heat transfer conditions at same pump condition. (b) Poor heat transfer interface. (c) Good heat transfer interface. Different temperature scales are used for (b) and (c).

distribution on the crystal surface and the temperature distribution vs. depth from the front surface (AR coated surface) to the back surface (HR coated surface) of the active mirror. At the center of the pump area, the temperature difference between Z = 0.1 mm and Z = 1.9 mm was measured to be about 6 K for 113 W average pump power and about 3 K for 56 W. Figure 2.9(c) and Fig-

ure 2.9(d) show the temperature profile vs. depth measured at the center of pump spot, for these pump powers, respectively.

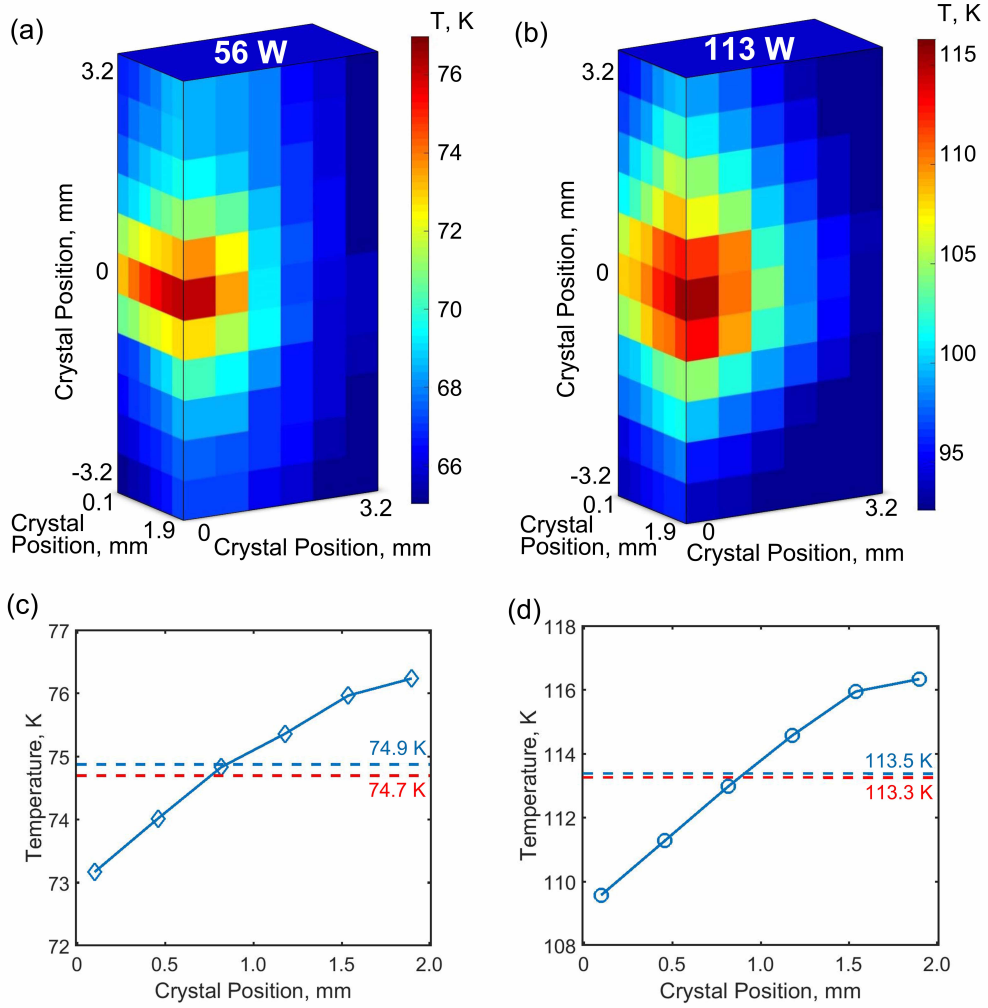

Figure 2.9: 3-D Temperature mapping comparison of the different pump powers. Z = 2.0 mm corresponds to the front surface of the crystal. (a) 3-D temperature profile of 56 W average pump power. (b) 3-D temperature profile obtained with 113 W average pump power. (c) and (d) Plots of the temperature distributions at the center of pump spots for these two average pump powers. The red dashed lines represent the temperature values from 2-D temperature mapping system, and the blue dashed lines represent the average temperature along Z from the 3-D scan.

The dashed lines in Figure 2.9(c) and Figure 2.9(d) show that the average temperature along Z in the 3-D scans is found to be in good agreement with the corresponding measured temperatures in the 2-D scans of Figure 2.6 at the center of the pump spot. Additionally, when the mathematical

sum of the spectra corresponding to different known temperatures are input to the fitting function, the temperature that is obtained is the average temperature. This is evidence that the temperature measured in the 2-D scan is an average of the temperature along orthogonal direction, making the 2-D scans useful on their own in many cases.

Insight from Comparison with Simulations

In principle, the temperature maps can be obtained from thermal model simulations. However, this is hindered by several unknowns. First, are the crystal thermal properties of Yb:YAG that have not been measured over the entire range of interest. Another uncertainty is created by the role of spontaneous emission and amplified spontaneous emission (ASE) and their absorption, which can alter the pump energy distribution. More importantly, as illustrated in Figure 2.8, the unknown value of the thermal impedance of the interface between the crystal and the heat sink can significantly alter the results. Consequently, the temperature maps cannot be obtained from a simple heat transfer model. This emphasizes the value of being able to directly measure the temperature distribution with a method which does not rely on simulations.

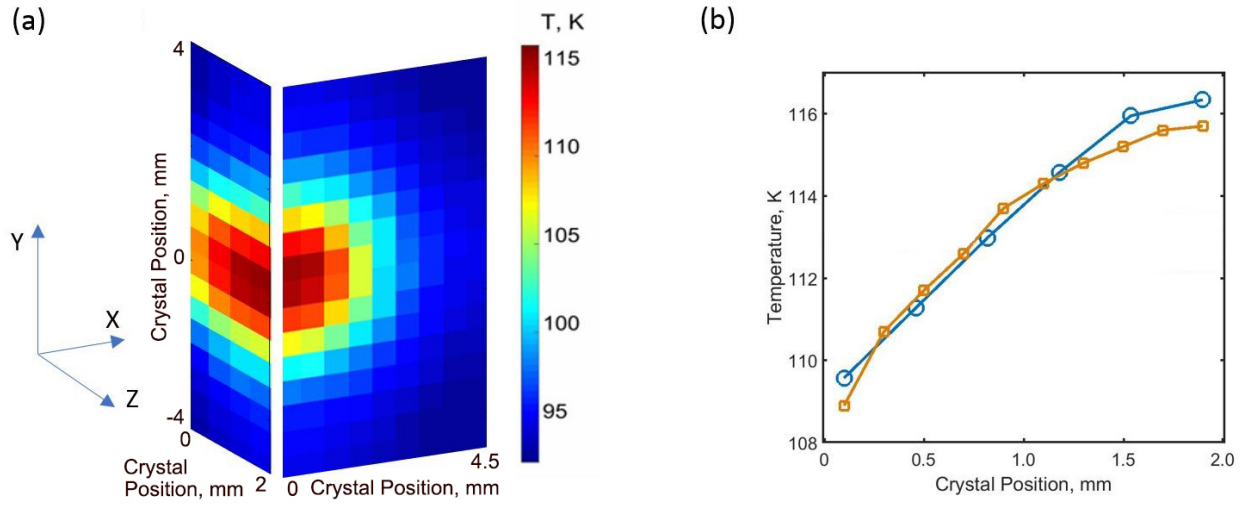

Figure 2.10: (a) Simulated 3-D temperature map and, (b) comparison of the simulated temperature distribution (yellow line) along the axis of the pumped volume with the experimentally measured values (blue circles). The average pump power is 113 W. The pixel size is chosen to be similar with experiments.

Nevertheless, as illustrated in the example below, comparison of the measured values with thermal model simulations can provide additional information on the gain medium. Figure 2.10(a) shows a temperature map resulting from a 3-D finite element simulation of the heat distribution for the case in which the temperatures are in the vicinity to 113 K for which the gain medium thermal parameters are available from the literature without the need for extrapolation [conditions corresponding to Figure 2.9(b) and Figure 2.9(d)]. In this model, the only heat source is assumed to be the thermal defect portion of the pump light. Temperature dependent thermal conductivity values were derived from [16]. The results were obtained neglecting the effects of spontaneous emission and ASE, and leaving as adjustable parameter the thermal impedance to heat transfer through the soldered interface between the crystal and the heat sink. Figure 2.10(b) shows an acceptable agreement between the simulated and measured axial temperature distributions is obtained when the interface thermal conductance is chosen to be $8600\,\mathrm{W{\cdot}m^{-2}{\cdot}K^{-1}}$. Best fits for other pump powers differ in quality, but all of them require similar values of the interface thermal conductance. This example illustrates the temperature mapping technique can be combined with simulations to obtain information about the gain medium beyond the temperature distribution. In case of a gain medium with better known parameters the measurement technique can serve to validate models.

2.5 Conclusions

In conclusion, we have developed a new, in situ method to map the 3-D temperature distribution in the gain medium of high average power cryogenic Yb lasers. The usefulness of this technique was demonstrated measuring the temperature distribution in a 100 mJ, 100 Hz Yb:YAG active mirror amplifier under different pump powers and cooling interface conditions. 2-D transverse temperature maps are shown to give temperature values that correspond to the average temperature in depth. The next chapter presents results of its use for mapping the temperature of kW average power Yb:YAG active mirror amplifiers. The technique should also be applicable to other solid-state lasers materials. This technique, combined with thermal modeling, can be expected to aid in the design of high average power solid-state lasers.

References

[1] W.P. Leemans, A.J. Gonsalves, H-S Mao, K. Nakamura, C. Benedetti, C.B. Schroeder, Cs Tóth, J. Daniels, D.E. Mittelberger, S.S. Bulanov, et al. Multi-GeV electron beams from capillary-discharge-guided subpetawatt laser pulses in the self-trapping regime. *Physical Review Letters*, 113(24):245002, 2014.

[2] Brendan A Reagan, Mark Berrill, Keith A Wernsing, Cory Baumgarten, Mark Woolston, and Jorge J Rocca. High-average-power, 100-Hz-repetition-rate, tabletop soft-X-ray lasers at sub-15-nm wavelengths. *Physical Review A*, 89(5):053820, 2014.

[3] David Alessi, Yong Wang, BM Luther, Liang Yin, DH Martz, MR Woolston, Yanwei Liu, M Berrill, and JJ Rocca. Efficient excitation of gain-saturated sub-9-nm-wavelength tabletop soft-X-ray lasers and lasing down to 7.36 nm. *Physical Review X*, 1(2):021023, 2011.

[4] Ioachim Pupeza, Simon Holzberger, T Eidam, Henning Carstens, D Esser, J Weitenberg, P Rußbüldt, Jens Rauschenberger, J Limpert, Th Udem, et al. Compact high-repetition-rate source of coherent 100 eV radiation. *Nature Photonics*, 7(8):608–612, 2013.

[5] M-C Chen, P Arpin, T Popmintchev, M Gerrity, B Zhang, M Seaberg, D Popmintchev, MM Murnane, and HC Kapteyn. Bright, coherent, ultrafast soft x-ray harmonics spanning the water window from a tabletop light source. *Physical Review Letters*, 105(17):173901, 2010.

[6] A Azhari, S Sulaiman, and AK Prasada Rao. A review on the application of peening processes for surface treatment. In *IOP Conference Series: Materials Science and Engineering*, volume 114, page 012002. IOP Publishing, 2016.

[7] Liang Yin, Hanchen Wang, Brendan A Reagan, Cory Baumgarten, Eric Gullikson, Mark Berrill, Vyacheslav N Shlyaptsev, and Jorge J Rocca. 6.7-nm emission from Gd and Tb plasmas over a broad range of irradiation parameters using a single laser. *Physical Review Applied*, 6(3):034009, 2016.

[8] WR Meier, AM Dunne, KJ Kramer, S Reyes, TM Anklam, LIFE Team, et al. Fusion technology aspects of laser inertial fusion energy (life). *Fusion Engineering and Design*, 89(9-10):2489–2492, 2014.

[9] Saumyabrata Banerjee, Klaus Ertel, Paul D Mason, P Jonathan Phillips, Mariastefania De Vido, Jodie M Smith, Thomas J Butcher, Cristina Hernandez-Gomez, R Justin S Greenhalgh, and John L Collier. Dipole: a 10 J, 10 Hz cryogenic gas cooled multi-slab nanosecond Yb: YAG laser. *Optics Express*, 23(15):19542–19551, 2015.

[10] Saumyabrata Banerjee, Paul D Mason, Klaus Ertel, P Jonathan Phillips, Mariastefania De Vido, Oleg Chekhlov, Martin Divoky, Jan Pilar, Jodie Smith, Thomas Butcher, et al. 100 J-level nanosecond pulsed diode pumped solid state laser. *Optics Letters*, 41(9):2089–2092, 2016.

[11] Brendan A Reagan, Keith A Wernsing, Alden H Curtis, Federico J Furch, Bradley M Luther, Dinesh Patel, Carmen S Menoni, and Jorge J Rocca. Demonstration of a 100 Hz repetition rate gain-saturated diode-pumped table-top soft x-ray laser. *Optics Letters*, 37(17):3624–3626, 2012.

[12] Darren A Rand, Scot EJ Shaw, Juan R Ochoa, Daniel J Ripin, Andrew Taylor, Tso Yee Fan, Hector Martin, Scott Hawes, Jim Zhang, Samvel Sarkisyan, et al. Picosecond pulses from a cryogenically cooled, composite amplifier using Yb: YAG and Yb: GSAG. *Optics Letters*, 36(3):340–342, 2011.

[13] Luis E Zapata, Hua Lin, Anne-Laure Calendron, Huseyin Cankaya, Michael Hemmer, Fabian Reichert, W Ronny Huang, Eduardo Granados, Kyung-Han Hong, and Franz X Kärtner. Cryogenic Yb: YAG composite-thin-disk for high energy and average power amplifiers. *Optics Letters*, 40(11):2610–2613, 2015.

[14] Ondřej Novák, Taisuke Miura, Martin Smrž, Michal Chyla, Siva Sankar Nagisetty, Jiří Mužík, Jens Linnemann, Hana Turčičová, Venkatesan Jambunathan, Ondřej Slezák, et al.

Status of the high average power diode-pumped solid state laser development at HiLASE. *Applied Sciences*, 5(4):637–665, 2015.

[15] Glen A Slack and DW Oliver. Thermal conductivity of garnets and phonon scattering by rare-earth ions. *Physical Review B*, 4(2):592, 1971.

[16] RL Aggarwal, DJ Ripin, JR Ochoa, and TY Fan. Measurement of thermo-optic properties of $Y_3Al_5O_{12}$, $Lu_3Al_5O_{12}$, $YAIO_3$, $LiYF_4$, $LiLuF_4$, BaY_2F_8, $KGd(WO_4)_2$, and $KY(WO_4)_2$ laser crystals in the 80–300 K temperature range. *Journal of Applied Physics*, 98(10):103514, 2005.

[17] Jun Dong, Michael Bass, Yanli Mao, Peizhen Deng, and Fuxi Gan. Dependence of the Yb^{3+} emission cross section and lifetime on temperature and concentration in yttrium aluminum garnet. *JOSA B*, 20(9):1975–1979, 2003.

[18] David C Brown, Rufus L Cone, Yongchen Sun, and Randy W Equall. Yb: YAG absorption at ambient and cryogenic temperatures. *IEEE Journal of selected topics in quantum electronics*, 11(3):604–612, 2005.

[19] Tso Yee Fan, Daniel J Ripin, Roshan L Aggarwal, Juan R Ochoa, Bien Chann, Michael Tilleman, and Joshua Spitzberg. Cryogenic Yb^{3+}-doped solid-state lasers. *IEEE Journal of selected topics in Quantum Electronics*, 13(3):448–459, 2007.

[20] Cory Baumgarten, Michael Pedicone, Herman Bravo, Hanchen Wang, Liang Yin, Carmen S Menoni, Jorge J Rocca, and Brendan A Reagan. 1 J, 0.5 kHz repetition rate picosecond laser. *Optics Letters*, 41(14):3339–3342, 2016.

[21] Paul Mason, Martin Divokỳ, Klaus Ertel, Jan Pilař, Thomas Butcher, Martin Hanuš, Saumyabrata Banerjee, Jonathan Phillips, Jodie Smith, Mariastefania De Vido, et al. Kilowatt average power 100 J-level diode pumped solid state laser. *Optica*, 4(4):438–439, 2017.

[22] Sébastien Chenais, Frédéric Druon, François Balembois, Gaëlle Lucas-Leclin, Yves Fichot, Patrick Georges, Romain Gaume, Bruno Viana, GP Aka, and Daniel Vivien. Thermal lensing

measurements in diode-pumped Yb-doped GdCOB, YCOB, YSO, YAG and KGW. *Optical materials*, 22(2):129–137, 2003.

[23] WA Clarkson. Thermal effects and their mitigation in end-pumped solid-state lasers. *Journal of Physics D: Applied Physics*, 34(16):2381, 2001.

[24] J Petit, B Viana, and Ph Goldner. Internal temperature measurement of an ytterbium doped material under laser operation. *Optics express*, 19(2):1138–1146, 2011.

[25] Hee-Jong Moon, Changhwan Lim, Guang-Hoon Kim, and Uk Kang. Study of operation dynamics for crystal temperature measurement in a diode end-pumped monolithic Yb: YAG laser. *Optics Express*, 21(25):31506–31520, 2013.

[26] Real-time measurement of temperature distribution inside a gain medium of a diode-pumped Er^{3+}/Yb^{3+} 1.55 μm laser.

[27] Sébastien Chénais, Sébastien Forget, Frédéric Druon, François Balembois, and Patrick Georges. Direct and absolute temperature mapping and heat transfer measurements in diode-end-pumped Yb: YAG. *Applied Physics B*, 79(2):221–224, 2004.

[28] L Van Pieterson, M Heeroma, E De Heer, and A Meijerink. Charge transfer luminescence of Yb^{3+}. *Journal of Luminescence*, 91(3-4):177–193, 2000.

[29] Xu-dong Wang, Otto S Wolfbeis, and Robert J Meier. Luminescent probes and sensors for temperature. *Chemical Society Reviews*, 42(19):7834–7869, 2013.

[30] Miroslav D Dramićanin. Sensing temperature via downshifting emissions of lanthanide-doped metal oxides and salts. A review. *Methods and applications in fluorescence*, 4(4):042001, 2016.

[31] Jan Brübach, Christian Pflitsch, Andreas Dreizler, and Burak Atakan. On surface temperature measurements with thermographic phosphors: A review. *Progress in Energy and Combustion Science*, 39(1):37–60, 2013.

[32] Tao Cai, Dong Kim, Mirae Kim, Ying Zheng Liu, and Kyung Chun Kim. Two-dimensional thermographic phosphor thermometry in a cryogenic environment. *Measurement Science and Technology*, 28(1):015201, 2016.

[33] Hiroaki Furuse, Junji Kawanaka, Noriaki Miyanaga, Haik Chosrowjan, Masayuki Fujita, Kenji Takeshita, and Yasukazu Izawa. Output characteristics of high power cryogenic yb: Yag tram laser oscillator. *Optics express*, 20(19):21739–21748, 2012.

[34] Fit Data with a Shallow Neural Network (The MathWorks, Inc., 2018).

[35] Warren S McCulloch and Walter Pitts. A logical calculus of the ideas immanent in nervous activity. *The bulletin of mathematical biophysics*, 5(4):115–133, 1943.

[36] Kurt Hornik, Maxwell Stinchcombe, and Halbert White. Multilayer feedforward networks are universal approximators. *Neural networks*, 2(5):359–366, 1989.

[37] Paul Davidovits and M David Egger. Scanning laser microscope. *Nature*, 223(5208):831–831, 1969.

[38] C. M. Bishop. Pattern recognition. *Machine learning*, 128(9), 2006.

[39] Jerome H Friedman. Data Mining and Statistics: What's the connection? *Computing science and statistics*, 29(1):3–9, 1998.

[40] Mehryar Mohri, Afshin Rostamizadeh, and Ameet Talwalkar. *Foundations of machine learning*. MIT press, 2018.

[41] James Seligman. *Artificial intelligence and machine learning and marketing management*. Lulu. com, 2018.

[42] Steven D Brown, Stephen T Sum, Frederic Despagne, and Barry K Lavine. Chemometrics. *Analytical Chemistry*, 68(12):21–62, 1996.

[43] Dragan A Cirovic. Feed-forward artificial neural networks: applications to spectroscopy. *TrAC Trends in Analytical Chemistry*, 16(3):148–155, 1997.

[44] Daniel Svozil, Vladimir Kvasnicka, and Jiri Pospichal. Introduction to multi-layer feed-forward neural networks. *Chemometrics and intelligent laboratory systems*, 39(1):43–62, 1997.

[45] A.H. Curtis, B.A. Reagan, K.A. Wernsing, F.J. Furch, B.M. Luther, and J.J. Rocca. Demonstration of a compact 100 Hz, 0.1 J, diode-pumped picosecond laser. *Optics Letters*, 36(11):2164–2166, 2011.

Chapter 3

Thermal Behavior Characterization of a Kilowatt-Power-Level Cryogenically Cooled Yb:YAG Active Mirror Laser Amplifier

The demonstration of a new 3-D temperature mapping technique that can be used to noninvasively acquire real-time temperature information of the Yb:YAG at cryogenic temperature range was described in Chapter 2. Based on this temperature mapping technique, Chapter 3 presents the measurement and analysis of the thermal behavior of a high energy kilowatt average power diode-pumped cryogenically-cooled Yb:YAG active mirror laser amplifier. Temperature distribution maps of the laser material at pump powers up to 1 kW were obtained for the first time by spatially and spectrally resolving the fluorescence induced by a scanning laser probe beam. The wavefront distortion resulting from the front surface deformation and the overall deformation of the gain medium assembly were measured using a Mach-Zehnder interferometer. The measured deformations agree well with the results of thermo-mechanical modeling using finite element method (FEM) simulations and with the results of focal length shift measurements. The relative contributions to the optical path difference (OPD) of the mechanical deformations, refractive index changes, and electronic contribution are discussed. It is shown that the Cr^{4+}:YAG cladding plays a significant role in both the temperature distribution and the overall OPD changes. The pump-induced mechanical deformations of the assembly dominate the OPD changes in this kilowatt average pump power cryogenically-cooled Yb:YAG active mirror laser. Apart from the temperature measurement results at unseeded condition, the measured maximum temperature of the laser material with >500 W extracted energy while pumped with >1750 W pump power is presented and discussed. It provides the evidence that, with improved cooling system and beam divergency con-

trol system, the main amplifier stage of a previously demonstrated 500 Hz, 1.4 J amplifier system could be scaled to 1 kHz repetition rate.

3.1 Introduction

Diode-pumped solid-state lasers with simultaneously high energy and high average power have advanced rapidly due to the demand from various applications including compact particle accelerators [1], extreme ultraviolet lithography [2], laser processing of materials [3] and the future prospect of practical inertial confinement fusion power generation [4]. By taking advantage of the good thermal properties [5, 6] and gain characteristics [7, 8] of Yb:YAG at cryogenic temperature, several high average power chirped pulse amplification (CPA) lasers with high pulse energies have recently been developed [9–11]. These include the demonstration of a cryogenic Yb:YAG active mirror CPA laser that produced 1.4 J stretched pulses at 0.5 kHz repetition rate (0.75 kW average power) compressed to about 5 ps [9], the recent first demonstration of 1 J pulses at 1 kHz repetition rate [10], and the operation of a cryogenic gas-cooled Yb:YAG laser that can generate 100 J pulses at 10 Hz repetition rate with nanosecond pulse duration [11].

With kW-level pump power incident on the active material in these systems, thermal gradients can lead to thermal lensing, depolarization and, ultimately, catastrophic stress fracture of the material. To evaluate and help minimize these thermal effects in such a high average power amplifier, a thermal analysis of the laser material under high pump power is necessary. This evaluation can benefit from the use of a technique that can map the temperature distribution at cryogenic conditions. Several research groups have theoretically and experimentally investigated the thermal effects and the pump-induced optical path difference (OPD) in end-pumped Yb:YAG laser amplifiers at room temperature with relatively low average pump powers [12–15]. Chénais et al. reported on a study of thermal effects in several Yb-doped materials in which the contribution to the OPD due to mechanical and optical effects was determined and methods of measuring the thermal lens power in solid-state lasers were comprehensively reviewed [12]. Albach et al. discussed the deformation of a room temperature active mirror amplifier as a free standing disk relying on experimental data

from the Lucia laser project [13]. Recently, Tamer et al. discussed the thermal contribution to the pump-induced wavefront aberrations and determined the electronic contributions caused by changes in the population inversion upon pumping [14]. However, at cryogenic temperature, the properties of Yb:YAG and other Yb-doped materials dramatically change. Several papers have presented simulated analyses of high average power cryogenic-cooled Yb-doped lasers [16–18]. Nevertheless, to our knowledge there are no publications presenting experimental results from a complete thermal behavior analysis including measured temperature distributions, wavefront distortions, and their relationship at cryogenic temperature under kW-level average power pump.

This chapter presents a complete analysis of the thermal behavior of a kW-power level cryogenically cooled active mirror Yb:YAG amplifier. We present what is, to the best of our knowledge, the first temperature map of a cryogenically-cooled kW class laser amplifier. Two-dimensional (2-D) temperature distribution maps of the active material were measured with the spectroscopic temperature measurement technique described in Chapter 2 and Ref. [19]. A Mach–Zehnder interferometer was used to simultaneously measure the front surface deformation and the overall wavefront deformation of the Yb:YAG assembly under different pump powers. A set of thermal lens focus shift data was also measured to compare with the thermal lens powers deduced from the interferograms. These results show good agreement with each other and also with those obtained from a simulation that uses a finite element method to determine the thermal profile and deformation. Finally, we find the major source of wavefront deformation by comparing the relative contributions of the thermal change in refractive index, the electronically-induced change, and the thermal deformation of the cryogenically-cooled Yb:YAG laser amplifier. It is found that, for the case of high average power cryogenically-cooled Yb:YAG with relatively thin gain media, the mechanical deformation dominates the overall OPD changes and wavefront aberrations. The contribution of the thermal refractive index change is second in importance, while the electronically-induced OPD can be ignored at these conditions. This investigation provides helpful information for the design of high power active mirror amplifiers and for benchmarking models that can be used to scale these laser amplifiers to higher average power.

3.2 Experimental Setup

The measurements were conducted on the final amplification stage of the 1.4 J, 0.5 kHz repetition rate picosecond laser system described in Ref. [9]. The active material (shown in Figure 3.1) used in the experiment is a 2 mm thick, 30 mm $\times$ 30 mm area, 3%-at doped Yb:YAG slab, which is surrounded by a 10 mm wide Cr^{4+}:YAG cladding optically bonded along the perimeter for amplified spontaneous emission (ASE) and parasitic lasing suppression. The front face of the Yb^{3+}/Cr^{4+}:YAG assembly is optically bonded to a 3 mm thick undoped YAG cap which provides structural integrity and ASE mitigation. The entire assembly is mounted on a cryogenically-cooled head and cooled by flowing liquid nitrogen at 77 K. The amplifier was pumped by a 940 nm wavelength, 6 kW, 60 bar laser diode array. The duration of the pump pulse was 300 µs with a repetition rate of 1 kHz. The pump diode output beam was conformed by beam profile shaping optics to form a nearly flat-top hexagonal pump spot on the crystal with a circumscribed diameter of 16 mm, and the unabsorbed pump light after the first pass was relay imaged back onto the active region by a spherical mirror, allowing for a pump absorption of greater than 90%. The average pump powers were varied up to 1 kW while keeping the pump pulse repetition rate at a constant 1 kHz.

To investigate the thermal behavior of this kW-level active mirror amplifier, several diagnostics were used. The temperature distribution in the cryogenically-cooled lasing media was measured with a recently developed temperature mapping technique described in Ref. [19]. A Mach-Zehnder interferometer was employed to monitor wavefront changes of a beam reflected from the front surface of the active mirror and a beam reflected from the back surface and double passing the bulk of the crystal. Additionally, the pump-induced shift in the waist position of a focusing beam was measured to determine the thermal lens power under different pump powers and compare with the results from the interferograms. The setup used for each of these measurements is described below.

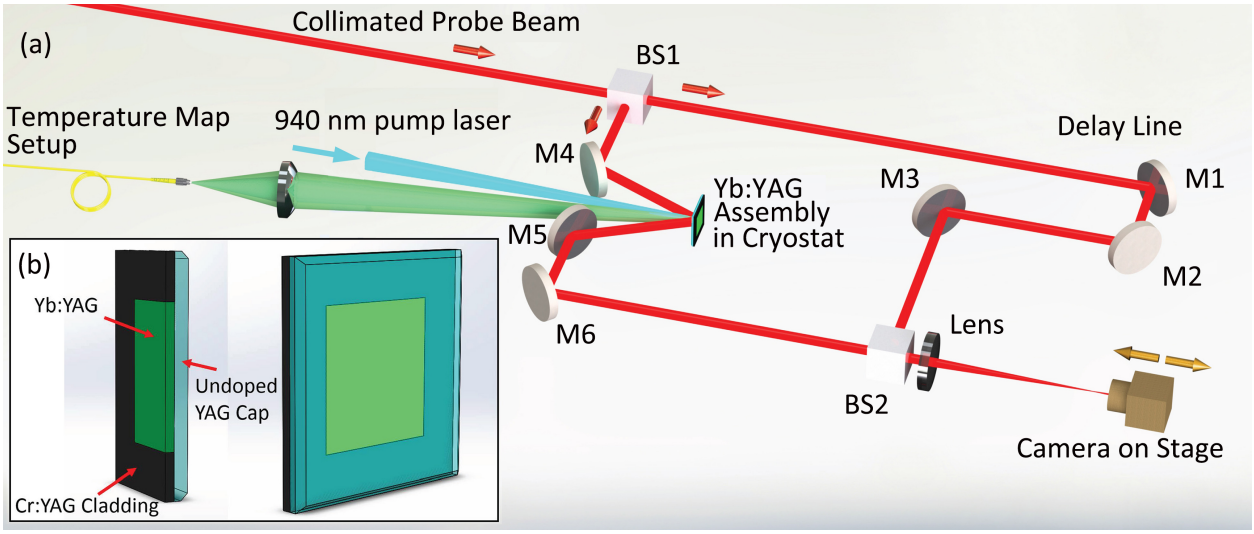

Figure 3.1: Schematic of the experiment setup (a) and the Yb^{3+}/Cr^{4+}:YAG and YAG cap assembly (b). In the Mach-Zehnder interferometer measurement, a 660 nm collimated semiconductor laser probe beam is used for both front surface and overall wavefront measurements. BS1 and BS2 are beamsplitters. M1 to M6 are silver mirrors. A FL=300 mm lens is used to image the fringes onto a camera. For focus shift measurements, the collimated probe beam is changed to a 1030 nm laser and the lens is replaced by a FL=750 mm lens. The camera is scanned to determine the location of the focus.

3.2.1 Temperature Mapping Measurement

The temperature mapping setup is shown in Figure 3.1(a). As described in a recent publication [19], the fluorescence spectrum of Yb:YAG from 1015 nm to 1029 nm can be used to calculate the temperature with a neural network based algorithm that is calibrated by measuring spectra at known temperatures and fluorescence intensities. The 2-D temperature maps were obtained by raster scanning the tips of the localized probe and signal fiber over an area of 20 mm $\times$ 20 mm of the active mirror Yb:YAG assembly, which contains the entire pump area. The step size was selected to be 0.5 mm. As discussed in Ref. [19], the 2-D temperature maps obtained by this method provides the depth-averaged temperature of the Yb:YAG slab. In addition, to obtain the temperature profile in depth we conducted a one dimensional (1-D) scan from the front surface to the back surface of the Yb:YAG crystal at the center of the pump spot using a confocal geometry also described in Ref. [19].

3.2.2 Mach-Zehnder Interferometer

To measure the wavefront distortion, a Mach-Zehnder interferometer was built as shown in Figure 3.1(a). To acquire the pump-induced OPD from both the front surface and the overall crystal assembly, a collimated 660 nm continuous wave (CW) diode laser was used as a probe beam to produce separate reflections from the two surfaces. As shown in Figure 3.1(a), a 50:50 non-polarizing beamsplitter is used to separate the 660 nm laser into two beams. One beam probes the crystal assembly and the other one goes into a delay line. The 660 nm diode laser is used because the spectral bandwidth is about 1 nm, corresponding to a coherence length of 0.2 mm, which allows us to avoid unwanted interference fringes arising from simultaneous reflections from the various surfaces of the gain medium assembly and the cryostat chamber window. A second 50:50 non-polarizing beamsplitter is used to recombine the beams. By changing the length of the delay line, the fringes originating from the front and back surface reflections can be clearly differentiated. A 300 mm focal length lens is used to image the surface under study onto a camera. The effective pixel size is 15 µm $\times$ 15 µm, which was obtained by imaging a calibrated test pattern. The pump and cooling conditions were the same as those during the temperature mapping measurement.

3.2.3 Focal Length Shift Measurement

The focal length shift measurement set up shares part of the Mach-Zehnder interferometer layout. A collimated 1030 nm probe beam from a separate laser was utilized for this measurement to take advantage of the HR coating on the back surface of the Yb:YAG crystal. The imaging lens was replaced by a 750 mm focal length lens for greater sensitivity of the thermal lens focal length measurement. The camera was put on a linear translation stage to analyze the beam focus over a 50 mm range. By performing measurements of the beam diameter at different locations to determine the precise position of the focus at various pump powers [20], the shift of the focus location was determined and the thermal lens power was calculated.

3.3 Simulations

In order to simulate the thermal distribution of the Yb:YAG assembly and the wavefront distortion that it induces, we used a finite element method and the same pump conditions as the measurements. By using the calculated temperature distribution, we determined the thermal expansion and stress distribution within the assembly, from which the deformation of the assembly can be obtained. By using these data, the OPD and thermal lens power can be calculated and compared with the experimental results.

3.3.1 Thermal Distribution Simulation

In the finite element method simulations, the distribution of the pump power absorbed by the Yb:YAG has a flat-top profile with the same shape as the pump beam employed in the experiment. The absorption of the Yb:YAG crystal is over 90%. The heat power applied in the model is primarily calculated from the geometry of the gain medium and the quantum defect of the materials. Under the non-extraction condition, most of the pump energy is dissipated radiatively as the form of ASE and the rest of the energy stored in the upper level decays non-radiatively in the form of heat according to the quantum defect of the active material [12, 21]. To account for ASE emission and absorption we created a 3-D Monte Carlo ray-trace program to simulate the generation, propagation, and absorption of the ASE. This was done by generating many rays corresponding to the spontaneous emission and tracking each ray as it is amplified, absorbed, reflected or transmitted through the crystal until it eventually leaves the medium or is completely absorbed in the cladding. This simulation uses the experimentally measured transmission of the multilayer-coated front face as a function of angle and assigns a fixed refractive index to calculate Fresnel reflections or total internal reflection at the remaining crystal interfaces and edges. The internal gain is computed by solving the population equations self consistently with the local amplified emission intensity to account for losses due to stimulated emission. We compute that about 60% of the ASE is trapped in the assembly and is absorbed by the Cr^{4+}:YAG cladding [22]. Of this fraction, about 65% is transformed into thermal power that heats the Cr^{4+}:YAG cladding [23]. The rest of absorbed

energy is re-emitted as broadband 1400 nm wavelength radiation that is assumed to exit the assembly [24]. The heat density in the Cr^{4+}:YAG can be calculated with the total thermal power and the absorption coefficient of the Cr^{4+}:YAG cladding, which we measured to be $8.4\,cm^{-1}$. The back surface of assembly is cooled by flowing liquid nitrogen at a temperature of 77 K. An interface coefficient of $6700\,W/m^2K$ is used, that gives good agreement with the measured temperature maps. The temperature maps are used to simulate the stress distribution using a finite element method, as discussed below.

3.3.2 Pump-induced OPD

The overall pump-induced OPD in the active mirror amplifier can be calculated by Eq.(3.1) [14, 25]:

$$\begin{aligned}\phi(x,y) = {} & 2(n_0-1)\cdot FS(x,y) - 2n_0 \cdot BS(x,y) \\ & + 2\cdot\frac{dn}{dT}\cdot(T(x,y)-T_0)L \\ & + \frac{4\pi}{n_0}\cdot(\frac{n_0^2+2}{3})^2\cdot\Delta\alpha\cdot\Delta N(x,y)l\end{aligned} \tag{3.1}$$

The first two terms are the front surface induced OPD and the back surface induced OPD. $\mathbf{n_0}$ is the refractive index. $\mathbf{FS}(\mathbf{x},\mathbf{y})$ and $\mathbf{BS}(\mathbf{x},\mathbf{y})$ are the front surface deformation and back surface deformation, respectively. These can be determined by using a finite element method to simulate the stress distribution from the simulated temperature distributions, which agree with the measured temperature distributions. The third term gives the integrated OPD related to $\mathbf{dn/dT}$ from a round trip of the beam through the assembly. $(\mathbf{T}(\mathbf{x},\mathbf{y})-\mathbf{T_0})$ is the mean of the temperature difference along the material thickness $\mathbf{L}$ [14, 25]. In the fourth term, $\mathbf{\Delta N}(\mathbf{x},\mathbf{y})$ is the spatial profile of the inverted population within the pumped region averaged over the length and $\mathbf{\Delta}\alpha$ is the change in polarizability due to the inversion [26]. l is the thickness of active material. The contribution of the photoelastic effect [12, 14] is calculated to be negligible in our case. The overall OPD described in Eq.(3.1) can be considered as two separate parts, thermally-induced OPD and electronically-induced OPD. The summation of the first three terms constitutes the thermal

contribution because they are all related to the thermal distribution in the assembly. The pump-induced thermal distribution not only leads to refractive index changes, but also induces mechanical deformations which are related to the thermal expansion and photoelastic effect over the entire gain medium assembly. The fourth term is the electronic contribution originating from the excited laser-active ions, which leads to a refractive index change in the pumped active material. The inverted population can be calculated from the small signal gain and the stimulated emission cross-section of the laser material at cryogenic temperature. The electronically-induced OPD is typically non-negligible in the room temperature case [14, 25]. By using the polarizability of Yb:YAG measured in Ref. [25] of $1.95 \times 10^{-26}\,\mathrm{cm}^3$ and an approximate maximum population inversion of $\Delta N = 1.5 \times 10^{19}$, a maximum OPD due to the polarizability change of the material of only 12.6 nm (about $\lambda/100$) is obtained at cryogenic temperature. Based on this calculation and in agreement with the measurements below, the electronically-induced OPD is much smaller than that due to the thermo-optic effect and thermal deformation and can be safely ignored. Note that this is contrary to the conclusions of Ref. [14], however this can be explained by the lower population inversion densities required to achieve significant gain when using Yb:YAG at cryogenic temperature compared to the room temperature measurements of Ref. [14].

3.4 Results and Discussions

Figure 3.2(a) and Figure 3.2(d) show the measured 2-D temperature distribution of the Yb:YAG slab at 444 W and 1010 W average pump power respectively. Figure 3.2(b) and Figure 3.2(e) are the corresponding simulated depth-averaged temperature distributions from finite element method simulations of the same area. The peak-to-valley temperature difference at 444 W and 1010 W average pump power is 4.6 K and 13.5 K, respectively. As can be seen in both conditions, the measured results agree well with the simulated results in both the shape and the temperature differences. The hexagonal shape is due to the spatial profile of the pump. There is an asymmetry on the right side of the measured temperature map caused by the off-center pump location, closer to the Cr^{4+}:YAG cladding. Figure 3.2(c) and Figure 3.2(f) show vertical lineouts of the simulated

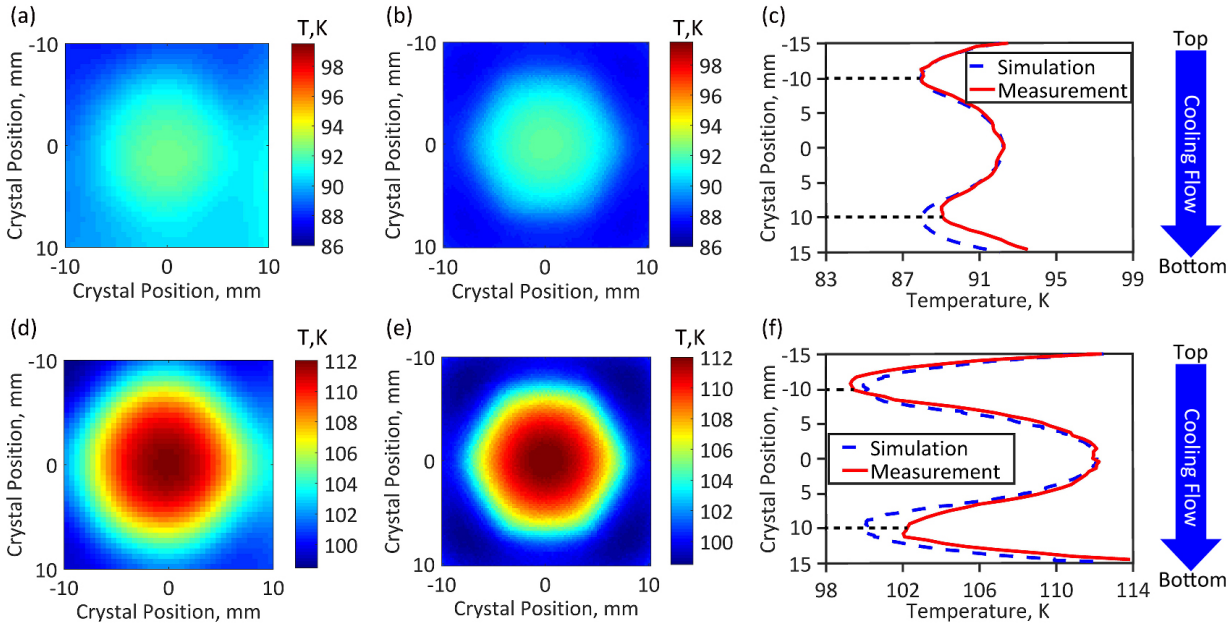

Figure 3.2: (a) Measured and (b) simulated 2-D temperature distribution in the Yb:YAG slab under 444 W pump power, (c) Vertical cut through the center of the pump area under 444 W pump power. (d) Measured and (e) simulated 2-D temperature distribution of the Yb:YAG slab under 1010 W pump power. The temperature scale in (d) and (e) is offset respect to that in (a) and (b) while keeping the same temperature span, to more clearly show the temperature variations. (f) Vertical cut through the center of the pump area under 1010 W pump power. In (c) and (f), the blue dashed line is the simulation result and the red solid line is the measurement result. The direction of cooling flow is from top to bottom for all figures.

and measured temperature results across the entire width of the Yb:YAG from cladding to cladding through the center of the pump for 444 W and 1010 W average pump power, respectively. The large amount of absorbed ASE in the Cr^{4+}:YAG cladding heats the side of the Yb:YAG and creates the "W" shaped temperature distribution. The temperature at the very edge of the Yb:YAG is higher than that at the center of the pump spot. The cooling liquid runs from top to bottom along the assembly's back surface. The temperature difference in depth between the front and back surfaces was measured using the confocal microscope setup described in Ref. [19]. At the center of the pump spot, temperature differences were determined to be 2 K, 3 K and 4.7 K for pump powers of 444 W, 761 W and 1010 W respectively, which are consistent with the simulated temperature distributions at these pump powers.

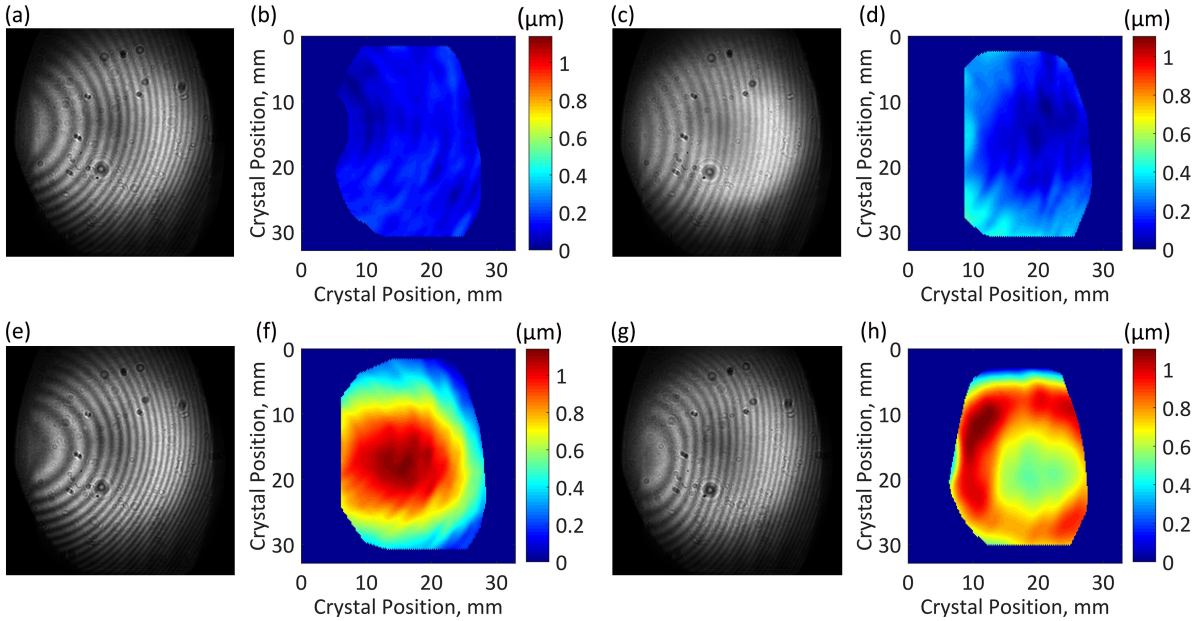

Figure 3.3: Interferometry measurement results for different average pump powers. (a) and (c) are raw data from the front and back surface reflections at 288 W, respectively. (b) and (d) are the corresponding front surface and overall wavefront deformation, respectively. (e) and (g) are the fringes raw data from front surface reflection and back surface reflection at 1010 W, respectively. (f) and (h) are the corresponding front surface and overall wavefront deformation, respectively.

The interferometry results are shown in Figure 3.3. Figure 3.3(a) is the raw interferogram collected from the front surface of the Yb:YAG crystal for 288 W pump power. An interferogram of the crystal was obtained with the pump diode off to use as a reference. Figure 3.3(b) shows the wavefront deformation determined by subtracting this no pump reference from the 288 W result. Figure 3.3(e) and Figure 3.3(f) show the raw interferogram and wavefront for the 1010 W case after reference subtraction, respectively. Again, for an easier comparison, the scale in Figure 3.3(b) and Figure 3.3(f) is kept the same. The changes in wavefront induced by the front surface for these two pump powers are significant. With 288 W pump power, the deformation from the edge to the center is about 0.2 µm with a relatively flat profile. However, under 1010 W pump power, the deformation from the edge to the center is about 1.1 µm.

Figure 3.3(c) and Figure 3.3(d) show the interferogram and the overall wavefront deformation of the beam passing throughout the entire assembly for 288 W pump power (entering through the front face, reflected from the back surface, and exciting through the front surface). The same

set of data under 1010 W pump power is presented in Figure 3.3(g) and Figure 3.3(h). As can be observed from these figures, at high pump powers the overall wavefront deformation has a "donut" shape, which is related to the effect of spontaneous emission and ASE absorption in the Cr^{4+}:YAG cladding. In both cases, the chamber window limits the accessible angle on the left side of Figure 3.3(f) and on the right side of Figure 3.3(h). Nevertheless, the detected area covers the entire pump area and it is enough to observe the entire change in the wavefront.

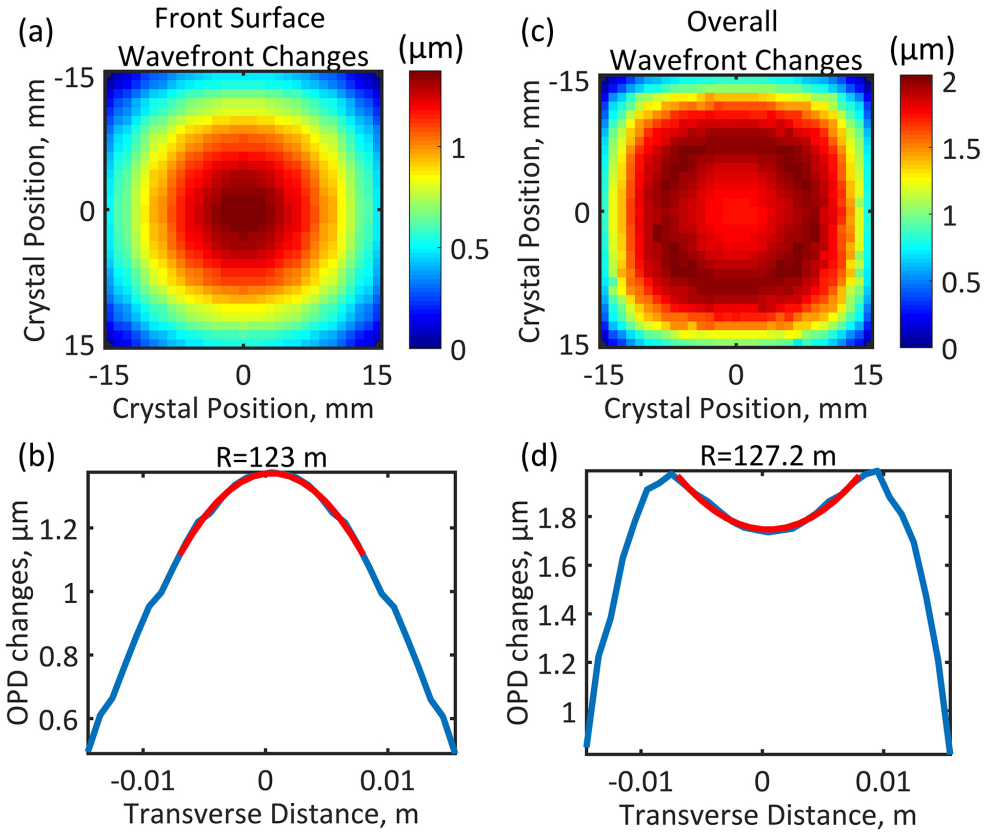

Figure 3.4: (a) Simulated front surface induced wavefront deformation, and (c) simulated overall wavefront deformation. (b) and (d) show vertical lineouts of the front surface and overall wavefront deformations, respectively, and their radii of curvature. The red line is the fitting of the parabolic curve.

Simulation results of the OPD corresponding to the 1010 W pump power condition can be seen in Figure 3.4. Figure 3.4(a) and Figure 3.4(c) show the calculated wavefront change induced by the front surface and the overall wavefront change based on the temperature distributions, respectively. As can be seen from Figure 3.3 and Figure 3.4, the simulated wavefront deformations share the

same shape as the measurement results for both front surface deformation and overall wavefront change. Within the measured area, the simulated wavefront change is in good agreement with the measurements.

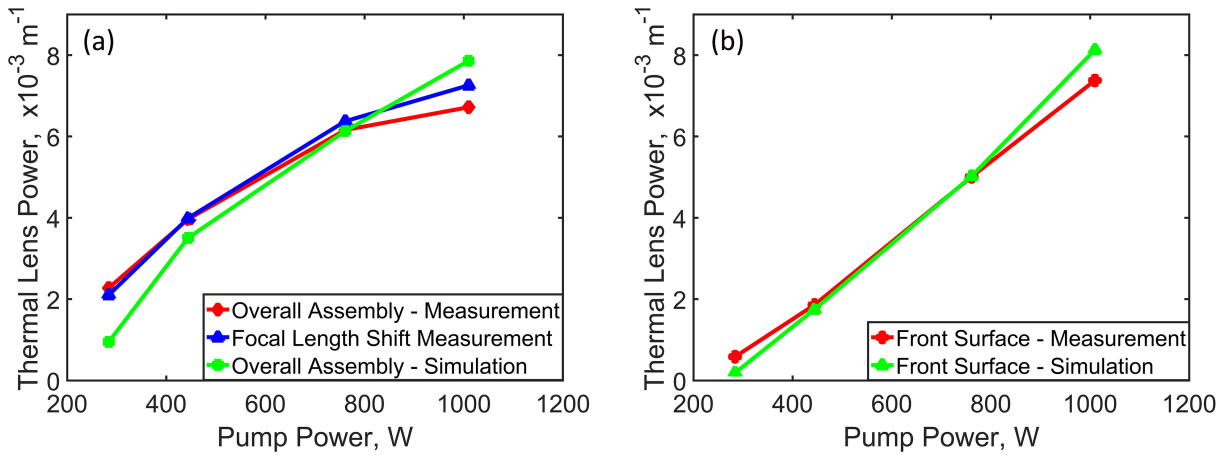

Figure 3.5: Comparison of the thermal lens power from the simulation and measurements due to (a) overall wavefront changes and focus shifts, and (b) front surface deformation wavefront changes.

The thermal lens power determined by measuring a focal length shift was compared with the thermal lens power values deduced from the wavefront measurement results and with the simulations. The results are shown in Figure 3.5(a). As can be seen in Figure 3.5(a), a good agreement between the two different measurement methods and the simulation is observed for all pump powers. Figure 3.5(b) compares the results for the radius of curvature of the front surface within the pump area from the interferograms and the simulated front surface deformations. These wavefront results are slightly more favorable than those reported in Ref. [10], primarily due to changes in the cryo-cooling conditions, which illustrates the importance of making in situ measurements. The overall OPD is dominated by the mechanical deformation, and the contribution due to the variation of the refractive index with temperature is secondary. In other words, the crystal expansion caused by the temperature gradient is the most important factor in this high power diode-pumped cryogenically-cooled Yb:YAG active mirror amplifier.

The temperature distribution for the seeded condition differs from the unseeded case. The biggest difference is the reduced power deposited in the Cr^{4+}:YAG cladding in the seeded case. Table 3.1 shows an estimate of the fraction of the pump power that is transferred to heat in the different parts of the Yb^{3+}/Cr^{4+}:YAG assembly, under the assumption that 36% of the deposited pump power is extracted by the seed. In both cases the power deposited in the Yb:YAG due to the thermal defect is the same, about 8.7%. The energy which is not extracted by the amplified seed decays in the form of ASE, the majority of which is absorbed by the Cr^{4+}:YAG cladding.

Table 3.1: Heat power comparison between seeded and non-extraction in different parts of the assembly.

Fraction of Power	Seeded Condition	Non-extraction Condition
Total Absorbed Power	100%	100%
16 mm Yb:YAG	8.7%	8.7%
1030 nm Power	100%×(1-8.7%)×36% = 32.9%	0
ASE Power	100%×(1-8.7%)×(1-36%) = 58.4%	100%×(1-8.7%)=91.3%
Cr^{4+}:YAG Absorbed Power	58.4%×60%= 35.0%	91.3%×60%= 54.8%
Cr^{4+}:YAG Heating Power	35.0%×65%= 22.8%	54.8%×65%= 42.3%

While the heat power deposited in the Yb:YAG is the same for both cases, the power on the Cr^{4+}:YAG cladding is reduced to almost half in the seeded condition, which means the temperature in the Cr^{4+}:YAG will be relatively lower in seeded condition. Due to the high thermal conductivity of the YAG material, it will result in a lower temperature in the Yb:YAG as well.

A temperature measurement under seeded condition was conducted at a different of pump powers. The temperature of Yb:YAG at the center of the pump area was measured. As can be seen in Figure 3.6, the temperature at the center of crystal in the unseeded condition is always higher than the temperature in the seeded condition. At the highest pump power of 1.75 kW, the temperature of the Yb:YAG under the seeded condition remains below 130 K. At this pump power, the temperature difference between seeding and non-extraction condition is about 8 K.

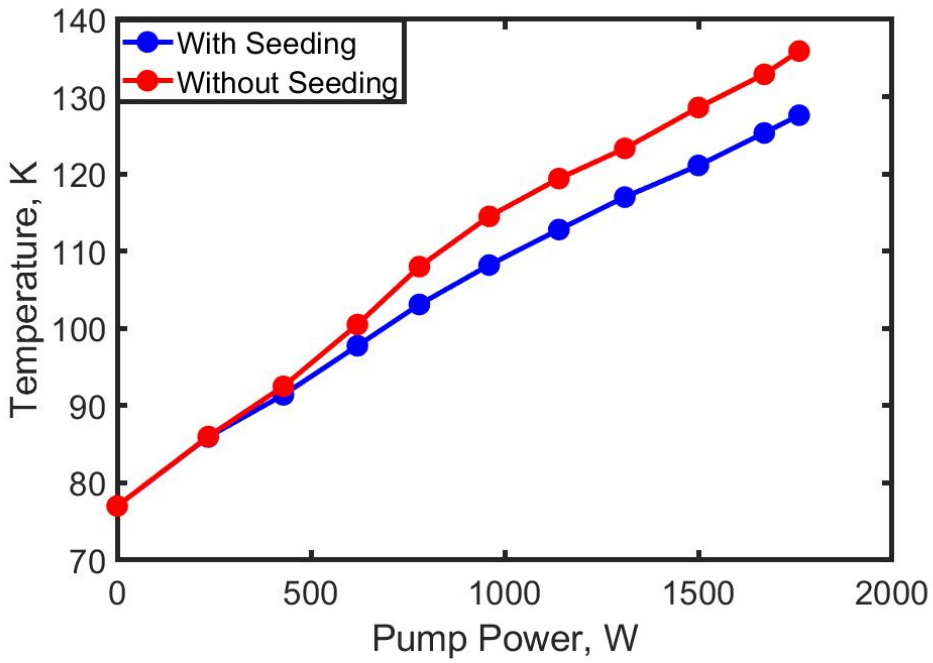

Figure 3.6: Measured temperature of one Yb:YAG active mirror in the final amplifier at the center of the pump with and without seeding vs. pump power.

3.5 Conclusion

In summary, we have characterized the thermal behavior of a cryogenically-cooled Yb:YAG active mirror laser amplifier pumped at kilowatt average power. The measurements provide maps of the temperature distribution in the gain medium at these high pump power levels for the first time. Radial temperature differences of 4.6 K and 13.5 K were measured at 444 W and 1010 W average pump power, respectively. The wavefront changes induced by the deformation of the front surface and the overall assembly were quantified by a Mach-Zehnder interferometer. The interferogram results show that the front surface induced wavefront deformation has a convex shape, while the overall wavefront deformation presents a concave shape in the pump area and a "donut" shape over the entire area. The latter is indicative of the increasing temperature in the periphery, caused by ASE absorption in the Cr^{4+}:YAG cladding. The interferometrically measured wavefront deformations at different pump powers show good agreement with both the finite element simulations and the focus shifts measurements. The thermal lens power corresponds to 0.007 m^{-1} for a full round-trip path through the gain medium at 1010 W average pump power. Furthermore, the OPD

is found to be dominated by the mechanical deformation of the assembly. Moreover, the thermal dynamic difference between extraction and non-extraction situation was discussed, indicating a lower maximum temperature should be observed under the seeding condition, which was proved by the temperature measurement results under a pump power up to 1.75 kW. The measurement of the temperature under 1 kHz 1.2 J give an value of 128 K, which is acceptable for both the thermal mechanical and gain requirement. This investigation of the thermal behaviors of a cryogenically-cooled Yb:YAG laser amplifier and the demonstrated ability to generate temperature maps of cryo-cooled Yb-doped gain media pumped by kilowatt average power beam will benefit the design of high-energy, high average power laser active mirror amplifiers and their further power scaling.

References

[1] W.P. Leemans, A.J. Gonsalves, H-S Mao, K. Nakamura, C. Benedetti, C.B. Schroeder, Cs Tóth, J. Daniels, D.E. Mittelberger, S.S. Bulanov, et al. Multi-GeV electron beams from capillary-discharge-guided subpetawatt laser pulses in the self-trapping regime. *Physical Review Letters*, 113(24):245002, 2014.

[2] Liang Yin, Hanchen Wang, Brendan A Reagan, Cory Baumgarten, Eric Gullikson, Mark Berrill, Vyacheslav N Shlyaptsev, and Jorge J Rocca. 6.7-nm emission from Gd and Tb plasmas over a broad range of irradiation parameters using a single laser. *Physical Review Applied*, 6(3):034009, 2016.

[3] A Azhari, S Sulaiman, and AK Prasada Rao. A review on the application of peening processes for surface treatment. In *IOP Conference Series: Materials Science and Engineering*, volume 114, page 012002. IOP Publishing, 2016.

[4] WR Meier, AM Dunne, KJ Kramer, S Reyes, TM Anklam, LIFE Team, et al. Fusion technology aspects of laser inertial fusion energy (LIFE). *Fusion Engineering and Design*, 89(9-10):2489–2492, 2014.

[5] Glen A Slack and DW Oliver. Thermal conductivity of garnets and phonon scattering by rare-earth ions. *Physical Review B*, 4(2):592, 1971.

[6] R. L. Aggarwal, D. J. Ripin, J. R. Ochoa, and T. Y. Fan. Measurement of thermo-optic properties of $Y_3Al_5O_{12}$, $Lu_3Al_5O_{12}$, $YAIO_3$, $LiYF_4$, $LiLuF_4$, BaY_2F_8, $KGd(WO_4)_2$, and $KY(WO_4)_2$ laser crystals in the 80–300 K temperature range. *Journal of Applied Physics*, 98(10):103514, 2005.

[7] Jun Dong, Michael Bass, Yanli Mao, Peizhen Deng, and Fuxi Gan. Dependence of the Yb^{3+} emission cross section and lifetime on temperature and concentration in yttrium aluminum garnet. *JOSA B*, 20(9):1975–1979, 2003.

[8] David C Brown, Rufus L Cone, Yongchen Sun, and Randy W Equall. Yb: YAG absorption at ambient and cryogenic temperatures. *IEEE Journal of selected topics in quantum electronics*, 11(3):604–612, 2005.

[9] Cory Baumgarten, Michael Pedicone, Herman Bravo, Hanchen Wang, Liang Yin, Carmen S Menoni, Jorge J Rocca, and Brendan A Reagan. 1 J, 0.5 kHz repetition rate picosecond laser. *Optics Letters*, 41(14):3339–3342, 2016.

[10] Brendan A Reagan, Cory Baumgarten, Elzbieta Jankowska, Han Chi, Herman Bravo, Kristian Dehne, Michael Pedicone, Liang Yin, Hanchen Wang, Carmen S Menoni, et al. Scaling diode-pumped, high energy picosecond lasers to kilowatt average powers. *High Power Laser Science and Engineering*, 6, 2018.

[11] Paul Mason, Martin Divokỳ, Klaus Ertel, Jan Pilař, Thomas Butcher, Martin Hanuš, Saumyabrata Banerjee, Jonathan Phillips, Jodie Smith, Mariastefania De Vido, et al. Kilowatt average power 100 J-level diode pumped solid state laser. *Optica*, 4(4):438–439, 2017.

[12] Sébastien Chénais, Frédéric Druon, Sébastien Forget, François Balembois, and Patrick Georges. On thermal effects in solid-state lasers: The case of ytterbium-doped materials. *Progress in quantum electronics*, 30(4):89–153, 2006.

[13] Daniel Albach, Geoffroy LeTouze, and Jean-Christophe Chanteloup. Deformation of partially pumped active mirrors for high average-power diode-pumped solid-state lasers. *Optics Express*, 19(9):8413–8422, 2011.

[14] Issa Tamer, Sebastian Keppler, Marco Hornung, Jörg Körner, Joachim Hein, and Malte C Kaluza. Spatio-Temporal Characterization of Pump-Induced Wavefront Aberrations in Yb^{3+}-Doped Materials. *Laser & Photonics Reviews*, 12(2):1700211, 2018.

[15] Jörg Körner, Fangxin Yue, Joachim Hein, and Malte C Kaluza. Spatially and temporally resolved temperature measurement in laser media. *Optics letters*, 41(11):2525–2528, 2016.

[16] K Ertel, S Banerjee, PD Mason, PJ Phillips, M Siebold, C Hernandez-Gomez, and JC Collier. Optimising the efficiency of pulsed diode pumped yb: Yag laser amplifiers for ns pulse generation. *Optics express*, 19(27):26610–26626, 2011.

[17] Xing Fu, Kyung-Han Hong, Li-Jin Chen, and Franz X Kärtner. Performance scaling of high-power picosecond cryogenically cooled rod-type Yb: YAG multipass amplification. *JOSA B*, 30(11):2798–2809, 2013.

[18] Ondrej Slezak, Antonio Lucianetti, Martin Divoky, Magdalena Sawicka, and Tomas Mocek. Optimization of wavefront distortions and thermal-stress induced birefringence in a cryogenically-cooled multislab laser amplifier. *IEEE Journal of Quantum Electronics*, 49(11):960–966, 2013.

[19] Han Chi, Kristian A Dehne, Cory M Baumgarten, Hanchen Wang, Liang Yin, Brendan A Reagan, and Jorge J Rocca. In situ 3-D temperature mapping of high average power cryogenic laser amplifiers. *Optics express*, 26(5):5240–5252, 2018.

[20] Anthony E Siegman. How to (maybe) measure laser beam quality. In *Diode Pumped Solid State Lasers: Applications and Issues*, page MQ1. Optical Society of America, 1998.

[21] TY Fan. Heat generation in Nd: YAG and Yb: YAG. *IEEE Journal of Quantum Electronics*, 29(6):1457–1459, 1993.

[22] Jochen Speiser. Scaling of thin-disk lasers—influence of amplified spontaneous emission. *JOSA B*, 26(1):26–35, 2009.

[23] S Kück, K Petermann, U Pohlmann, and G Huber. Near-infrared emission of Cr^{4+}-doped garnets: lifetimes, quantum efficiencies, and emission cross sections. *Physical Review B*, 51(24):17323, 1995.

[24] Magdalena Sawicka, Martin Divoky, Jakub Novak, Antonio Lucianetti, Bedrich Rus, and Tomas Mocek. Modeling of amplified spontaneous emission, heat deposition, and energy

extraction in cryogenically cooled multislab Yb^{3+}: YAG laser amplifier for the HiLASE Project. *JOSA B*, 29(6):1270–1276, 2012.

[25] OL Antipov, DV Bredikhin, ON Eremeykin, AP Savikin, EV Ivakin, and AV Sukhadolau. Electronic mechanism for refractive-index changes in intensively pumped Yb: YAG laser crystals. *Optics letters*, 31(6):763–765, 2006.

[26] Max Born and Emil Wolf. *Principles of optics: electromagnetic theory of propagation, interference and diffraction of light*. Elsevier, 2013.

Chapter 4

Demonstration of a Kilowatt Average Power, 1 J, Green Laser

In this chapter, the demonstration of a kilowatt average power, 1 kHz repetition rate, ns pulse width green laser is presented. Despite the fact that the results from Chapter 3 indicate that the main amplifier system in the 500 Hz Yb:YAG laser system could provide sufficient gain for generating pulses with >1 J energy at 1 kHz and within an acceptable temperature range, there are several challenges that must be met to achieve this goal as well as for high average power, high pulse energy, green laser generation. This includes modifications in the implementation in the seed laser, the regenerative amplifier, and the pre-amplifier stage. In section 4.2, the redesigned configurations of each subsystem of the >1 J, 1 kHz λ=1030 nm laser are described in detail along with their output performance. In addition, the demonstration of an average power up to 1.26 kW from the cryogenically cooled main amplifier stage is presented. Section 4.3 focuses on the second harmonic generation (SHG) process, where a λ=515 nm laser generating Joule-level pulses at 1 kHz repetition rate was achieved by frequency doubling the 1.2 J, 2 ns temporally shaped square pulses from a cryogenically cooled Yb:YAG laser in LBO crystals. A doubling efficiency of 78 percent resulted in 0.94 J second harmonic pulses at 1 kHz. The unconverted fundamental beam interacted with a second LBO crystal to generate >100 mJ second harmonic pulses to reach a total green average power of 1.04 kW. A conversion efficiency of 89 percent was also demonstrated for 0.58 J green pulses generation at 1 kHz with a different parameter LBO crystal. These results open the possibility to pump high energy femtosecond lasers at kHz repetition rates.

4.1 Introduction

High power green lasers play an important role in material processing [1], in optical pumping of ultrashort pulse lasers [2, 3], and in dense plasma generation [4]. The leading approach

to the generation of high energy green laser pulses is frequency doubling of 1 μm wavelength solid state lasers in a nonlinear optical crystal. However, the traditional high energy (Joule-level and beyond) λ=1 μm solid state lasers, which include Nd:glass, Nd:YAG and Nd:YLF lasers, are typically limited to relatively low repetition rate (<50 Hz) and low average power [5–7]. Future advances in new applications such as the development of compact high energy particle accelerators based on laser wakefield acceleration [8] and the scaling to high repetition rates of ultra-intense laser-matter interaction experiments for the generation of high average flux energetic photon and particle sources [9–14] require the generation of femtosecond pulses of multi-Joule energy at kHz repetition rates [3, 15–17]. However, the scaling of some of the leading technologies for the generation of ultra-intense pulses, including Ti:Sapphire and OPCPA lasers, is limited by the availability of the necessary high average power laser drivers.

An efficient scalable solution to the generation of high energy green pulses at high repetition rates is the frequency doubling of lasers based on Yb:YAG, a gain material with good optical and thermal properties [18–21]. With an upper laser level lifetime of $\sim$1 ms, Yb:YAG can be efficiently pumped with commercially available high average power semiconductor lasers. Diode-pumped Yb-doped lasers at λ=1.03 μm have been demonstrated to generate high energy pulses at high repetition rate [22–27] with cryogenically cooled Yb:YAG laser amplifiers producing 1 J pulses at repetition rates of up to 1 kHz [22–24]. Meanwhile, nonlinear optical materials such as LiB_3O_5 (LBO) have been demonstrated to yield high optical conversion efficiency into second harmonic for λ=1 μm lasers [28–32]. However, most of the progress achieved in the development of high average power green lasers based on Yb:YAG has been limited to the generation of μJ to mJ-level pulses at repetition rates ranging from hundreds of kHz to MHz [30,31]. For example, 370 W average power at λ=515 nm was achieved by the generation of 7 μJ pulses at 50 MHz repetition rate [30]. 1.4 kW average power at the same wavelength was achieved with 4.8 mJ pulses at 300 kHz repetition rate [31]. In comparison, the repetition rate and average power of lasers generating Joule-level green pulses has remained considerably lower. Second harmonic generation (SHG) in the DiPOLE laser based on a cryogenically cooled Yb:YAG laser has produced 5.6 J pulses at 10 Hz repetition rate,

an average power of 56 W [32]. However, there are no reports of Joule-level green pulse laser operation at kHz repetition rate. This chapter discusses the generation of Joule-level λ=515 nm nanosecond laser pulses at 1 kHz repetition rate. Frequency doubling of 1.2 J laser pulses from a 1 kHz repetition rate cryogenically cooled Yb:YAG laser in a Type-I phase matching LBO crystal generated 0.94 J, λ=515 nm pulses with a conversion efficiency of 78 percent. The unconverted light interacted with a second LBO crystal to generate an additional >100 mJ pulses of λ=515 nm to reach a total green average power of 1.04 kW.

4.2 Generation of 1.2 J, 1030 nm, 2 ns square pulses at 1 kHz

The kilowatt average power, 1 kHz repetition rate, λ=515 nm laser system is schematically illustrated in Figure 4.1. The system can be separated to two main parts, an infrared (IR) laser system that produces pulses (λ=1.03 μm) of 1.2 J energy at 1 kHz repetition rate which is illustrated in the upper part of Figure 4.1., and the frequency doubling module in the lower part of Figure 4.1.

4.2.1 Arbitrary Shape Laser Pulse Generation

The temporal and spatial profiles of the seed pulse play an important role in the SHG conversion efficiency. Temporally square pulses were generated to uniformly maintain the intensity impinging into the doubling crystals at the optimum value for frequency doubling. Because the temporal profile of the pulses injected into the amplifier chain is re-shaped by gain saturation as pulses are amplified to the Joule level, the seed pulses are generated by an arbitrary-waveform laser which can be programmed to generate a constant amplitude square pulse shape at the end of the amplifier chain.

A schematic of the setup used to generate seed pulses of arbitrary shape is shown in the upper part of Figure 4.1. Figure 4.2 shows the actual seed laser setup corresponding to the schematic. It comprises a 2 W peak power λ=1030 nm diode laser, an electro-optic modulator (EOM), an arbitrary waveform generator (AWG), and a processing unit. The seed laser is temperature tuned to operate at the wavelength corresponding to high gain in the following chain of Yb:YAG cryogenic

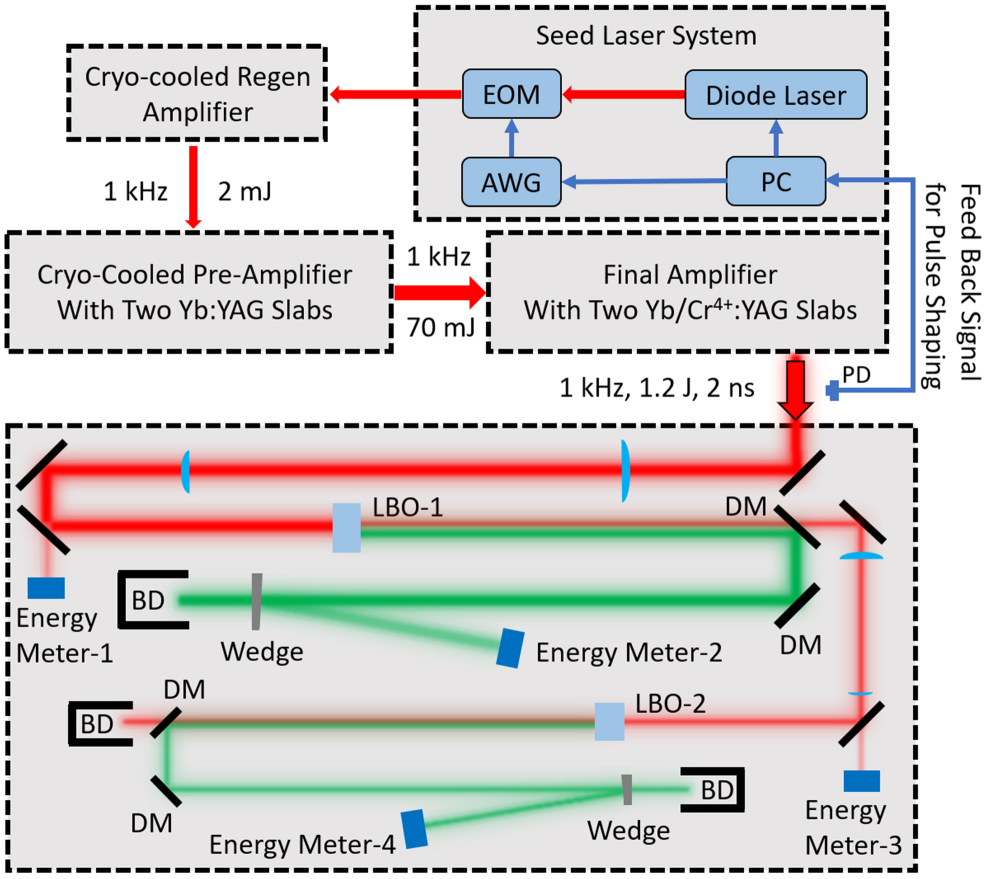

Figure 4.1: Schematic diagram of the high power λ=515 nm laser system. It includes a seed pulse laser front-end to generate pulses of arbitrary shape, a chain of diode pumped Yb:YAG cryogenic amplifiers, and two LBO second harmonic generation units. DM: dichroic mirror; BD: beam dumper; PD: photodiode.

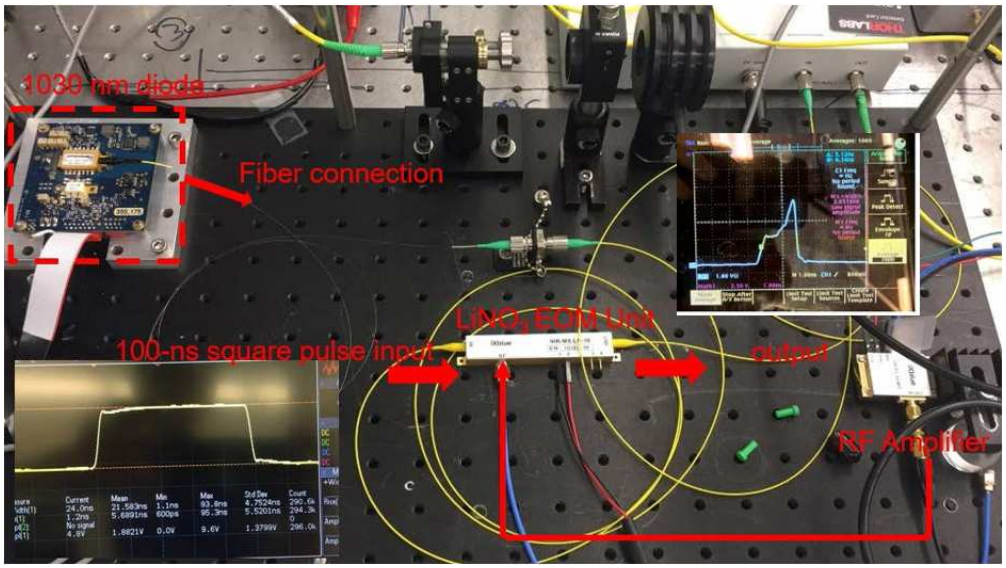

Figure 4.2: Seed laser for the generation of arbitrary shape pulses.

amplifiers. The diode laser generates rectangular pulses of 100 ns duration at a repetition rate of 300 kHz. A 10 GHz RF bandwidth EOM controlled by the 2.5 GHz AWG is subsequently used to shape the pulses into a 2 ns wide profile. The 2 ns pulse width was selected as a compromise between doubling efficiency and safe long term operation of the optics in the system, and to avoid pulse overlapping in the amplifier stages. Because the half wave voltage of the EOM is about 5 V and the AWG can only generate a maximum output voltage of 350 mV, a 10 GHz RF amplifier is employed to boost the pulse shape signal. The shaped pulses have a risetime of 200 ps, which could be made shorter if a higher RF bandwidth AWG is used. A 5 GHz photodiode is set up at the output of the Yb:YAG amplifier chain to monitor the final pulse shape and provide the feedback necessary to adjust the input signal of the program-controlled AWG. The adjusted signal is then again applied to the EOM. This feedback process keeps looping until the desired pulse shape is achieved at the output of the amplifier chain. Figure 4.3(a) shows the measured amplified 1.2 J square pulse shape, along with the temporal profile of the corresponding shaped seed pulse measured before the cryogenically cooled regenerative amplifier (Figure 4.3(b)). While only the square pulse shape relevant to SHG is presented here, more complicated pulse shapes can be generated with the same setup for other applications.

4.2.2 Cryogenically Cooled Regenerative Amplifier

The shaped seed pulses are first amplified to the mJ-level by a cryogenically cooled Yb:YAG thin disk regenerative amplifier at 1 kHz repetition rate. The advantages of using a cryogenic regenerative amplifier include more efficient heat dissipation due to the increase of the thermal conductivity of Yb:YAG at cryogenic temperature which helps to mitigate thermal effects and at the same time it results in a higher gain factor. In addition, besides matching the wavelength of the subsequent cryogenically cooled power amplifier, it lowers the saturation intensity allowing for more efficient energy extraction. Figure 4.4 shows the diagram of the cryogenic regenerative amplifier, which uses a 0.5 mm thick, 7% doped Yb:YAG active mirror. The front side of crystal is coated with a 940-1030 nm anti-reflective (AR) coating, while the back is coated with a 1030 nm

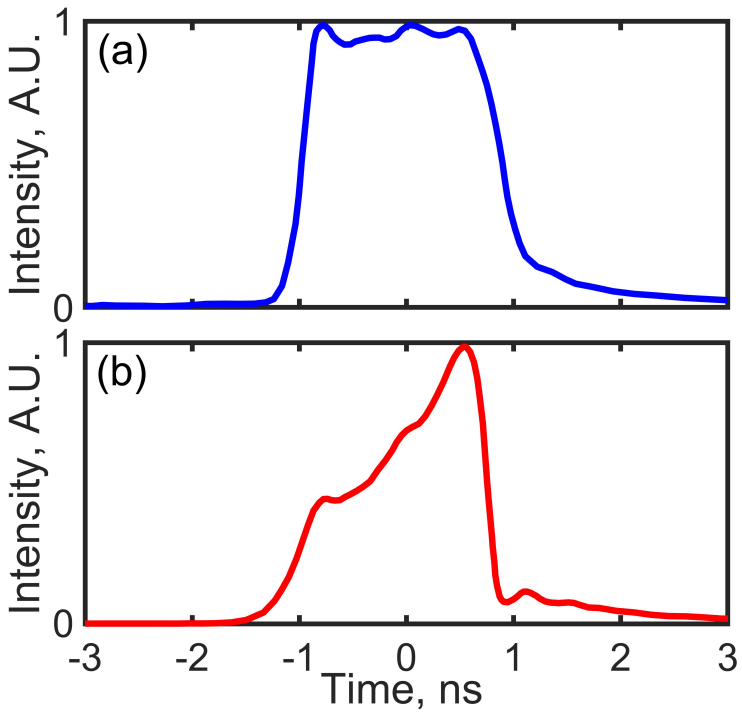

Figure 4.3: Temporal profile of (a) output pulse from the final amplifier and (b) the seed pulse measured before the regenerative amplifier.

high reflective coating. The crystal was soldered to a copper tungsten (CuW) heatsink mounted on a cold finger, which is in contact with liquid nitrogen (LN2). The assembly is mounted in a vacuum chamber to avoid water condensation. The plano-concave cavity is designed to achieve a stable operation and to allow for 2 passes through the gain medium per round trip. A fiber-coupled 200 W maximum CW power 940 nm wavelength diode laser was used as the pump. The output from a 400-µm core diameter fiber was imaged with a telescope onto the gain crystal to form a 1 mm diameter beam. The pump pulse duration is optimized to 450 µs at 1 kHz repetition rate. After 30 round trips in the cavity, a 3 mJ pulse is achieved and kicked out of the cavity by an inner cavity quarter voltage Pockels cell. Another Pockels cell and a pair of crossed polarizers is placed at the exit of the regenerative amplifier cavity to improve the pulse contrast before further amplification.

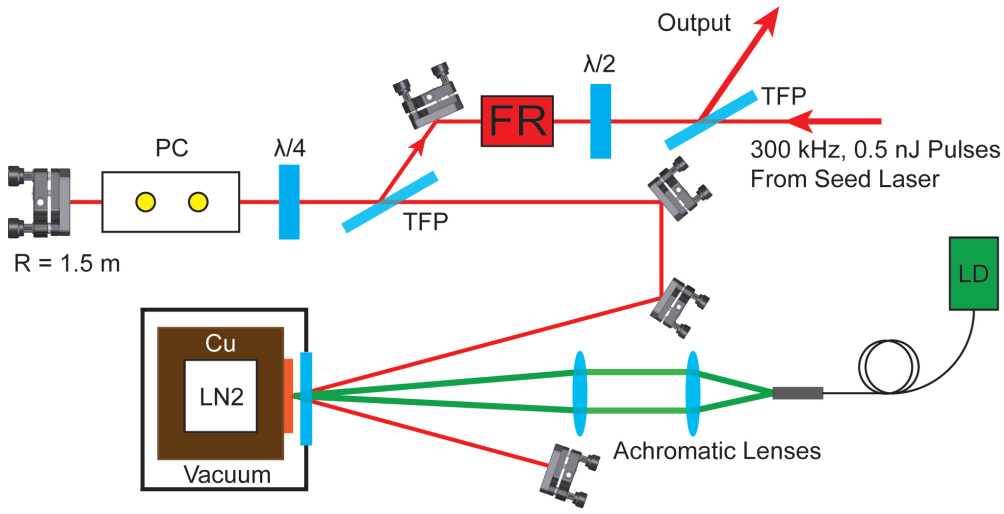

Figure 4.4: Schematic of cryogenically cooled regenerative amplifier. TFP: thin film polarizer; PC: Pockels Cell; FR: Faraday rotator

4.2.3 Cryogenically Cooled Pre-Amplifier Stage

After exiting the laser front-end, the millijoule-level pulses are injected into a cryogenically cooled Yb:YAG pre-amplifier where they are amplified to about 100 mJ. An schematic of the pre-amplifier is shown in Figure 4.5. It comprises two active mirrors based on 5 mm thick 2%-at Yb:YAG crystals. The number of active mirrors in this pre-amp was increased to two with respect to a previous 500 Hz design [22] to manage the dissipation of the thermal load. A total of 7 passes achieves the desired amplification to 100 mJ pulse energy at 1 kHz repetition rate which is necessary for efficient energy extraction from the subsequent main amplifier stage. Both crystals are mounted into a single evacuated chamber where their back surfaces are directly cooled by flowing liquid nitrogen. The first active mirror is pumped by imaging the output of a 400 W, λ=940 nm wavelength fiber coupled diode laser into a 4 mm diameter spot with an achromatic lens. The pump pulses are 450 µs in duration. The laser pulses are amplified in five passes through the first crystal (where one pass is defined as the laser pulse traversing the gain medium twice after reflecting from the HR coating), and are subsequently further amplified in two passes through the second active mirror. The second Yb:YAG active mirror is pumped into a similar spot by two 400 W, 940 nm fiber coupled laser diodes. The pump pulse duration is set at 450 µs as well. The

100 mJ pulses are passed through an 8 mm diameter serrated aperture (SA) to achieve a nearly flat-top beam profile. A Faraday rotator and a pair of polarizers are used to mitigate feedback from the subsequent main amplifier.

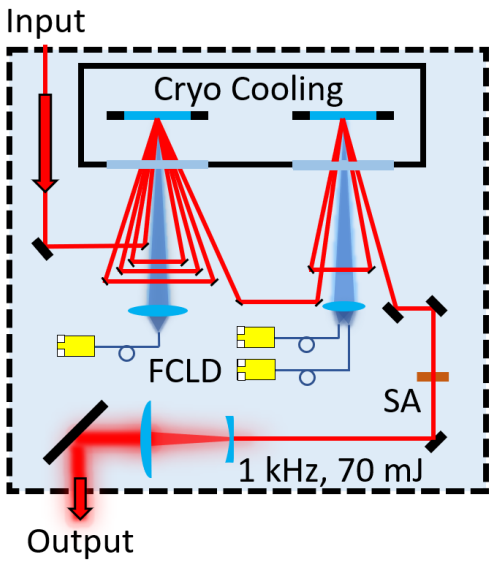

Figure 4.5: Schematic of cryogenically cooled pre-amplifier. FCLD: fiber coupled laser diode; SA: serrated aperture.

4.2.4 Cryogenically Cooled Main Amplifier

The pulses from the pre-amplification stage are used to seed the final power amplifier, which consists of a compact evacuated chamber containing two active mirror Yb:YAG slabs cooled by flowing liquid nitrogen with an automated system. The active mirror slab is composed of a 2 mm thick $30\times30\,\mathrm{mm}^2$, 3%-at Yb:YAG slab, surrounded by a 10 mm wide Cr^{4+}:YAG cladding for mitigating amplified spontaneous emission (ASE) and parasitic lasing. A 3 mm thick undoped YAG cap is bonded on the front surface of this Yb/Cr^{4+}:YAG assembly to reduce ASE, assist in dissipating heat, and increase structural integrity. The front and back surfaces are coated with a broadband 940-1030 nm anti-reflection (AR) and a high reflection (HR) coating, respectively. Each slab is pumped by a λ=940 nm, 6 kW peak power, 60 bar laser diode array. The pump diodes generate 380 µs duration pulses at 1 kHz that are shaped to form nearly flat-top 16 mm diameter

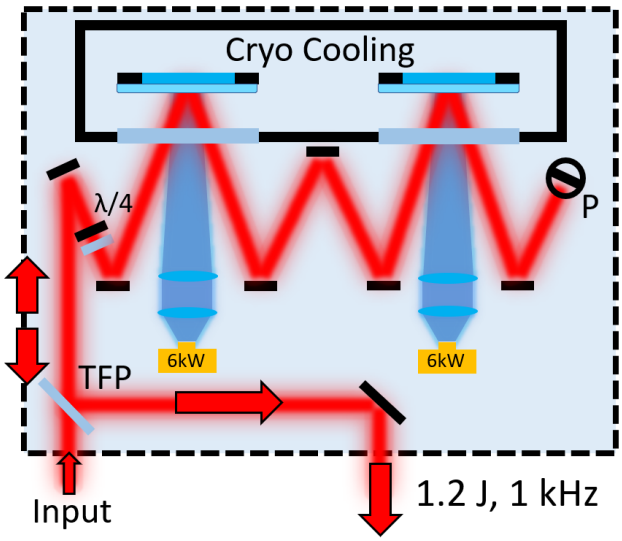

Figure 4.6: Schematic of cryogenically cooled main power amplifier. TFP: thin film polarizer.

pump spots onto each slab. A spherical mirror is used to image back the unabsorbed pump laser onto the active region, which results in more than 90% absorption of the total pump power, while avoiding an increased doping concentration that would reduce the thermal conductivity of Yb:YAG at cryogenic temperatures [19]. This final amplifier is seeded with 70 mJ pulses from the pre-amplifier stage that are injected through a thin film polarizer (TFP). After the seed pulses pass twice through the each of the active mirrors, a periscope is used to spatially rotate the beam 90 degrees and change its height. The beam is sent back to the two active mirrors for a third and fourth pass. After the first four passes a quarter waveplate combined with a 0-degree HR mirror rotates the polarization 90 degrees, sending the beam back through the same path to the TFP to exit the amplifier.

Figure 4.7 shows the measured output pulse energy at 1 kHz repetition rate as a function of the final amplifier total pump energy. A maximum 1.26 J pulse energy (1.26 kW average power) was obtained with a total pump pulse energy of 3.5 J incident on the Yb:YAG slabs. The optical-to-optical conversion efficiency is about 36%. The 1.2 kW average power output beam has a uniform flat-top beam profile. The beam is characterized by a measured M^2=1.32 and 1.39 on the horizontal and vertical directions, respectively (Figure 4.8).

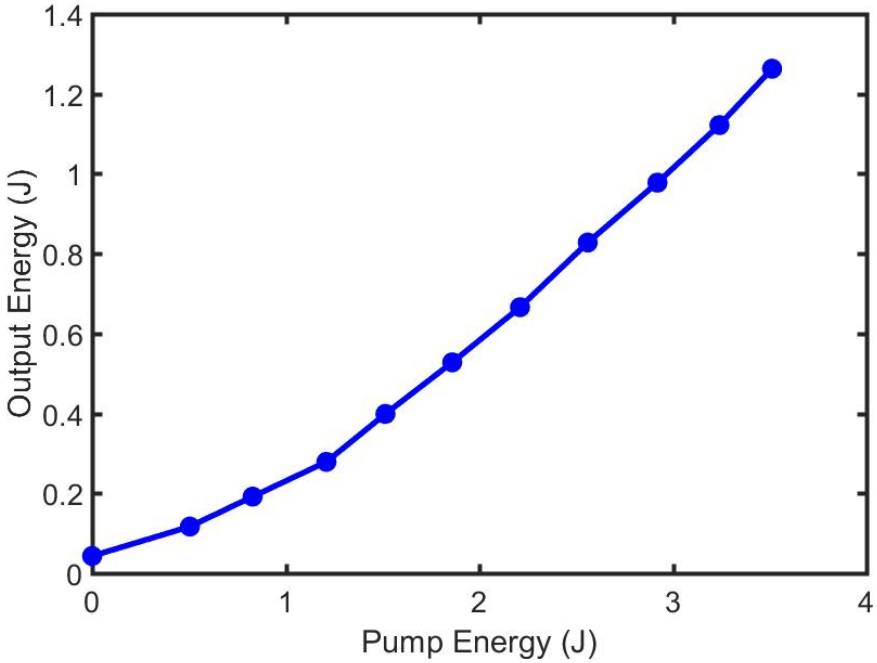

Figure 4.7: Laser pulse energy measured at the exit of the final amplifier as a function of total pump energy at 1 kHz repetition rate. A maximum energy of 1.26 J was obtained with a total pump energy of 3.5 J.

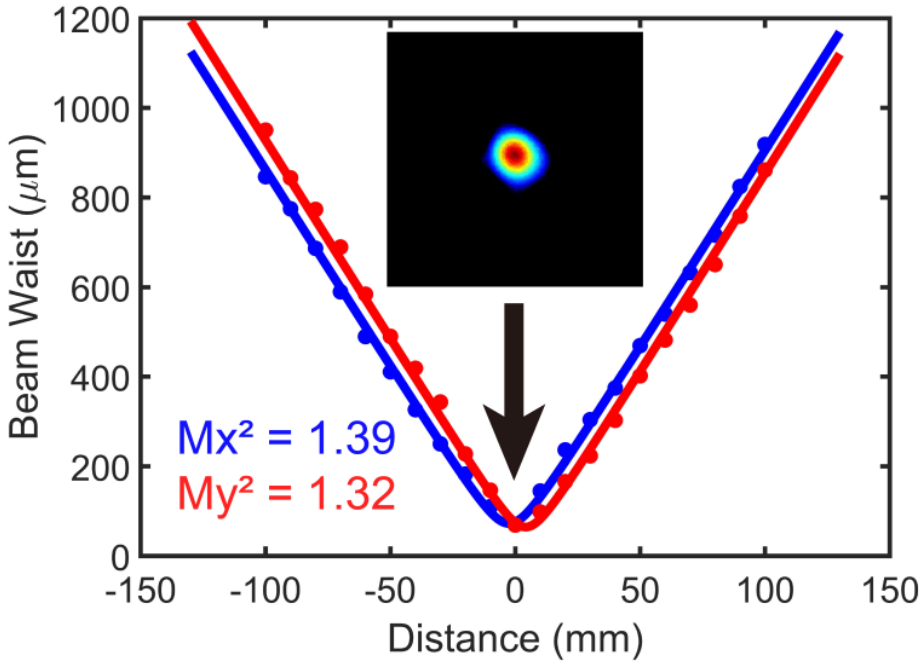

Figure 4.8: M^2 measurement of the beam quality of the 1.2 J pulses at 1 kHz repetition rate. The inset image shows the far field beam profile at focus.

4.3 Demonstration of a kilowatt average power, 1 J, green laser

4.3.1 SHG Experimental Setup

The SHG setup is placed at the output of the final amplification stage. Type-I phase matching in LBO crystals cut at θ=90° and φ=13.6° were used to upconvert the λ=1030 nm pulses into λ=515 nm light. To make the most efficient use of the fundamental beam, two LBO crystals were set up in series as shown in Figure 4.1. The absorption coefficient of the material is lower than 10 ppm/cm. Anti-reflection (AR) coatings at λ=515 nm and λ=1030 nm were deposited on both crystal surfaces, and the crystals were mounted on temperature controlled copper holders, with the temperature set to 300 K. A Keplerian telescope was used to image the output of the final stage of the Yb:YAG amplifier chain with selected demagnification onto the first 30 mm diameter, 13 mm thick, LBO crystal. The energy of the impinging IR pulse is measured using the calibrated leak from a mirror placed before the crystal. The second harmonic light is separated from the fundamental by a sequence of two dichroic mirrors. An imaging camera system is setup after the second dichroic mirror to monitor the beam profile at the output surface of the LBO crystal. The beam reflected from an AR coated wedge is used to measure the energy of λ=515 nm pulses. The unconverted λ=1030 nm beam is imaged into the second LBO crystal ($10\times10\times14$ mm^3) by a Keplerian telescope placed after the first dichroic mirror. The rest of the components after the second LBO crystal are similar to those after the first SHG stage.

4.3.2 SHG Experimental Results

Figure 4.9 shows the λ=515 nm laser pulse energy and SHG conversion efficiency as a function of IR pulse energy obtained with the 13 mm thick LBO crystal for a 14 mm diameter beam with a fluence of up to 0.78 J/cm^2. The pulse energy reaches 0.94 J, corresponding to an average power of 940 W and a conversion efficiency 78 percent. At the highest fluence the conversion efficiency curve shows signs of saturation. Figure 4.10 shows the shot-to-shot energy variation for 125,000 consecutive shots at 1 kHz repetition rate. The standard deviation of the λ=1030 nm pulse and λ=515 nm pulse energy is 1.4% and 2.4%, respectively. Runs over 10-30 minutes of uninterrupted

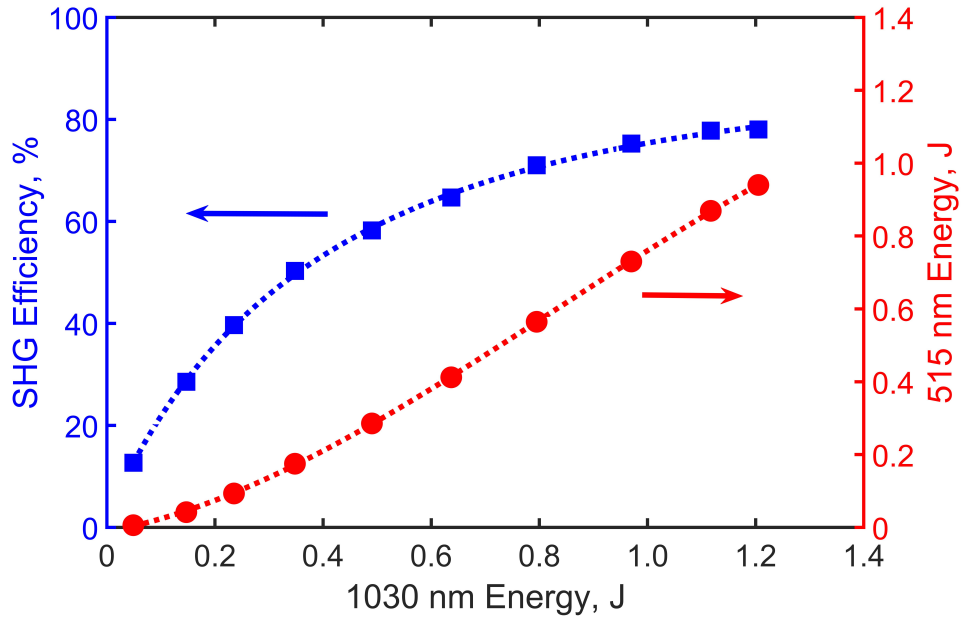

Figure 4.9: SHG efficiency (blue) and SHG output energy (red) vs. fundamental pulse energy obtained with a 13 mm thick LBO crystal at 1 kHz repetition rate.

operation at total green pulse energies up to 0.85 J at 1 kHz repetition rate show energy standard deviations within 2.9%. A further decrease on standard deviation of both fundamental and SHG energy could be achieved by upgrading the seed diode laser to a single or few frequency mode(s) diode laser with a spectrum bandwidth lower than the gain bandwidth of cryogenically cooled Yb:YAG.

The unconverted fundamental beam was upconverted in the second LBO crystal. A 7 mm diameter beam of >200 mJ pulse energy was used to achieve a fundamental fluence of $\sim$0.5 J/cm^2 on the crystal, resulting in $\sim$50% conversion efficiency and in the generation of an additional >100 mJ pulses at λ=515 nm. The resulting total λ=515 nm average power reached 1.04 kW (1.04 J pulses at 1 kHz repetition rate). The λ=515 nm beam quality depends mainly on the quality of the fundamental beam. The measurements show that a uniform fundamental beam profile [24] leads to a second harmonic beam with good intensity uniformity and similar M^2. Figure 4.11(a) and Figure 4.11(b) show that both the λ=515 nm, 0.94 J and the secondary 100 mJ beams display

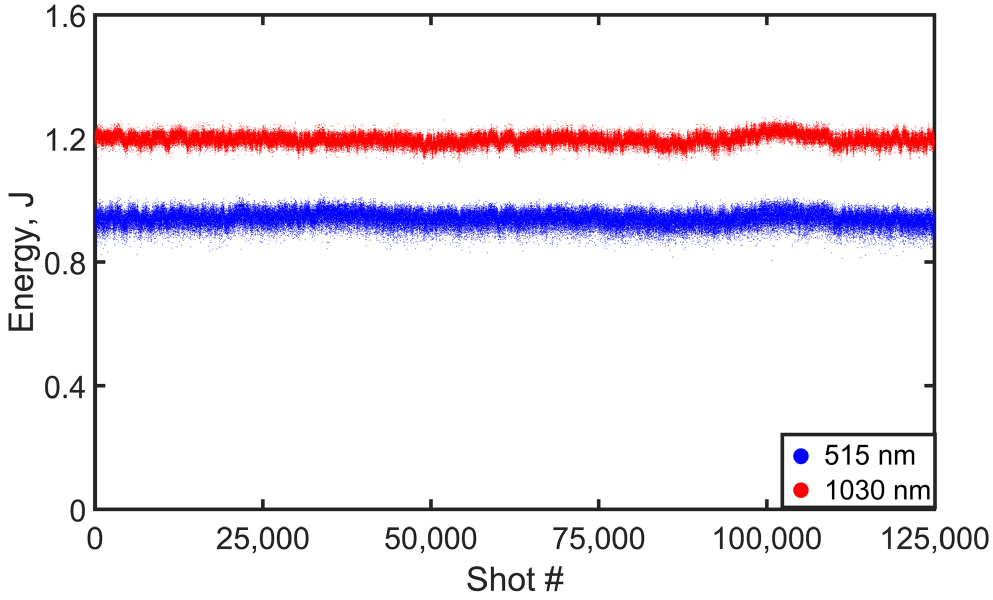

Figure 4.10: Measured shot-to-shot energy variation of the fundamental (red) and second harmonic (blue) pulses for 125,000 consecutive shots at 1 kHz repetition rate.

relatively flat-top profiles with good uniformity. The second harmonic beam is characterized by a measured M^2=1.40 and 1.32 on the horizontal and vertical directions respectively (Figure 4.11(c)).

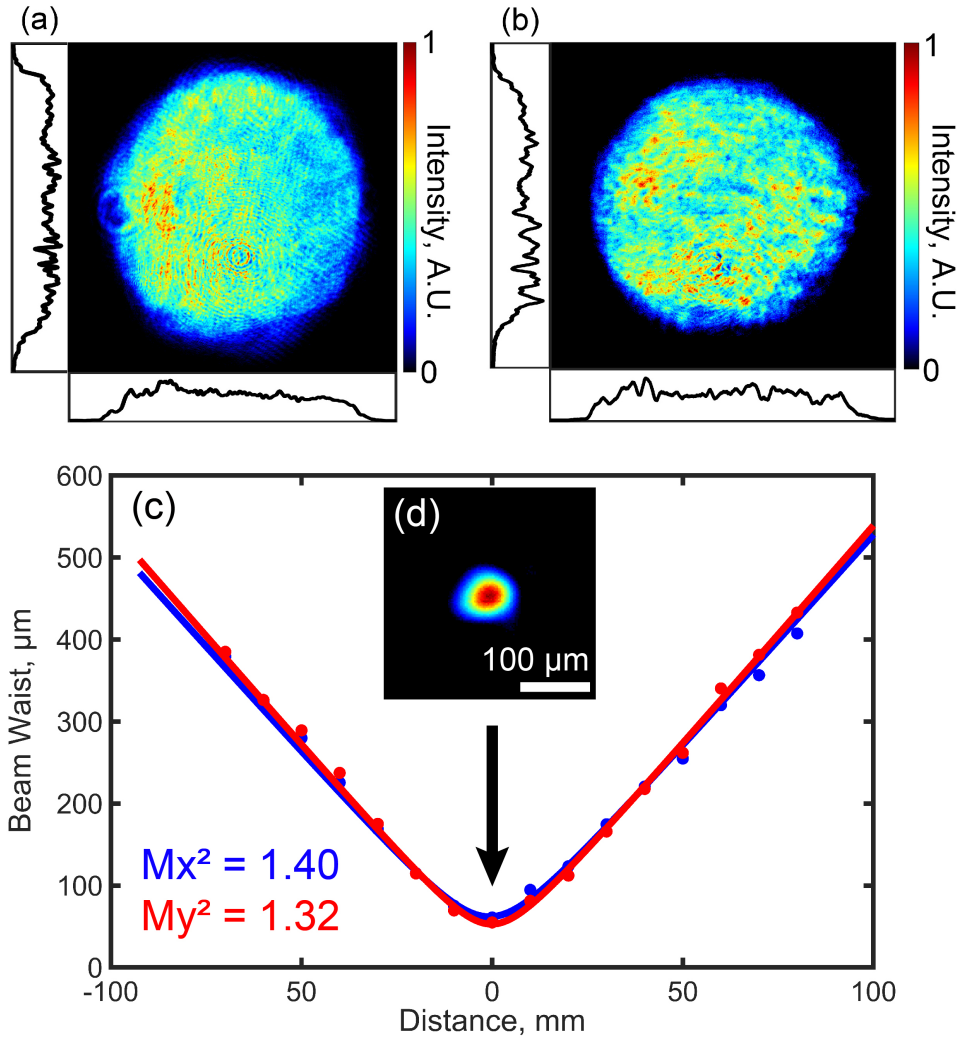

Figure 4.11: Beam profile of the λ=515 nm (a) 0.94 J, pulse beam and (b) the secondary 100 mJ SHG beam at 1 kHz repetition rate; (c) M^2 measurement of the λ=515 nm primary beam with (d) the beam profile at focal spot.

To further investigate the optimal parameters for efficient doubling of high energy pulses at 1 kHz repetition rate, a 10 mm thick LBO crystal was also tested. Because of the shorter crystal length, a higher fluence was applied for which 0.65 J fundamental wavelength pulses were down sized to about 10 mm diameter, corresponding to a fluence of 0.83 J/cm^2. As shown in Figure 4.12, this resulted in the generation of 0.58 J pulses at λ=515 nm at 1 kHz repetition rate, corresponding to a doubling efficiency of 89%. The doubling efficiency showed signs of saturation when the fundamental fluence was further increased. To use a larger fraction of the λ=1030 nm pulse energy

available at 1 kHz, the beam diameter was increased to 12 mm. SHG pulses of 0.74 J energy were generate at an average power of 740 W with a conversion efficiency of ∼74%, which is lower than the value achieved with the 13 mm thick crystal.

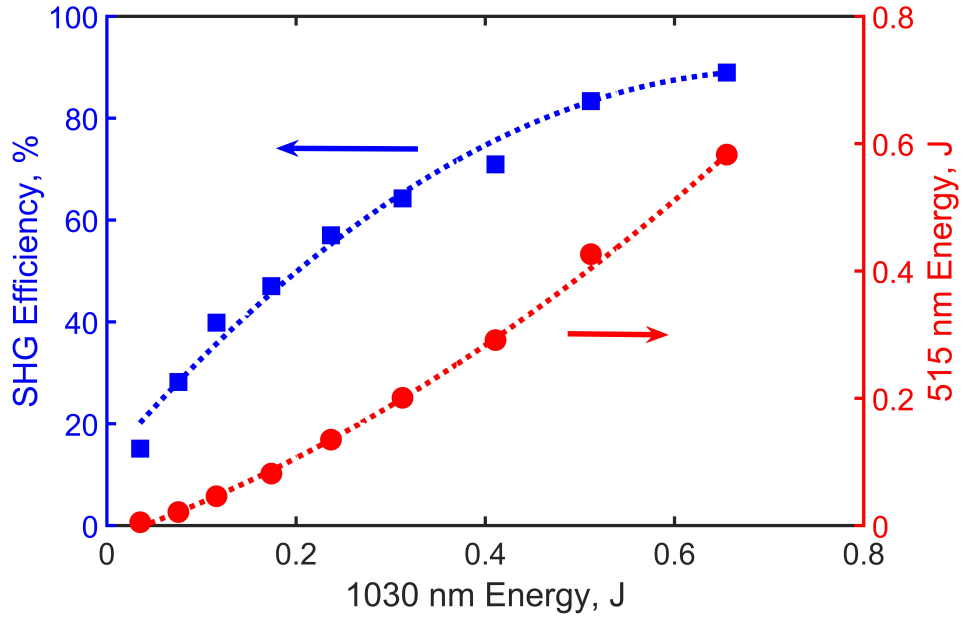

Figure 4.12: SHG efficiency (blue) and SHG output energy (red) vs. fundamental energy obtained with a 10 mm thick LBO crystal at 1 kHz repetition rate.

4.4 Conclusion

In this chapter, we have demonstrated the generation of >1.2 J, λ=1030 nm laser pulse with a square pulse shape operating at 1 kHz repetition rate by a cryogenically cooled Yb:YAG laser, and the generation of Joule-level λ=515 nm laser pulses of nanosecond duration at 1 kHz repetition rate by frequency doubling the output from the above laser in LBO with 78 percent conversion efficiency. The measured 1.04 kW average power is to our knowledge the highest average power reported for Joule-level green lasers. A higher SHG conversion efficiency of 89 percent was also achieved for 0.65 J fundamental pulses using a shorter crystal. These results will enable the generation of high energy laser pulses of femtosecond duration at 1 kHz repetition rate. In addition, the

generation of Joule-level nanosecond pulses of arbitrary shape from the kilowatt average power Yb:YAG laser system has the potential to benefit other applications such as the generation of tailored plasmas for extreme ultraviolet generation.

References

[1] J Dutta Majumdar and I Manna. Laser material processing. *International materials reviews*, 56(5-6):341–388, 2011.

[2] Xiaoming Zeng, Kainan Zhou, Yanlei Zuo, Qihua Zhu, Jingqin Su, Xiao Wang, Xiaodong Wang, Xiaojun Huang, Xuejun Jiang, Dongbin Jiang, et al. Multi-petawatt laser facility fully based on optical parametric chirped-pulse amplification. *Optics letters*, 42(10):2014–2017, 2017.

[3] Colin N Danson, Constantin Haefner, Jake Bromage, Thomas Butcher, Jean-Christophe F Chanteloup, Enam A Chowdhury, Almantas Galvanauskas, Leonida A Gizzi, Joachim Hein, David I Hillier, et al. Petawatt and exawatt class lasers worldwide. *High Power Laser Science and Engineering*, 7, 2019.

[4] Z Jiang, JC Kieffer, JP Matte, M Chaker, O Peyrusse, D Gilles, G Korn, A Maksimchuk, S Coe, and G Mourou. X-ray spectroscopy of hot solid density plasmas produced by subpicosecond high contrast laser pulses at 1018-1019 w/cm2. *Physics of Plasmas*, 2(5):1702–1711, 1995.

[5] Spectra-Physics Quanta-Ray Pro Series. https://www.spectra-physics.com/.

[6] Takashi Sekine, Hiroshi Sakai, Yasuki Takeuchi, Yuma Hatano, Toshiyuki Kawashima, Hirofumi Kan, Junji Kawanaka, Noriaki Miyanaga, and Takayoshi Norimatsu. High efficiency 12.5 J second-harmonic generation from CsLiB6O10 nonlinear crystal by diode-pumped Nd:glass laser. *Opt. Express*, 21(7):8393–8400, Apr 2013.

[7] A. J Bayramian, R. J Beach, C Bibeau, R Campbell, CA Ebbers, BL Freitas, R Kent, D Van Lue, Z Liao, T Ladran, et al. High average power frequency conversion on the Mercury laser. In *Advanced Solid-State Photonics*, page MB1. Optical Society of America, 2006.

[8] A. J Gonsalves, K Nakamura, J Daniels, C Benedetti, C Pieronek, TCH De Raadt, S Steinke, JH Bin, SS Bulanov, J Van Tilborg, et al. Petawatt laser guiding and electron beam accel-

eration to 8 gev in a laser-heated capillary discharge waveguide. *Physical Review Letters*, 122(8):084801, 2019.

[9] D Guénot, D Gustas, A Vernier, B Beaurepaire, F Böhle, M Bocoum, M Lozano, Aurélie Jullien, R Lopez-Martens, Agustin Lifschitz, et al. Relativistic electron beams driven by khz single-cycle light pulses. *Nature Photonics*, 11(5):293–296, 2017.

[10] Matteo Passoni, FM Arioli, L Cialfi, D Dellasega, L Fedeli, A Formenti, AC Giovannelli, A Maffini, F Mirani, A Pazzaglia, et al. Advanced laser-driven ion sources and their applications in materials and nuclear science. *Plasma Physics and Controlled Fusion*, 62(1):014022, 2019.

[11] J Alvarez, J Fernández-Tobias, K Mima, S Nakai, S Kar, Y Kato, and JM Perlado. Laser driven neutron sources: characteristics, applications and prospects. *Physics Procedia*, 60:29–38, 2014.

[12] Alden Curtis, Chase Calvi, James Tinsley, Reed Hollinger, Vural Kaymak, Alexander Pukhov, Shoujun Wang, Alex Rockwood, Yong Wang, Vyacheslav N Shlyaptsev, et al. Micro-scale fusion in dense relativistic nanowire array plasmas. *Nature Communications*, 9(1):1–7, 2018.

[13] H. X Chang, B Qiao, T. W Huang, Z Xu, C. T Zhou, Y. Q Gu, X. Q Yan, M Zepf, and X. T He. Brilliant petawatt gamma-ray pulse generation in quantum electrodynamic laser-plasma interaction. *Scientific Reports*, 7:45031, 2017.

[14] Reed Hollinger, Clayton Bargsten, Vyacheslav N. Shlyaptsev, Vural Kaymak, Alexander Pukhov, Maria Gabriela Capeluto, Shoujun Wang, Alex Rockwood, Yong Wang, Amanda Townsend, Amy Prieto, Patrick Stockton, Alden Curtis, and Jorge J. Rocca. Efficient picosecond x-ray pulse generation from plasmas in the radiation dominated regime. *Optica*, 4(11):1344–1349, Nov 2017.

[15] Yong Wang, Shoujun Wang, Alex Rockwood, Bradley M Luther, Reed Hollinger, Alden Curtis, Chase Calvi, Carmen S Menoni, and Jorge J Rocca. 0.85 pw laser operation at 3.3 hz and high-contrast ultrahigh-intensity λ= 400 nm second-harmonic beamline. *Optics Letters*, 42(19):3828–3831, 2017.

[16] Kei Nakamura, Hann-Shin Mao, Anthony J Gonsalves, Henri Vincenti, Daniel E Mittelberger, Joost Daniels, Arturo Magana, Csaba Toth, and Wim P Leemans. Diagnostics, control and performance parameters for the bella high repetition rate petawatt class laser. *IEEE Journal of Quantum Electronics*, 53(4):1–21, 2017.

[17] E Sistrunk, T Spinka, A Bayramian, S Betts, R Bopp, S Buck, K Charron, J Cupal, R Deri, M Drouin, et al. All diode-pumped, high-repetition-rate advanced petawatt laser system (HAPLS). In *CLEO: Science and Innovations*, pages STh1L–2. Optical Society of America, 2017.

[18] Glen A Slack and DW Oliver. Thermal conductivity of garnets and phonon scattering by rare-earth ions. *Physical Review B*, 4(2):592, 1971.

[19] RL Aggarwal, DJ Ripin, JR Ochoa, and TY Fan. Measurement of thermo-optic properties of $Y_3Al_5O_{12}$, $Lu_3Al_5O_{12}$, $YAlO_3$, $LiYF_4$, $LiLuF_4$, BaY_2F_8, $KGd(WO_4)_2$, and $KY(WO_4)_2$ laser crystals in the 80-300 K temperature range. *Journal of Applied Physics*, 98(10):103514, 2005.

[20] Jun Dong, Michael Bass, Yanli Mao, Peizhen Deng, and Fuxi Gan. Dependence of the yb3+ emission cross section and lifetime on temperature and concentration in yttrium aluminum garnet. *JOSA B*, 20(9):1975–1979, 2003.

[21] David C Brown, Rufus L Cone, Yongchen Sun, and Randy W Equall. Yb: YAG absorption at ambient and cryogenic temperatures. *IEEE Journal of Selected Topics in Quantum Electronics*, 11(3):604–612, 2005.

[22] Cory Baumgarten, Michael Pedicone, Herman Bravo, Hanchen Wang, Liang Yin, Carmen S Menoni, Jorge J Rocca, and Brendan A Reagan. 1 J, 0.5 kHz repetition rate picosecond laser. *Optics Letters*, 41(14):3339–3342, 2016.

[23] Brendan A Reagan, Cory Baumgarten, Elzbieta Jankowska, Han Chi, Herman Bravo, Kristian Dehne, Michael Pedicone, Liang Yin, Hanchen Wang, Carmen S Menoni, and Jorge J. Rocca. Scaling diode-pumped, high energy picosecond lasers to kilowatt average powers. *High Power Laser Science and Engineering*, 6, 2018.

[24] Yong Wang, Han Chi, Cory Baumgarten, Alexander R. Meadows, Kristian Dehne, Brendan A. Reagan, Aaron Davenport, Gabriel Murray, Carmen S. Menoni, and Jorge J. Rocca. 1.1 j, 1 khz repetition rate, yb:yag picosecond laser. *Optics Letters*, to be published.

[25] Paul Mason, Martin Divokỳ, Klaus Ertel, Jan Pilař, Thomas Butcher, Martin Hanuš, Saumyabrata Banerjee, Jonathan Phillips, Jodie Smith, Mariastefania De Vido, et al. Kilowatt average power 100 j-level diode pumped solid state laser. *Optica*, 4(4):438–439, 2017.

[26] S Petit, C Feral, MC Nadeau, Ph Balcou, J Brandam, D Descamps, J Lhermite, and D Marion. Towards a kW-class picosecond laser at 1 kHz. In *The European Conference on Lasers and Electro-Optics*, page ca_8_6. Optical Society of America, 2019.

[27] Luis E Zapata, Simon Schweisthal, Jelto Thesinga, Collette Zapata, Matthias Schust, Liu Yizhou, Mikhail Pergament, and Franz X Kaertner. Joule-class 500 Hz cryogenic Yb:YAG chirped pulse amplifier. In *CLEO: Science and Innovations*, pages SM4E–1. Optical Society of America, 2019.

[28] Chuangtian Chen, Yicheng Wu, Aidong Jiang, Bochang Wu, Guiming You, Rukang Li, and Shujie Lin. New nonlinear-optical crystal: Lib3o5. *JOSA B*, 6(4):616–621, 1989.

[29] T Ukachi, RJ Lane, WR Bosenberg, and CL Tang. Measurements of noncritically phase-matched second-harmonic generation in a lib3o5 crystal. *Applied Physics Letters*, 57(10):980–982, 1990.

[30] Bastian Gronloh, Peter Russbueldt, Waldemar Schneider, Bernd Jungbluth, and Hans-Dieter Hoffmann. High average power sub-picosecond pulse generation at 515 nm by extracavity frequency doubling of a mode-locked innoslab MOPA. In *Solid State Lasers Xxi: Technology and Devices*, volume 8235, page 82351C. International Society for Optics and Photonics, 2012.

[31] Christoph Röcker, André Loescher, Florian Bienert, Philippe Villeval, Dominique Lupinski, Dominik Bauer, Alexander Killi, Thomas Graf, and Marwan Abdou Ahmed. Ultrafast green thin-disk laser exceeding 1.4 kw of average power. *Optics Letters*, 45(19):5522–5525, Oct 2020.

[32] Jonathan P Phillips, Saumyabrata Banerjee, Jodie Smith, Mike Fitton, Tristan Davenne, Klaus Ertel, Paul Mason, Thomas Butcher, Mariastefania De Vido, Justin Greenhalgh, et al. High energy, high repetition rate, second harmonic generation in large aperture dkdp, ycob, and lbo crystals. *Optics Express*, 24(17):19682–19694, 2016.

Chapter 5

The Design of High Power High Energy Ultrafast Laser System

5.1 Introduction

In previous chapters, I presented the results of the generation of high energy λ = 1.03 μm pulses at 1 kHz repetition rate and the subsequent second harmonic generation (SHG) based on LBO crystals which achieved the joule-level nanosecond green pulses at up to 1 kHz repetition rate. The results provide the capability of pumping ultrafast laser amplifiers to generate pulses with hundreds of millijoule energy at 1 kHz repetition rate. However, there are still several crucial challenges in the design of high repetition rate high energy Ti:Sapphire amplifiers. The main challenge is to manage the thermal loads generated in the amplification process due to the high quantum defect of Ti:Sapphire.

In this chapter, the design of the high energy Ti:Sapphire laser system for high repetition rates is presented. A chirped pulse amplification (CPA) system with two-stage room-temperature multi-pass Ti:Sapphire amplifier sequence is proposed. Uncompressed λ = 800 nm pulses with 300 mJ pulse energy at the output of the amplifier system were designed to be generated at up to 1 kHz repetition rate. With a measured overall 70% transmission efficiency gold grating pair compressor, the system has the potential of delivering 210 mJ compressed pulses with 50 fs duration. With additional spectral compensation components, the <30 fs pulse duration could be obtained, which corresponds to a peak power of 10 TW level. In Section 5.2, the concept and the design of the cross-thin slab (XTS) Ti:Sapphire geometry are proposed for managing the thermal effects during the amplification process in a sequence of two room-temperature amplifiers. Section 5.3 discusses the gain factors in both amplifiers with different seeding energies and resulted output energies based on the design of the amplifiers. It is shown that 300 mJ output pulse energy could be achieved with

100 mJ and 700 mJ pump energy in green for the two amplifiers, respectively. Section 5.4 describes the design of water-cooled crystal mounts and the thermal distribution of Ti:Sapphire crystals at 1 kHz repetition rate in both amplifier stages. The finite element method (FEM) simulations show that the temperature distributions inside the Ti:Sapphire crystals are within the acceptable range. The calculation of the thermal lens focal lengths in both the 1st and 2nd amplifier stages is also presented, which shows that although the small temperature gradients are achieved in the Ti:Sapphire crystals, It is necessary to design thermal lensing compensation for both amplifiers. In Section 5.5, the schematic diagram of the whole high power high energy ultrafast laser system is described and discussed with the first results of the system performance.

5.2 Design of the Cross-Thin Slab Geometry for Ti:Sapphire Amplifier

The traditional design of Ti:Sapphire crystal for high energy low repetition rate ultrafast CPA laser uses the geometry of a thick disk or rod [1], which offers a sufficient amplification path length with a relatively simple multi-pass seed-pump geometry but is non-optimal for thermal load dissipation. Since the saturation fluence does not vary with the repetition rate, the heat density in the laser crystal increases proportionally with the increased repetition rate. As a result, the thermal load in the case of high energy amplifier is more severe at high repetition rate. Without sufficient heat dissipation, several consequences follow. First of all, the crystal temperature will be high. This leads to the reduction of gain factors in the amplification process that is caused by the decreased emission cross-section coefficient as well as the rise of thermo-mechanical problems [2]. Secondly, the thermal gradient inside the laser crystal will be large, which could result in severe thermal lens in a multi-pass amplification geometry. Consequently, the design of Ti:Sapphire crystal geometry for the high average power generation has to take both the gain and thermal factors into account.

Here, we describe a high energy high repetition rate Ti:Sapphire amplifier, utilizing a recently proposed crystal design with cross-thin slab (XTS) geometry [3], as shown in Figure 5.1. Contrary to the traditional rod geometry, the XTS geometry is focused on maximizing heat dissipation while

keeping the overlap volume between the seed and pump beams. The two largest surfaces on top and bottom are used to extract the heat from the crystal induced by the pump. Meanwhile, the four lateral surfaces of the XTS geometry crystal are designed to be used for pumping and seeding. AR coatings or Brewster angles could be applied to them. In this way, not only the good extraction efficiency can be achieved by the overlap of the pump and seed beams, but also a larger cooling capacity could be satisfied. The system complexity of using this XTS geometry design will be slightly higher than the traditional rod geometry amplifier, but the overall system complexity will be reduced with the room temperature operation rather than a cryogenic cooling design.

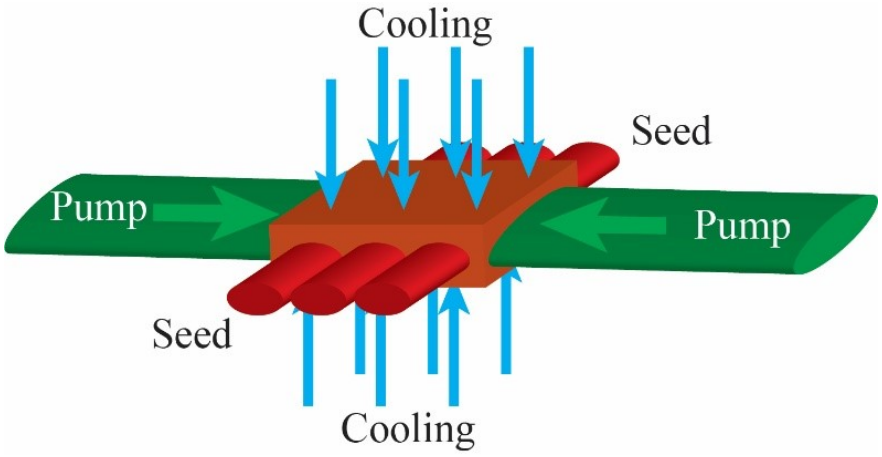

Figure 5.1: Illustration of cross-thin slab (XTS) Ti:Sapphire geometry.

In general, a higher seeding fluence leads to a higher extraction efficiency in an amplification process without reaching the gain saturation [4]. As a result, to increase the extraction rate on the Ti:Sapphire system, a two-stage XTS-amplifier scheme was designed to boost the pulse energy from the level of a few mJ to 300 mJ. Considering the gain factor, the seed-pump overlap, and the thermal management for 1 kHz repetition rate operation, the designed crystal dimension for the 1st and 2nd stage amplifiers is $10\times10\times4\,\text{mm}^3$ and $20\times30\times4\,\text{mm}^3$, respectively. The pump beam is separated into two parts by a 50:50 beam splitter to pump the crystal from both sides with oval beam shapes, as shown in Figure 5.1. The seed beam is designed to pass through the gain area six to eight times to extract the stored energy. The two $10\times10\,\text{mm}^2$ and $20\times30\,\text{mm}^2$ surfaces of the

1st and 2nd stage crystals are used to dissipate the heat, which means a total cooling area of 2 cm^2 and 12 cm^2 can be achieved for the 1st and 2nd stage crystals, respectively.

In the following sections, the gain calculation and thermal simulation results for both the 1st and 2nd amplifier will be presented and discussed. The results provide strong evidence that the two XTS Ti:Sapphire amplifiers could achieve the pulse energy of 300 mJ at up to 1 kHz repetition rate operation with a mJ-level λ = 800 nm seed energy in a water-cooled geometry.

5.3 Gain Calculations of Ti:Sapphire Amplifiers

Typically, gain calculations for a laser amplifier is based on the Frantz-Nodvik equation [5]:

$$E_{out} = E_{sat} \cdot \ln[1 + \exp(N_0\sigma) \cdot [\exp(\frac{E_{in}}{E_{sat}}) - 1]] \tag{5.1}$$

where E_{in} is the energy fluence into the crystal, E_{out} is the energy fluence after the amplification, and E_{sat} is the saturation energy fluence, which is defined as [5]:

$$E_{sat} = \frac{hv}{\sigma} \tag{5.2}$$

where the hv is the photon energy at the emission wavelength, and σ is the emission cross-section coefficient at the emission wavelength. For room temperature Ti:Sapphire crystals, the E_{sat} is on the level of 0.9 J/cm^2 [6]. In Eq.(5.1), N_0 is the total initial inversion in the laser medium. With certain pump powers, the output energy of the 1st and 2nd stage can be calculated with different seed energies.

Figure 5.2 shows the calculated output energy from the 1st stage amplifier as a function of the input energy under the absorbed pump energy of 100 mJ. The gain is calculated based on a 2×8 mm^2 pump beam. In this calculation, the seed beam with a dimension of 2×3.3 mm^2 is designed to travel through almost the entire pumped volume twice in six passes. As can be seen in Figure 5.2, with the seed energy above 2.5 mJ, the output energy of the 1st stage could reach the values >30 mJ.

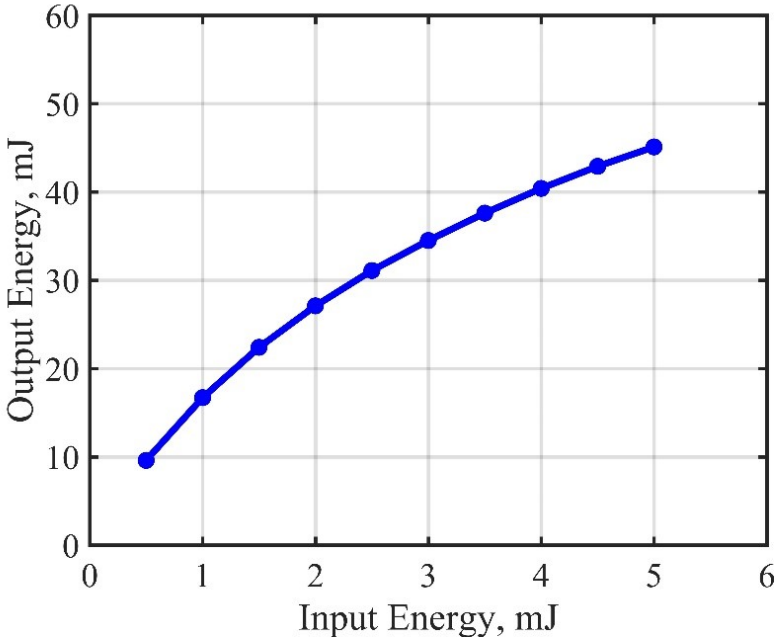

Figure 5.2: Dependence of output energy on input energy for the 1st stage amplifier, with 100 mJ absorbed pump energy.

The same principle was applied to the gain calculation for the 2nd Ti:Sapphire stage. The pump beam size is $2\times18\,\mathrm{mm}^2$, and the seed beam size is $2\times10\,\mathrm{mm}^2$. As shown in Figure 5.3, over 300 mJ output energy could be obtained with more than 20 mJ seed energy with 700 mJ pump.

Based on the gain calculation results, the output fluence of the 1st stage and 2nd stage beam is on the level of $1\,\mathrm{J/cm}^2$ and $1.9\,\mathrm{J/cm}^2$, respectively. Considering the damage threshold of the standard dielectric anti-reflection (AR) coating with around 300 ps pulse duration, the surfaces for the seed beam were designed as Brewster angles for both crystals in reality, which can reduce the possibility of system failure causing by coating damage. Moreover, the B-integral has been calculated for both stages, which is on the level of 1 for both cases.

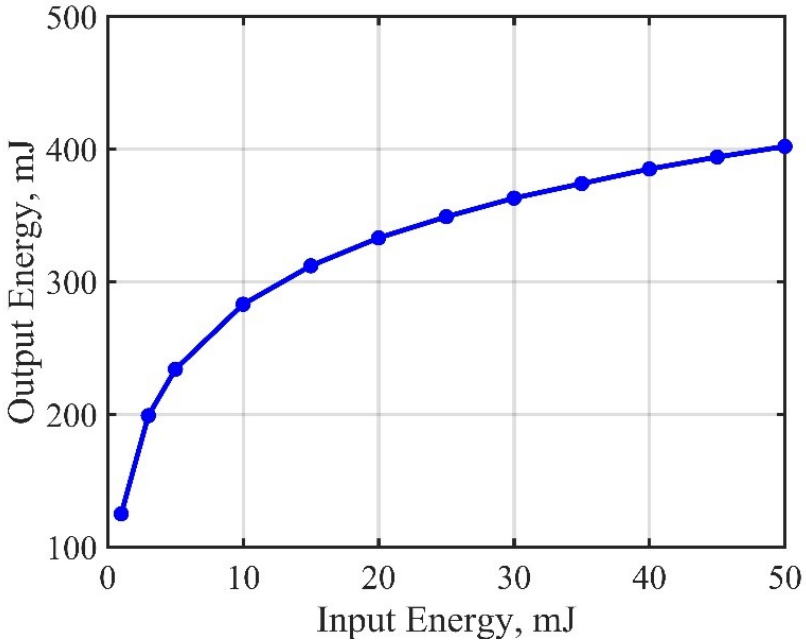

Figure 5.3: Dependence of output energy on input energy for the 2nd stage amplifier, with 700 mJ absorbed pump energy.

5.4 Cooling Design and Thermal Simulation of Ti:Sapphire Amplifiers

Besides the gain calculations, the cooling design and thermal simulation of both Ti:Sapphire amplifier stages are necessary to generate pulses with few hundreds of millijoule energy at up to 1 kHz repetition rate. As mentioned in Section 5.3, the 1st and 2nd stage XTS Ti:Sapphire amplifier requires 100 mJ and 700 mJ pump energy to achieve the 300 mJ level output energy, respectively. The power of the heat source in the crystal can be estimated based on the quantum defect of the laser material [6, 7], which is calculated from the seed and pump wavelengths:

$$QD = (1 - \frac{\lambda_{abs}}{\lambda_e}) \times 100\% \tag{5.3}$$

where the *QD* represents the quantum defect, the λ_{abs} is the absorption wavelength, and the λ_e is the emission wavelength. In the design of both XTS Ti:Sapphire amplifiers, the pump wavelength

is 515 nm and the emission wavelength is 800 nm:

$$QD = (1 - \frac{515\,nm}{800\,nm}) \times 100\% = 36\% \tag{5.4}$$

which means about 36% of absorbed λ=515 nm power will transfer to the heating power in the crystal. As a result, the estimated heat power for the case of 100 W and 700 W absorbed pump power is 36 W and 252 W, respectively.

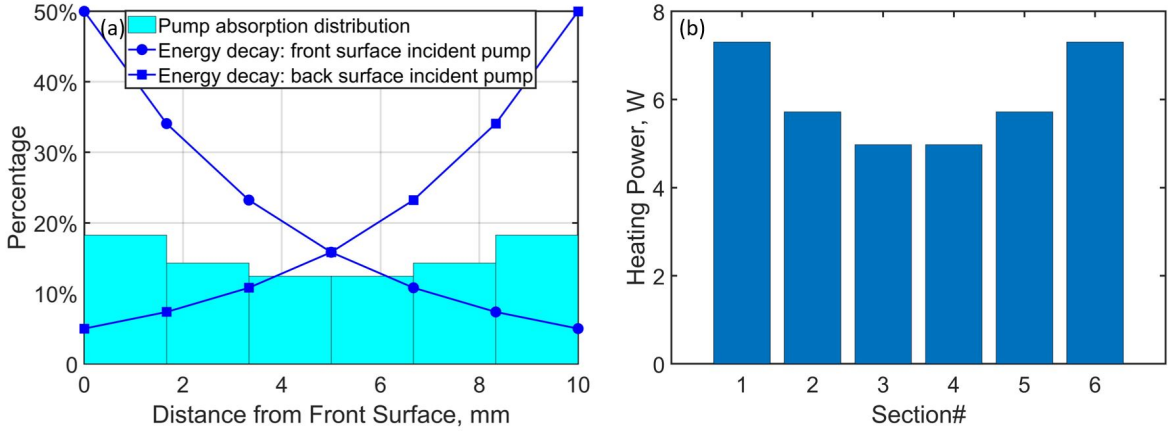

Figure 5.4: The heating power distribution of 1st stage crystal. (a) Pump energy decay and pump absorption distribution vs. crystal location; (b) Heating power at each section of crystal.

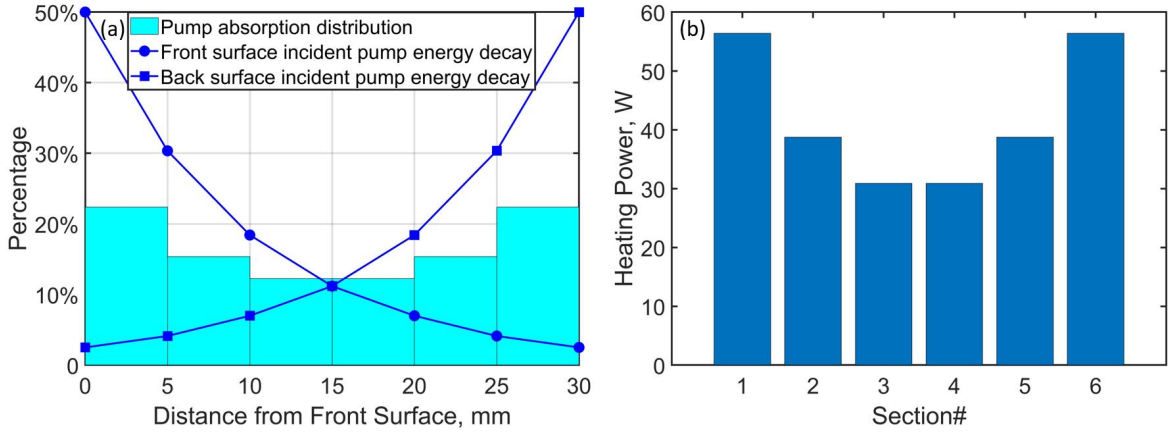

Figure 5.5: The heating power distribution of 2nd stage crystal. (a) Pump energy decay and pump absorption distribution vs. crystal location; (b) Heating power at each section of crystal.

We conducted a finite element method (FEM) simulation with a flowing liquid model for estimating the thermal distribution of the crystal under the pump power used in the gain calculation. To compute the temperature distribution using a realistic absorption profile, the pumped area was divided into six individual zones in the direction of the pump light. The absorption in each zone as a function of length was calculated based on Beer-Lambert law [8, 9] and absorption coefficient of the crystal. In the case of the 1st stage crystal, 36 W of heat was applied to the crystal, which indicates 100 W of absorbed pump power. The heating power distribution, as shown in Figure 5.4, is calculated with the pump absorption at each section of the crystal with an absorption coefficient of 2.3 cm^{-1}. For the crystal in the 2nd stage, as shown in Figure 5.5, a total heat power of 252 W was applied to the crystal. Due to the different dimension of the 1st and 2nd stage crystals, the absorption coefficient of 1.0 cm^{-1} was used in the 2nd stage crystal to achieve 95% single-pass absorption rate. The thermal conductivity of 35 W/(m·K) was used for room temperature Ti:Sapphire [10].

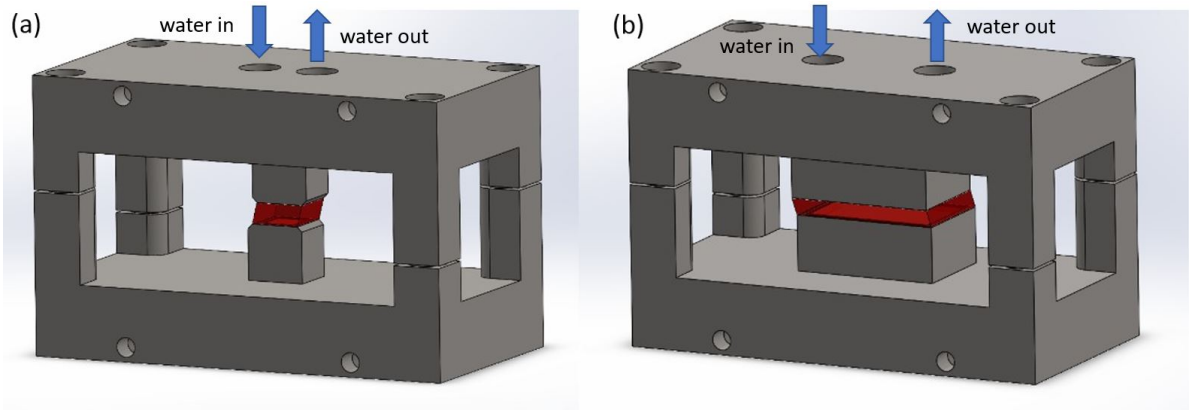

Figure 5.6: Cooling mount design of the (a) 1st and (b) 2nd stage crystal.

Stainless steel cooling mounts were designed for each amplifier crystal to provide the necessary water cooling capacity. As shown in Figure 5.6, two identical parts symmetrically hold the Ti:Sapphire crystal at the center. Each mount has a 1 mm thick water channel between the mount and crystal's largest surface, which allows the highest water flow rate passing through the direct-contact water-crystal interface with certain water pressure. The water channel is sealed with indium wire which can hold more than 100 PSI of water pressure. For the 1st stage crystal, the

flow rate was designed to be 1 GPM at 95 PSI water pressure. For the 2nd stage crystal, the flow rate was design to be about 1.5 GPM at 95 PSI water pressure. The water temperature was set at 20 °C.

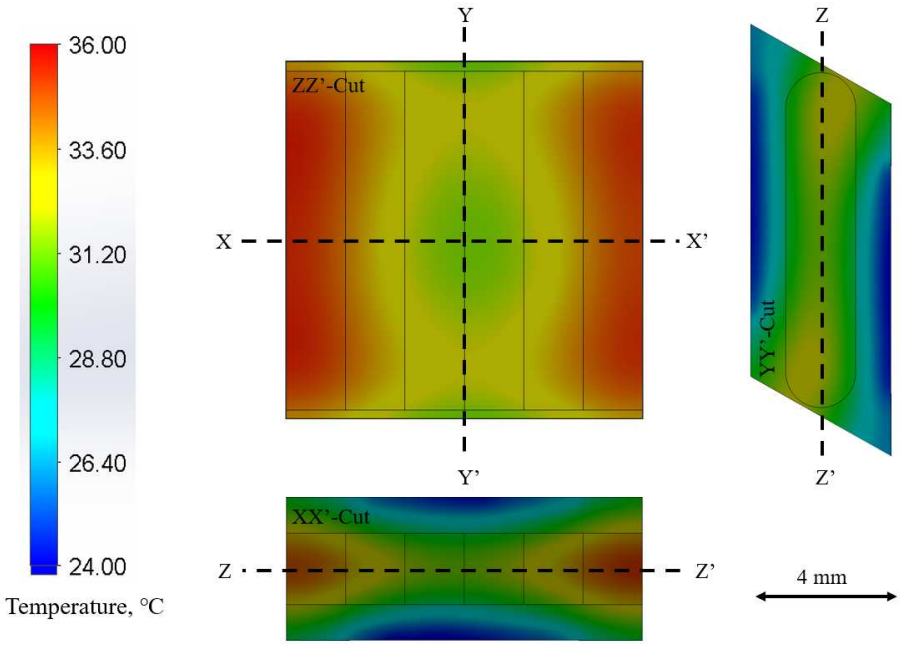

Figure 5.7: Thermal distribution of the 1st stage crystal.

Figure 5.7 and Figure 5.8 show the simulation result of the thermal distribution of the 1st stage crystal and 2nd stage crystal, respectively. As shown in the case of the 1st stage crystal, the maximum temperature of the crystal is 36 °C, which is located at the input and output area of the pump beam where the highest heating power is applied. The surface contacting the flowing water has the coolest temperature of 24 °C. Based on the three-axis-cut plots in Figure 5.7, in the transverse direction of the pump beam (XX'-cut), the temperature difference between the center and the edge of the pump beam is about 3 °C. In the transverse direction of the seed beam (YY'-cut), the average temperature difference between the center and edge of the seed beam is also about 3 °C. Similar temperature distribution can be noticed in the case of the 2nd stage crystal. The maximum temperature of the crystal is about 47 °C. As shown in Figure 5.8, in the transverse direction of the pump beam (XX'-cut), the temperature difference between the center and the edge

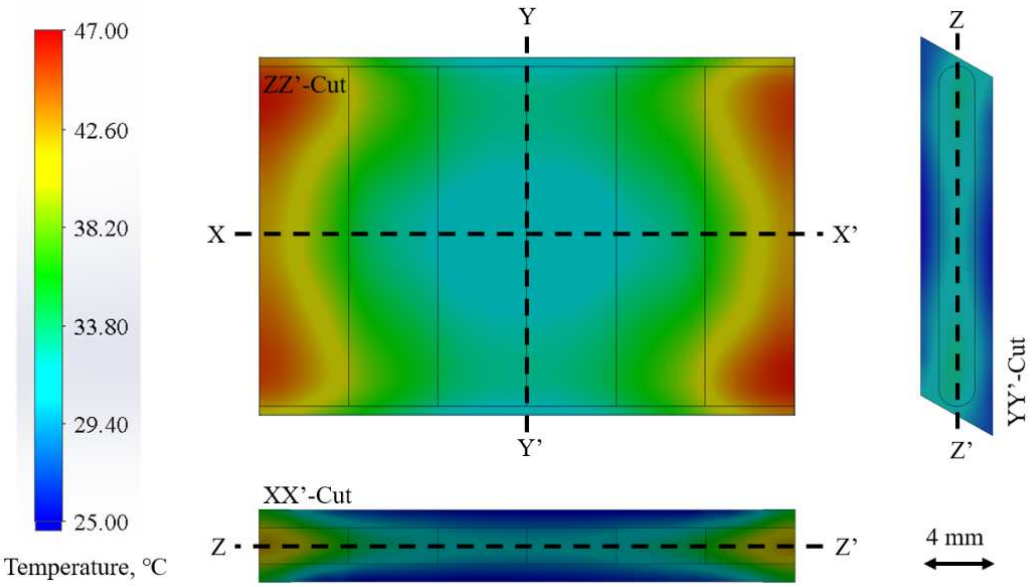

Figure 5.8: Thermal distribution of the 2nd stage crystal.

of the seed beam is about 2.5 °C. In the transverse direction of the seed beam (YY'-cut), the average temperature difference between the center and edge of the seed beam is also about 2.5 °C.

For both cases, the simulation results under the extreme heating conditions indicate that the well-designed water-cooling crystal mounts can provide sufficient cooling capacity for both the 1st and 2nd stage Ti:Sapphire amplifiers. Based on these results, the power of the thermal lens effects in both amplifier crystals can be estimated approximately from the thermally induced optical path difference (OPD) [11]:

$$OPD(r) - OPD(0) = -\frac{r^2}{2f} \tag{5.5}$$

where *f* is the focal length of the thermal lens and *r* is the radial coordinates. Furthermore, the OPD can be calculated from the temperature distributions inside the crystal, which is defined as [12]:

$$dOPD(r,z) = [\frac{\partial n}{\partial T} + (n-1)(1+v)\alpha_T + 2C_r n^3 \alpha_T]\Delta T(r,z)dz \tag{5.6}$$

where *dOPD(r,z)* represents the partial OPD at the location *(r,z)* inside the crystal. With the integration along the seed beam transmission direction *z*, the *OPD(r)* at any radial coordinate *r* from center of the crystal to the cooling surface can be calculated. In Eq.(5.6), v is the Poisson's ra-

tio, α_T is the thermal expansion coefficient, *n* is the refractive index of the crystal and C_r is the photo-elastic coefficient. Because the thermal expansion term (the second term in Eq.(5.6)) and the photo-elastic term (the third term in Eq.(5.6)) are typically much smaller than the thermally induced refractive index change term (the first term in Eq.(5.6)) [12], the *OPD(r)* can be estimated with the thermal-optic coefficient $\partial n/\partial T$ and the temperature distribution along the radial coordinate $\Delta T(r)$.

In the case of XTS crystal geometry, the temperature distribution is mainly in one direction which is between the center of the crystal and the two large cooling surfaces. With the assumption of the small variation in Ti:Sapphire's thermal-optic coefficient in the range of room temperature and the uniform pump beam intensity profile as described above, the temperature distribution from the center of the crystal to the pump surfaces can be negligible. As a result, the thermal lensing can be considered only in one direction, which is between the two cooling surfaces. The crystal acts as a cylindrical lens in the presence of the pump.

With the temperature distributions from the FEM simulation, the thermal lens power of this cylindrical lens can be estimated for a given heating condition. For the 1st and 2nd stage amplifier crystals, the temperature difference between the center and the edge of the seed beam is about 3 °C and 2.5 °C, respectively. Despite the temperature of 1st and 2nd stage crystals being different, the thermal-optic coefficient of Ti:Sapphire doesn't change rapidly near room temperature [13]. As a result, the thermal-optic coefficient of Ti:Sapphire at room temperature can be found as 1.3×10^{-5} (1/K) [13]. In addition, the pump beam size for both amplifier stages in the cooling direction is 2 mm. With Eq.(5.5) and Eq.(5.6), the focal length of thermal lens in the 1st and 2nd stage amplifier was estimated to be 1.28 m and 0.77 m, respectively. The estimated results show that it is necessary to have thermal lensing compensation in both amplifier stages. With a lower cooling water temperature, the temperature gradient could be further mitigated due to Ti:Sapphire's increased thermal conductivity and reduced thermal-optic coefficient as the temperature goes down, which can result in a less powerful thermal lens effect for both amplifier stages.

5.5 Experimental Setup and the First Results of the High Power High Energy Ultrafast Laser System

The schematic of the proposed ultrafast laser system can be seen in Figure 5.9. The high energy high repetition rate ultrafast laser system is based on the CPA technology with a Ti:Sapphire front end laser, two XTS Ti:Sapphire amplifiers pumped by the frequency-doubled cryogenically cooled Yb:YAG laser, and a grating pair compressor.

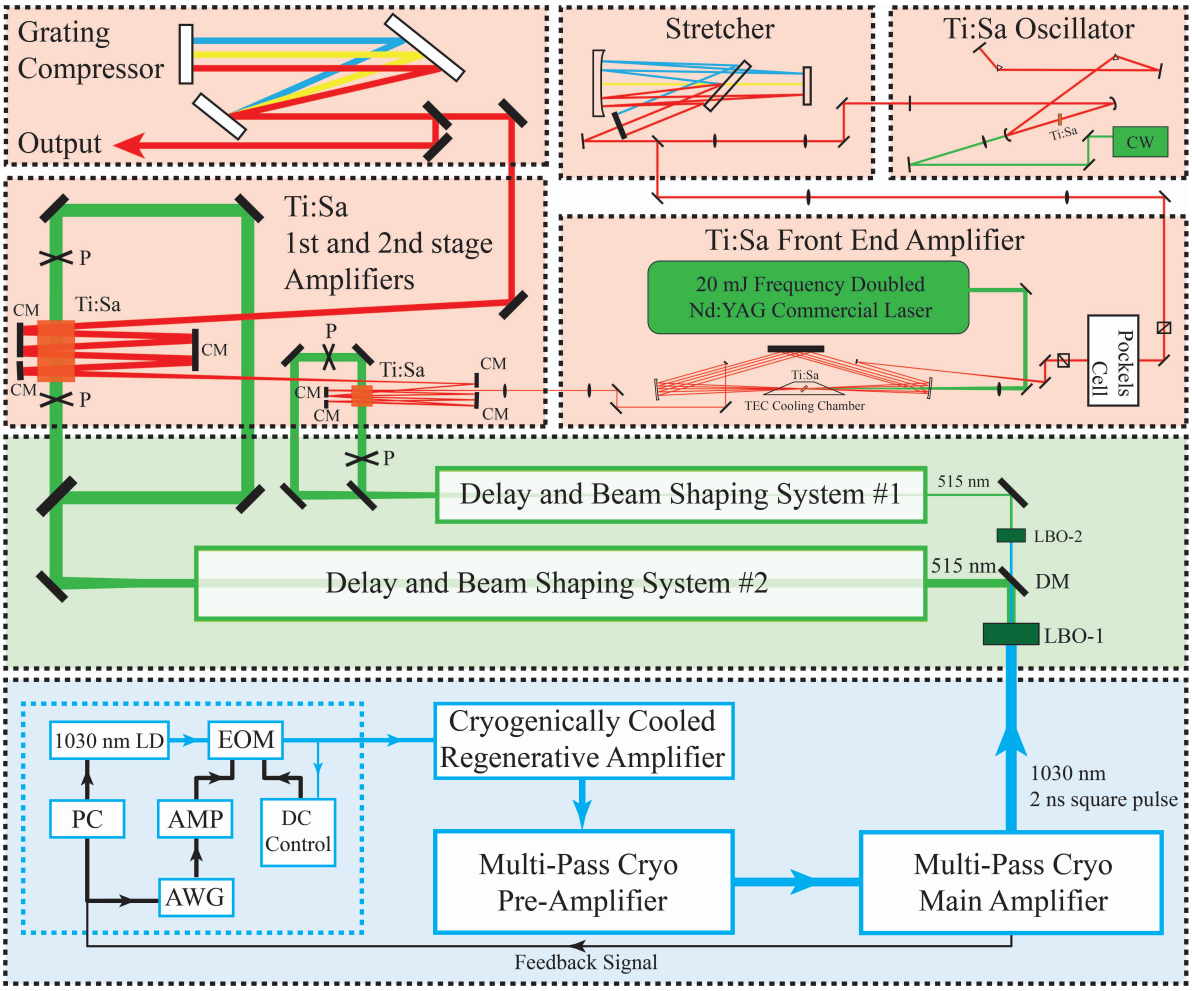

Figure 5.9: Schematic of the high energy high repetition rate ultrafast laser system.

The Ti:Sapphire front end laser consists of a Kerr lens mode-locking Ti:Sapphire oscillator, a Martinez stretcher, and a multi-pass thermoelectric cooler (TEC) cooled Ti:Sapphire amplifier.

An 85 MHz Kerr lens mode-locked Ti:Sapphire oscillator produced about 7 nJ seed pulses with more than 40 nm full width half maximum (FWHM) spectral bandwidth. The output pulses of the oscillator were first stretched to 300 ps FWHM duration by a Martinez stretcher. A Pockels Cell was subsequently applied to select pulses at a repetition rate of up to 1 kHz. The reduced-repetition-rate stretched pulses were then sent to a multi-pass amplifier with about 3 nJ pulse energy. In the multi-pass front end amplifier, a Brewster angle Ti:Sapphire crystal with the dimension of 5 mm diameter $\times$ 6 mm length was pumped by a commercial green laser with a maximum 20 mJ pulse energy at 1 kHz (Northrop Grumman PA-100-QMG). More than 90% of the pump light was absorbed by this Ti:Sapphire crystal. The repetition rate of the pump pulse can be varied by a synchronized phase-locked chopper if a different repetition rate is required. To compensate the thermal effect at a higher than 500 Hz repetition rate, a TEC cooling system was designed for dissipating the heat and reducing the temperature of the Ti:Sapphire crystal to -25 °C. A Brewster-window N_2-filled chamber was used to avoid the water condensation on crystal surfaces. With a 7-pass design, the front end amplifier is capable of generating >3 mJ pulses at a repetition rate up to 1 kHz with a standard pulse-to-pulse energy deviation of less than 0.8%. A 250 μm diameter spatial filter was applied to improve the beam quality for the subsequent amplifier stages and to avoid the feedback from the subsequent amplifiers. Due to the gain narrowing effect, the spectral bandwidth of the amplified pulses was reduced to FWHM of 25 nm without additional spectrum compensation devices, which could support sub-40 fs transform-limited pulses.

The output beam of the front end laser is first boosted in the 1st stage XTS Ti:Sapphire amplifier. The crystal used in the 1st stage is a 1 cm^{-1} absorption coefficient Ti:Sapphire with a dimension of $10\times10\times4$ mm^3. The 8×2 mm^2 elliptical beam size was achieved by imaging the up to 120 mJ pump pulse from the second LBO crystal in the SHG system through a telescope system. A 50:50 beamsplitter was used to separate the pump beam evenly to the two pump surfaces of the XTS Ti:Sapphire crystal. Because of the Brewster angle on the two seed surfaces, the crystal was mounted with an angle of 29.6° to the optical table for using a horizontal parallel seed beam, as shown in Figure 5.10. Two periscopes were used to maintain the orientation of pump beams well-

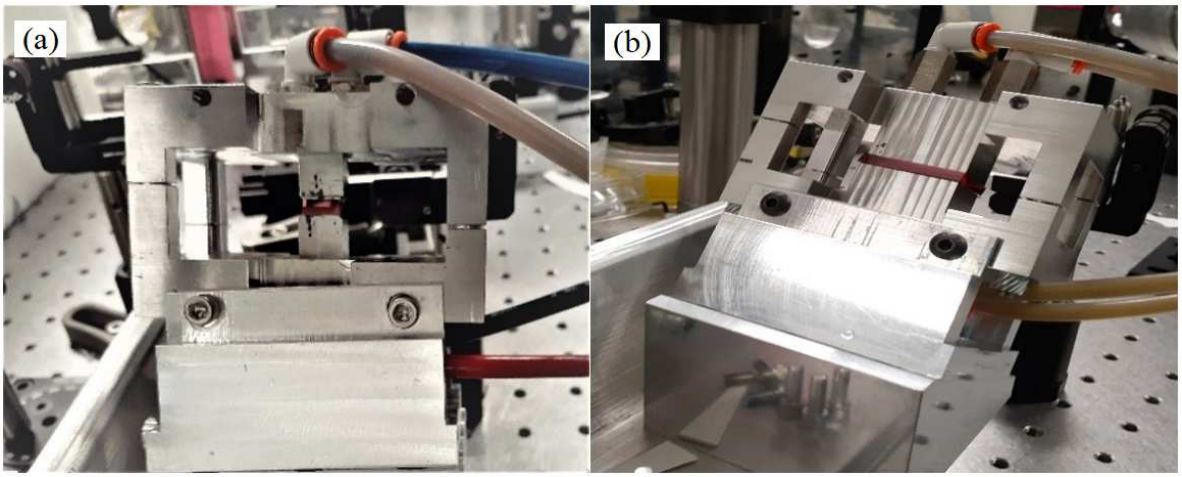

Figure 5.10: The mount assembling with Ti:Sapphire crystal inside of (a) the 1st stage amplifier and (b) the 2nd stage amplifier.

aligned with the crystal's direction. More than 90% of the 515 nm pump energy was absorbed by the crystal, and a reflective mirror was used to send the pump beam back to the crystal for increased absorption of both pump beams. Three cylindrical mirrors were used to form an 8-pass geometry and to ensure the efficient energy extraction of the seed beam through the entire pumped area of the crystal. The vertical size of the seed beam on Ti:Sapphire crystal was maintained by these three cylindrical mirrors, while the horizontal beam size was gradually increased with the divergency of the seed beam. For different repetition rates of the pump, different combinations of cylindrical mirrors with different focal lengths, distance between two cylindrical mirrors, and location of the Ti:Sapphire crystal were used to compensate for different power of thermal lensing. Another cylindrical mirror placed after the last pass through the Ti:Sapphire crystal was used to kick out the amplified beam maintaining a collimated vertical divergency. Pump energies up to 120 mJ were tested at repetition rate from 50 Hz to 1 kHz repetition rate. The maximum temperature of the Ti:Sapphire crystal while operating at 1 kHz repetition rate did not exceed 35 °C when operated with a cooling water temperature of 10 °C, as confirmed by a thermal camera image shown in Figure 5.11. With thermal lensing compensation, the output energy of 25 mJ was demonstrated with good beam intensity uniformity with up to 1 kHz repetition rate.

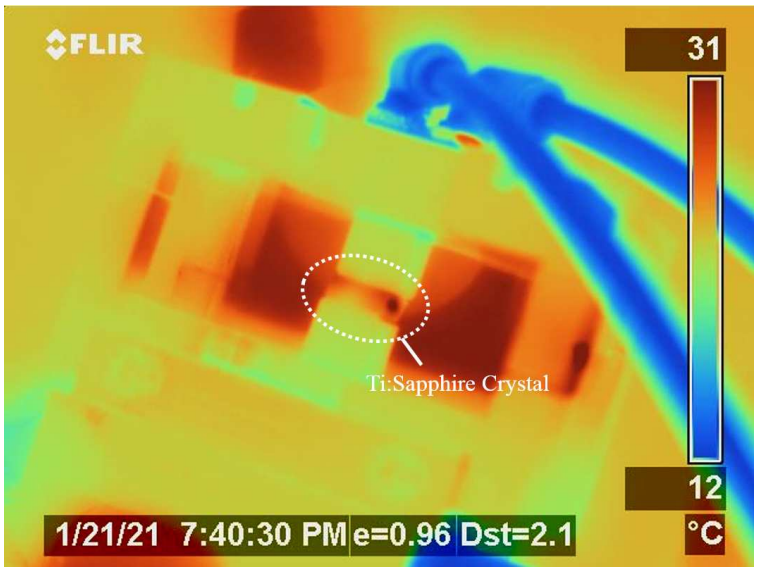

Figure 5.11: Thermal camera picture with the temperature distribution within the 1st Ti:Sapphire amplifier, operating at 1 kHz repetition rate. The Ti:Sapphire crystal is identified by the dotted line circle.

After the amplified beam was kicked out from the 1st stage amplifier, the beam was sent to the 2nd XTS Ti:Sapphire amplifier stage. The Ti:Sapphire crystal has a dimension of $20\times30\times4\,\text{mm}^3$ with an absorption coefficient of $1.0\,\text{cm}^{-1}$, which means more than 95% of the absorption rate could be achieved with a single pass through the 30 mm absorption length. The two $30\times4\,\text{mm}^2$ Brewster angle surfaces were used for the seed beam. An 8-pass geometry formed by three cylindrical mirrors was used to extract the energy. The total transmission loss of the 2nd stage amplifier was less than 20% after the 8 passes. The λ = 515 nm pump beam from the 1st LBO crystal in the SHG system was imaged to the pump surfaces of the 2nd stage XTS Ti:Sapphire crystal through a telescope system with four cylindrical lenses. The cylindrical lenses reshaped the pump beam from a diameter of 14 mm on the output of the LBO crystal to an elliptical size of $2\times18\,\text{mm}^2$ on the $4\times20\,\text{mm}^2$ pump surfaces of the Ti:Sapphire crystal. A delay distance was deployed in the imaging system to synchronize the arrival of the λ = 800 nm seed beam with respect to the pump to maximize gain while reducing the amount of ASE. The shaped pump beam was split into two pump beams with pulses of equal energy (50:50) by a thin film beam splitter. Two pairs of periscopes were subsequently used to rotate the oval shape pump beams to align them with the orientation of the Ti:Sapphire crystal while maintaining the polarization of the pump beam to ensure

maximum absorption. In a preliminary test, more than 700 mJ of pump energy was delivered to the Ti:Sapphire crystal. As the repetition rate changed, different combinations of the focal lengths of cylindrical mirrors, distance between two cylindrical mirrors and location of the Ti:Sapphire crystal were used to compensate for different power of thermal lensing in the 2nd stage amplifier.

A compressor with a pair of gratings in a vacuum chamber was placed after the output of the 2nd stage amplifier. The output beam from the 2nd stage Ti:Sapphire amplifier was first collimated by an FL=4 m cylindrical lens to achieve a $20\times20\,\mathrm{mm}^2$ square shape and sent into the pulse compressor. The grating pair used in the compressor were gold-coated holographic gratings with 1740 line/mm. A roof mirror with dielectric high reflective (HR) coating was used to bounce back the beam after the first two passes through the grating pair. The distance between the two gratings was about 40 cm which was close to the separation distance in the stretcher. The total throughput of the compressor was measured to be 70% using the λ = 800 nm pulses from the front end.

A Frequency-Resolved Optical Gating (FROG) pulse duration and phase analyzer was set up after the output of the compressor to measure the compressed pulse duration. The measured FROG signal was reconstructed to achieve the pulse duration and phase. The shortest pulse duration achieved for the beam produced by the front end of the laser is less than 55 fs, as shown in Figure 5.12. The pulse duration of the amplified pulses was not yet measured. If an additional spectral compensation device is added before the multi-pass amplifier in the front-end laser to mitigate spectral narrowing during amplification, pulses shorter than 30 fs in duration could be achieved with the current system [14], which could result in the 10 TW level peak power pulses at 1 kHz repetition rate.

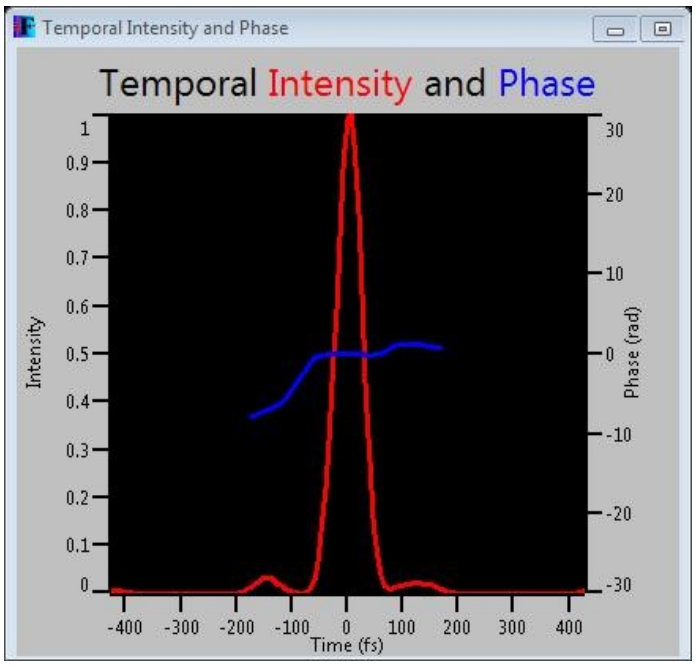

Figure 5.12: The measured pulse temporal intensity and phase results at the output of the compressor. The pulse width is 54.7 fs.

5.6 Conclusion

In summary, we designed and tested a XTS crystal geometry for high energy high repetition rate Ti:Sapphire amplifier, which could provide a larger cooling capacity for heat dissipation compared with the traditional rod/disk crystal in Ti:Sapphire amplifier. A two-amplifier system was designed based on the XTS geometry. The estimated output energy based on the Frantz-Nodvik equation could reach 30 mJ λ = 800 nm pulse energy with 100 mJ λ = 515 nm pump energy from the first amplification stage and 300 mJ λ = 800 nm pulse energy with 700 mJ λ = 515 nm pump energy in the 2nd amplifier. The thermal distributions from the finite element simulations show that an acceptable temperature and temperature gradient could be achieved in both amplifier stage crystals. The first results from the operation of the first amplifier stage showed a good agreement with the gain calculation and thermal simulation results. With spectral narrowing control and adequate compensation for the thermal lensing in the 2nd stage Ti:Sapphire amplifier, 10 TW level peak power operation could be achieved.

References

[1] Colin N Danson, Constantin Haefner, Jake Bromage, Thomas Butcher, Jean-Christophe F Chanteloup, Enam A Chowdhury, Almantas Galvanauskas, Leonida A Gizzi, Joachim Hein, David I Hillier, et al. Petawatt and exawatt class lasers worldwide. *High Power Laser Science and Engineering*, 7, 2019.

[2] M Fibrich, J Šulc, M Jelínek, H Jelínková, and V Kubeček. Influence of temperature on Ti:Sapphire spectroscopic and laser characteristics. *Laser Physics*, 28(8):085801, 2018.

[3] Huabao Cao, Roland S Nagymihaly, and Vladimir Chvykov. Cross thin slab kW-class Ti:Sapphire amplifiers. *Laser Physics*, 29(6):065802, 2019.

[4] Walter Koechner. *Solid-state laser engineering*, volume 1. Springer, 2013.

[5] Lee M Frantz and John S Nodvik. Theory of pulse propagation in a laser amplifier. *Journal of Applied Physics*, 34(8):2346–2349, 1963.

[6] Razvan Dabu. Femtosecond Laser Pulses Amplification in Crystals. *Crystals*, 9(7):347, 2019.

[7] TY Fan. Heat generation in Nd: YAG and Yb: YAG. *IEEE Journal of Quantum Electronics*, 29(6):1457–1459, 1993.

[8] August Beer and P Beer. Determination of the absorption of red light in colored liquids. *Annalen der Physik und Chemie*, 86(5):78–88, 1852.

[9] Jean-Henri Lambert. *Photometria, sive de Mensura et gradibus luminis, colorum et umbrae*. sumptibus viduae E. Klett, 1760.

[10] MG Holland. Thermal conductivity of several optical maser materials. *Journal of Applied Physics*, 33(9):2910–2911, 1962.

[11] C Pfistner, R Weber, HP Weber, S Merazzi, and R Gruber. Thermal beam distortions in end-pumped Nd: YAG, Nd: GSGG, and Nd: YLF rods. *IEEE Journal of Quantum Electronics*, 30(7):1605–1615, 1994.

[12] Sébastien Chénais, François Balembois, Frédéric Druon, Gaëlle Lucas-Leclin, and Patrick Georges. Thermal lensing in diode-pumped ytterbium lasers-Part I: theoretical analysis and wavefront measurements. *IEEE Journal of Quantum electronics*, 40(9):1217–1234, 2004.

[13] Anthony C DeFranzo and BG Pazol. Index of refraction measurement on sapphire at low temperatures and visible wavelengths. *Applied optics*, 32(13):2224–2234, 1993.

[14] Yong Wang, Shoujun Wang, Alex Rockwood, Bradley M Luther, Reed Hollinger, Alden Curtis, Chase Calvi, Carmen S Menoni, and Jorge J Rocca. 0.85 PW laser operation at 3.3 Hz and high-contrast ultrahigh-intensity λ= 400 nm second-harmonic beamline. *Optics Letters*, 42(19):3828–3831, 2017.

Chapter 6

Summary and Outlook

In conclusion, this dissertation demonstrates the development of key components for high power high energy ultrafast laser systems. For the purpose of developing a high repetition rate (500 Hz to 1 kHz level) ultrafast Ti:Sapphire laser with the pulse energy of a few hundred millijoules, with emphasis in the development of the pump laser.

In Chapter 2, a new, *in situ* method to map the 3-D temperature distribution in the gain medium of high average power cryogenic Yb lasers is described. The usefulness of this technique was demonstrated measuring the temperature distribution in a 100 mJ, 100 Hz Yb:YAG active mirror amplifier under different pump powers and cooling interface conditions. 2-D transverse temperature maps are shown to give temperature values that correspond to the average temperature in depth. In Chapter 3, the characterization of thermal behaviors of the cryogenically cooled Yb:YAG active mirror laser amplifier pumped at kilowatt average power is presented. Measured temperature maps provide the thermal distribution in the gain medium at these high pump power levels for the first time. Temperature maps were combined with interferometry based optical path difference measurements and simulations to fully characterized the active mirror amplifiers under kW average power operation. Operation of the cryogenically cooled amplifier system at 1 kHz repetition rate produced >1.2 J, λ=1030 nm pulses.

Chapter 4 discusses the generation of Joule-level λ=515 nm laser pulses of nanosecond duration at 1 kHz repetition rate by frequency doubling in LBO the output of 1.2 J, λ=1030 nm laser pulse from the cryogenically cooled Yb:YAG laser. A doubling efficiency of 78% was demonstrated using a 13 mm long LBO crystal. The measured 1.04 kW average power is to our knowledge the highest average power reported for Joule-level green lasers operating at 1 kHz repetition rate. A higher SHG conversion efficiency of 89% was achieved for 0.65 J fundamental pulses using a shorter LBO crystal.

In Chapter 5, the design of the Ti:Sapphire CPA system pumped by this green laser system is presented. The room temperature Ti:Sapphire CPA system consists of a home-built Ti:Sapphire front end and two multi-pass Ti:Sapphire amplifiers. An XTS crystal geometry for high energy high repetition rate Ti:Sapphire amplifier is proposed for both multi-pass amplifiers. The geometry was designed to provide sufficient cooling capacity for 1 kHz repetition rate. The thermal distributions from the finite element simulations show that acceptable maximum temperature and temperature gradient could be achieved in both amplifier crystals. The Frantz-Nodvik computations indicate that the output pulse energy could reach 30 mJ with 100 mJ pump energy from the first amplification stage and 300 mJ with 700 mJ pump energy from the second amplifier. The first results from the first amplification stage show a good agreement with the gain calculation and thermal simulation results.

The future work will include the further thermal lensing compensation caused by high average power pump and the inclusion of a spectral pre-compensation device to mitigate the gain narrowing in the amplifiers that could generate about 250 mJ energy pulses of 30 fs duration at 0.5-1 kHz repetition rate.

Among application of interest is the long range propagation in the air for remote sensing for which is necessary to study the air propagation an filamentation of high average power, high pulse energy laser in the atmosphere. On this topic, the kHz repetition rate high power Yb:YAG laser described in Chapter 4, was recently used to study the filamentation generation in atmosphere. This resulted the demonstration of permanent channel consisting of density depression that is of the interest for guiding directed high energy laser beams[1].

[1] A. Higginson, Y. Wang, H. Chi, A. Goffin, I. Larkin, H. M. Milchberg, and J. J. Rocca, "Wake dynamics of air filaments generated by high energy picosecond laser pulses at 1 kHz repetition rate", submitted to Optics Letters (2021).